HELSINGIN YLIOPISTO
HELSINGFORS UNIVERSITET
UNIVERSITY OF HELSINKI

Master`s thesis
Petrology and Economic Geology

Composition of chromite in the Sakatti Cu-Ni-PGE deposit, Central Lapland Greenstone Belt, Finland

Saara Silventoinen
12/2020

Supervisors:
Petri Peltonen (University of Helsinki)
Tuomas Väliheikki (Anglo American plc)

UNIVERSITY OF HELSINKI
FACULTY OF SCIENCE
DEPARTMENT OF GEOSCIENCES AND GEOGRAPHY

PL 64 (Gustaf Hällströmin katu 2)
00014 Helsingin yliopisto

HELSINGIN YLIOPISTO
HELSINGFORS UNIVERSITET
UNIVERSITY OF HELSINKI

Tiedekunta/Osasto Fakultet/Sektion – Faculty Faculty of Science		Koulutusohjelma– Degree programme Master's programme in Geology and Geophysics
Tekijä/Författare – Author Saara Helena Silventoinen		
Työn nimi / Arbetets title – Title Composition of chromite in the Sakatti Cu-Ni-PGE deposit, Central Lapland Greenstone Belt, Finland		
Opintosuunta/Studieinriktning – Study track Petrology and Economic Geology		
Työn laji/Arbetets art – Level Master's thesis	Aika/Datum – Month and year 12/2020	Sivumäärä/ Sidoantal – Number of pages 95 pages

Tiivistelmä/Referat – Abstract

Chromite $(Fe^{2+}, Mg)(Cr, Al)_2O_4$ contains in addition to the main elements a variety of minor and trace elements. It often occurs as an accessory mineral in cumulate rich olivine rocks. The melt composition is recorded into crystallised chromite. Due to these characteristics, the composition of chromite can be used as a proxy for the petrogenesis of the magma, providing vital information on how the sulphur saturation occurred, and, in particular, to record the conditions of the cooling cumulates.

The Sakatti Cu-Ni-PGE orthomagmatic deposit is located in northern Finland in the CLGB. The deposit is hosted by an olivine cumulate body (the main body), where both disseminated and massive sulphides occur. In addition to the main body, the smaller satellite bodies, the NE and the SW bodies also host mineralisation. The upper barren olivine peridotite body occurs on top of the main body.

Thin sections were selected from each of the olivine peridotite bodies (the main, the upper, the NE and the SW body). The chromites can be divided into two groups; unzoned chromites from the main body and the NE body, and zoned chromites from the upper body and the SW body. The chromite grains occur either as intercumulus positions relative to olivine grains or enclosed by unaltered olivine and pyroxene cumulus grains. The elemental compositions, including SiO_2, TiO_2, Al_2O_3, Fe_2O_3, FeO, V_2O_3, MnO, MgO, ZnO and NiO, of the chromites were analysed using EPMA. The trace element, Ru, was analysed using the LA-ICP-MS.

The Sakatti chromites are characterised by variable content of Mg# (0.18 -0.56), moderately high Cr# (0.56 -0.92) and Fe^{3+}# (0.11 -0.50). In addition to Mg# and Cr#, the Al_2O_3 and TiO_2 compositions and textural features, the Sakatti chromites resemble more of those chromites which saturate from komatiitic magmas than chromites which are associated with picritic or basaltic melts. A subset from those chromites that are spatially associated with massive sulphides display high ZnO (> 0.5 wt.%), low Ni (as low as 225 ppm) and higher TiO_2 (up to 3.22 wt.%). The source behind the elevated Zn-levels could be the assimilation of sulphide bearing sediments to the magma. The Ti enrichment could be explained by the magma being contaminated by iron-rich gabbro during its evolutional history. Nickel contents of the Sakatti chromites range from 225 ppm to 1731 ppm. The majority of the analysed chromite grains are Ni-depleted due to the separation of a sulphide liquid during the magmatic evolution of the Sakatti geological environment. Portion of the Sakatti chromites are Fe^{3+}-rich, which is interpreted to reflect their crystallisation from a melt that have potentially assimilated a sulphur-rich evaporitic rocks, anhydrite. Fe^{3+}-rich chromites together with high Zn, high Ti and low Ni contents represent primary magmatic features in the Sakatti olivine cumulate hosted chromite. Ru content in the Sakatti chromites are low (<2 pbb) and therefore, the low Ru values are an indication of mineralised geological environment.

Avainsanat – Nyckelord – Keywords
Sakatti, Chromite, CLGB, Mineral exploration, Geochemistry, Geology

Säilytyspaikka – Förvaringställe – Where deposited
HELDA – Digital repository of the University of Helsinki

Muita tietoja – Övriga uppgifter – Additional information

TABLE OF CONTENTS

1. INTRODUCTION

Major greenfield mineral deposit discoveries are rarety in Europe. One of these rare major discoveries is that by Anglo American plc, who found the Sakatti Cu-Ni-PGE deposit at Viiankiaapa mire, in Sodankylä, Central Lapland Greenstone Belt (CLGB) in 2009 (Figure 1). The Sakatti Cu-Ni-PGE deposit is a magmatic sulphide deposit that consists of a large cumulate body (the main body) that hosts the main mineralisation and two satellite bodies (the northeast and southwest bodies). The geology is characterised by cumulate peridotites and massive sulphides, which contact a breccia (which acts as the hanging wall) and volcanic rocks (acting as the footwall) (Brownscombe et al. 2015). The most recent published resources include 3.5 Mt of indicated resources at 3.45 % Cu, 2.47 % Ni and 2.49 g/t PGE, and inferred resources at 1.77 % Cu, 0.83 % Ni and 1.37 g/t PGE (Anglo American plc 2019).

Figure 1. Location of the Sakatti Cu-Ni-PGE deposit in Northern Finland. Modified from Anglo American plc presentation (2013).

The CLGB hosts both intrusions and komatiites (Makkonen et al. 2017). The origin of the Sakatti deposit has been under a debate (Brownscombe et al. 2015, Makkonen et al. 2017). Not many studies have yet been published on the Sakatti deposit. Such studies would yield important information on the Paleoproterozoic history of the CLGB and about the mineral potential in the CLGB. This thesis will focus on generating a better understanding of the geochemistry and petrology of the deposit through the study of composition of chromite in Sakatti.

Chromite ($(Fe^{2+}, Mg)(Cr, Al)_2O_4$) occurs as cumulus mineral in mafic and ultramafic rocks. The mineral is composed of a variety elements, from major to trace elements (Irvine 1965), which are determined by the conditions when chromite crystallised (e.g. fO_2 and sub-solidus Mg and Fe change with olivine) (Barnes 1998). These properties make chromite an ideal tracer for parental magma composition (e.g. Irvine 1965, Arai 1992, Peltonen 1995a) and most importantly an exploration tool for magmatic nickel sulphide deposits (Barnes and Roeder 2001, Dupuis and Beaudoin 2011, Evans 2017).

This study aims to examine the chemical composition of the chromite in the Sakatti Cu-Ni-PGE deposit both in the mineralised main, northeast (NE), southwest (SE) bodies, as well as in the unmineralised upper body. Through the chemical composition of the chromite, the cooling history of the chromite can be determined as well as the differences between the bodies and which will give insight into the origin of the deposit. The chemical composition of the chromite was determined using electron probe microanalyser (EPMA). This study systematically reviewed the major element contents of chromite and their variations between the mineralised and barren bodies, aiming to provide differences between the bodies.

An important part of the study was to determine how nickel content of chromite changes, to give new insights for exploration in the CLGB. Recent studies by Locmelis et al. (2013, 2018) have studied the exploration potential of ruthenium content in chromite. A hypothesis is that when the Ru content is low (<150 ppb) in the chromites, it indicates they occurred in a mineralised system (Brownscombe et al. 2015). Because Ru occurs in chromite in trace amounts, its composition was studied with Laser Ablation Inductively Coupled Plasma Mass Spectrometer (LA-ICP-MS).

2. GENETIC MODEL OF MAGMATIC NI-CU-PGE DEPOSITS

2.1. Magmatic Ni-Cu-PGE deposits

Mafic and ultramafic melts derived from the mantle are the major type of melts that form orthomagmatic Ni-Cu-PGE deposits (Naldrett 1999, Barnes and Lightfoot 2005, Arndt et al. 2008). The nickel content of the magma is primarily controlled by olivine content. When magma reaches a high degree of partial melting, it will reach its maximum nickel content and release nickel from olivine. Copper behaves in a different manner compared to nickel, where it stays in the residual sulphide melt and its concentration in the silicate melt is highest when all sulphide minerals have melted. How much sulphur the silicate melt can incorporate, depends on the FeO content in the melt, pressure and temperature and the oxidation state of the melt (Barnes and Lightfoot 2005, Naldrett 2004).

Once the magma has ascended into the crust, the magma has to become saturated in sulphur to form Ni-Cu-PGE sulphide deposits (Barnes and Lightfoot 2005). A separate sulphide liquid phase will form when all the sulphur can no longer stay dissolved to the magma. The Ni-Cu-PGE magmatic ore deposits are formed either when the immiscible sulphide liquid segregates from the melt, or when it is transported within the melt (Naldrett 1999). If the magma is already saturated in sulphide when entering the crust, sulphide liquid can segregate from the magma if the conditions are suitable. However, the economic Ni-Cu sulphide deposits are formed from magmas that were still sulphur undersaturated when emplaced into the crust. The important part of the ore forming process is the interaction between magmas and the surrounding wall rocks (Naldrett 1999). Sulphide undersaturated magmas interact with sulphide- or sulphate-bearing country rocks (e.g. at Noril'sk Talknakh with evaporates that consists of gypsum or anhydrite, and at Kambalda, Western Australia, with sulfidic sediments) (Naldrett 1999). If mafic and ultramafic magmas become saturated enough in sulphide, immiscible sulphide liquid starts to form. The immiscible sulphide droplets are denser than the mafic silicate magma (Barnes and Lightfoot 2005). Density contrasts between the settling heavier crystals (e.g., olivine) and the left-over silicate melt form ortho-, meso- and adcumulates (Wager et al. 1960, Arndt et al. 2008). Cumulate textures were first described by Wager et al. (1960). The classification terms ortho-, meso- and adcumulate, refer to

cumulus rocks, based on the abundance of intercumulus material. Orthocumulates contain 25-50 % of intercumulus material, mesocumulates 5-25 % and adcumulates only 0-5 % of intercumulus material. There are two type of factors that control the amount of cumulus minerals 1) the rate of cooling and 2) the rate at which the nutrient chemical constituents can be supplied to the surface of growing crystals. The sulphide droplets gather chalcophile metals from the silicate magma. The R factor describes the mass ratio of silicate magma to the mass ratio of sulphide melt (Naldrett 2004). The partition coefficient (D_i) of nickel between sulphide and silicate liquid fluctuates from 100 for komatiitic liquids to 300 for basaltic liquids. A formula to partition coefficient (D_i) is:

$$D_i^{(Sul.m\ /Sil.m)} = (wt\%i)^{Sul.m} / (wt\%i)^{Sil.m} \quad (1)$$

Hence for komatiitic magmas the R factor of 1000 is required to accomplish the maximum Ni enrichment. Comparing this to basaltic systems, the R needs to be 3000 in order to fulfill the maximum enrichment. (Barnes and Lightfoot 2015). In contrast, to form PGE-rich sulphide ore, the R factor has to be very high (>10,000) to accomplish the maximum enrichment (Barnes and Lightfoot 2005).

Accumulation and gathering of the sulphide droplets are required to form a sulphide deposit. Otherwise the sulphides occur only as disseminated grains in the rockmass. Massive and net textured sulphides occur in the base of a lava flow or intrusion, whereas the silicate magma transports the sulphide droplets until the flow rate of the silicate magma has decreased and the silicate magma loses its capability to carry the heavy sulphide droplets. This results in the droplets settling to the base. Accumulated sulphide droplets can settle to the footwall or to the feeder dike channel if the flow rate of the magma has sufficiently decreased. (Barnes and Lightfoot 2005).

Magmatic Ni-Cu-PGE deposits can be classified into seven types according to their parental magma composition (Naldrett 2010):

1. Komatiitic related magmatism
2. Flood basaltic related magmatism
3. Ferropicritic related magmatism
4. Anorthosite complex related

5. High MgO basaltic related magmatism
6. Impact related deposits
7. Ural-Alaskan type complex related

Barnes et al. 2016 has summarised the similarities and differences of komatiitic and mafic intrusion related ores (Table 1). The most significant differences among komatiitic and mafic systems are in the magma viscosity and temperature, the variation in commodities and fractionation of sulphide ore magmas.

Table 1. Komatiite-hosted deposits vs mafic-hosted Ni-Cu-PGE deposits. Modified after Barnes et al. 2016.

Attribute	Komatiite-hosted deposits	Mafic intrusion-hosted deposits
Nature of host silicate magma	Low viscosity, high T, fast cooling rate, wide melting range.	High viscosity, low T, slow cooling rates, narrow melting range (relatively).
Nature of sulphide ore magma	Ni-rich, Cu-poor, extremely low viscosity, narrow melting range	Relatively Ni-poor, Cu-rich, low viscosity, wide melting range
Morphology and geometry of host body and plumbing system	Elongate lava tubes or channels. Predominantly horizontal, lateral flow process, vertical feeder dykes almost never preserved.	Tube- or funnel-shaped conduits, flow-through sill-dyke complexes, blade-shaped dykes. Ore formation within long-lived, vertically extensive recharged magmatic plumbing systems.
Relationship to hosts rocks	Thermal/mechanical erosion of floor rocks.	Thermal/mechanical erosion of floor and roof rocks, abundant xenoliths and intrusion breccias.
Massive ore disposition	Usually planar, conformable at basal contacts, may inject into floor rocks.	Commonly cross-cut early marginal rocks of host intrusion and adjacent wall rocks.
Breccia ores	Rare – where found, due to melting of floor rocks and gravitational floating of detached xenomelts.	Breccia ores common – normal Cu-Ni sulphide intrusion/injection breccias, rarely (as at Noril'sk) external Cu-Pd rich explosively emplaced breccia/skarn ores.
Fractionation of sulphide ore magmas	Minor, manifest as subtle differences between massive ores and matrix/disseminated ores.	Common, can lead to chemical and mineralogical differentiation of entire orebody at scales from metres to hundreds of metres.

2.2. Spinel group minerals

The formula of spinel group minerals can be expressed as $X^{2+}Y_2^{3+}O_4$, where the X site (the tetrahedral site) can include divalent cations, such as Fe^{2+}, Mg, Mn, Zn or Ni. The Y site (the octahedral site) can include trivalent cations Fe^{3+}, Al, Cr, Ti or V. Multiple solid solutions are created by different divalent and trivalent cations (Figure 2). Several variations in elements (divalent and trivalent cations) create multiple solid solutions between spinel group minerals (Deer et al. 1992). The compact cubic structure of the spinel includes unit cells, where one cell consists of 32 oxygen ions and 24 cations. The tetrahedral site holds 8 cations per cell and the octahedral site 16 cations per cell. According to the distribution of cations on sites X and Y, the spinel group minerals can be separated into two different types, normal and inverse spinels. In the normal spinel structure, the tetrahedral site is reserved for 8 divalent cations and the octahedral site is reserved for 16 trivalent cations. In the inverse spinel structure, the divalent cations are required to occupy the octahedral site, whereas the trivalent cations have reserved the tetrahedral site and half of the octahedral site. Therefore, the formula of the inverse spinel is expressed as $Y[XY]O_4$, unlike the normal spinel $X[Y]_2O_4$. The major elements are typically projected on a spinel prism, where divalent (Mg, Fe) and trivalent (Fe, Cr and Al) cations are presented (after Irvine 1965, Barnes et al. 1996).

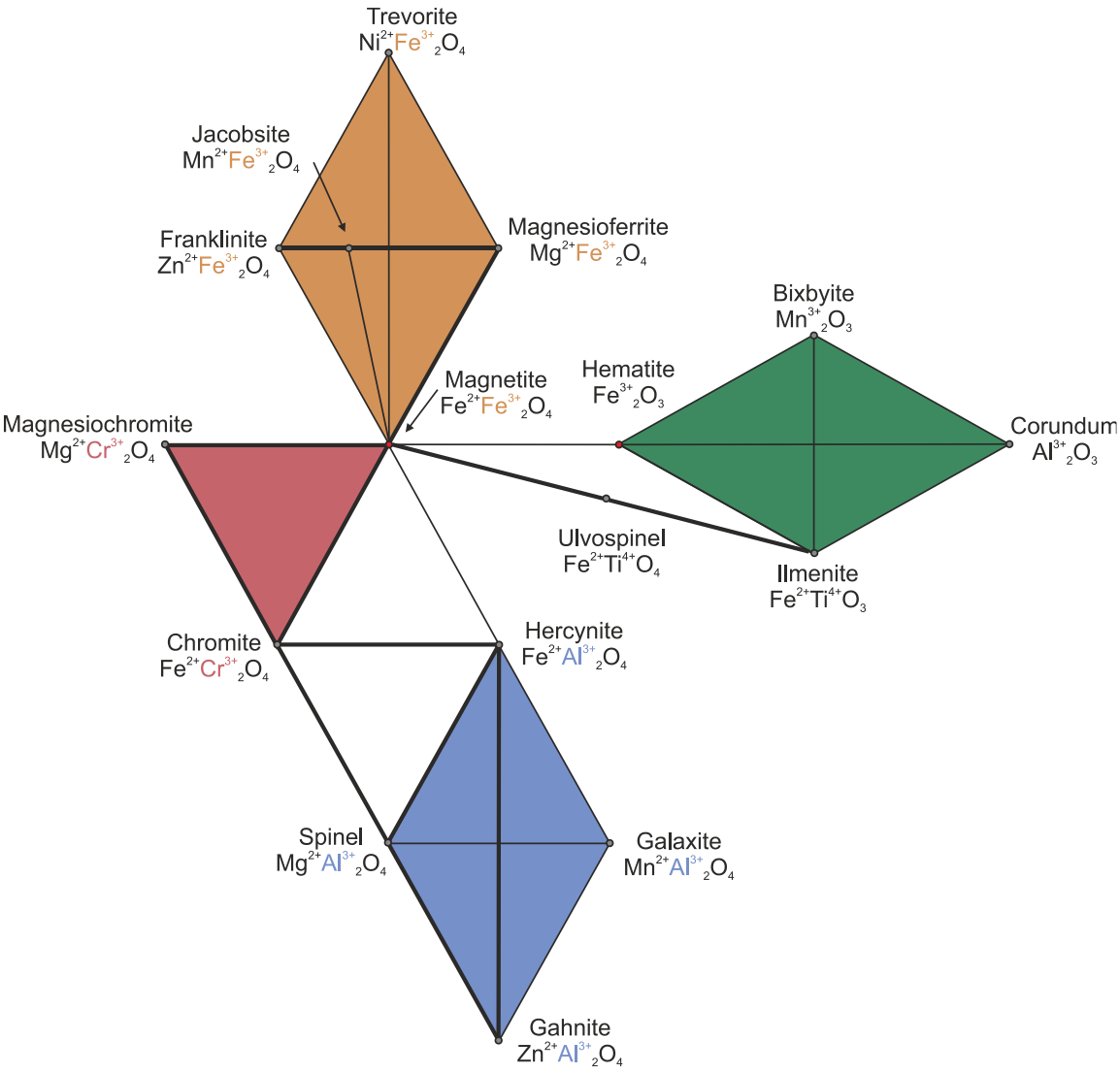

Figure 2. A schematic demonstration of the spinel group minerals. Thicker lines represent the complete solid solution and thin lines partial solid solution. Minerals inside the blue triangles belong to the spinel series, in the pink triangle to chromite and in the orange triangles to the magnetite series. Minerals in the green triangles belong to the ilmenite-hematite solid solution. Modified after Dupuis and Beaudoin (2011).

It is uncommon to find pure spinel solid solution end-members in nature. Spinel group minerals are divided, according to the International Mineralogical Association (IMA) nomenclature, based on the types main trivalent cations: chromite (Cr), magnetite (Fe) and spinel (Al) (Figure 3). Barnes et al. 1996 have estimated fields for spinels (Figure 3). Komatiite-hosted chromites plot within the field of primary igneous chromite (the blue field) and metamorphosed magnetite rims within the field of metamorphic magnetite rims (the pink field). Chromite can also plot within the field of ferrian chromite or if chromites are metamorphosed, they plot within the field of metamorphic chromite cores (the green field). Natural spinels do not occur in the field coloured in grey.

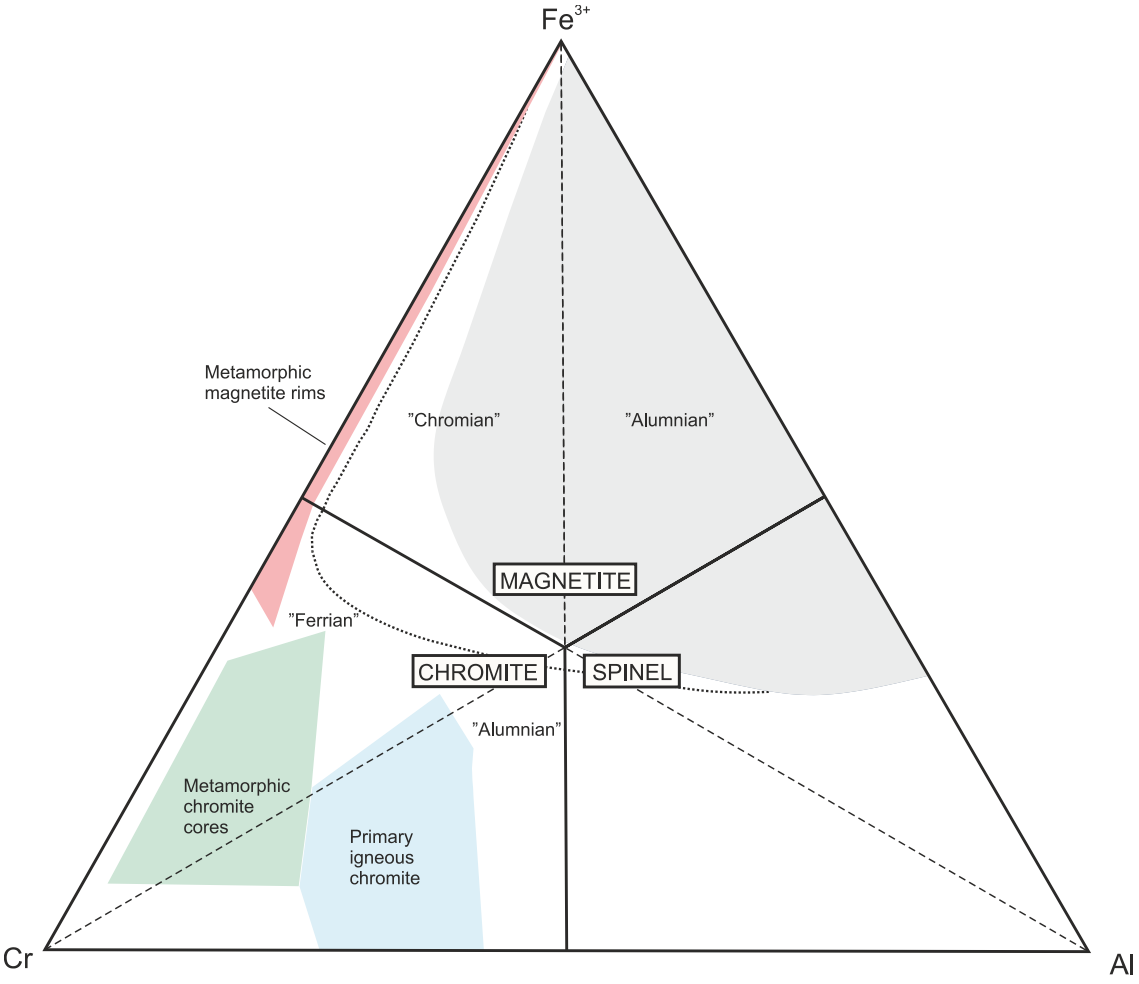

Figure 3. Classification of spinel according to IMA (International Mineralogical Association) nomenclature. The classification is based on the most abundant trivalent cation end member. The end-members are Cr, Fe^{3+} and Al. Primary igneous chromites typically plot within the blue area, metamorphic chromite cores plot within the green area and metamorphic magnetite rims plot within the pink field. Natural spinels do not occur in the grey field. Modified after Barnes et al. (1996).

2.3. Chromite generation in mafic and ultramafic rocks

Chromite is commonly one of the first minerals crystallising from mafic and ultramafic magmas and can be used as proxy for the petrogenesis of the magma (Irvine 1965). Barnes (1998) has demonstrated the crystallisation of chromite when the whole rock compositions MgO % is plotted with Cr ppm (Figure 4). When temperature is decreasing and the oxygen fugacity is dropping, the ability of chromium to dissolve in the silicate liquid decreases (Barnes 1998). Only olivine will crystallise from the melt with the composition 'PK' which represents a typical primitive komatiite (Figure 4). When olivine crystallises, it removes magnesium from the melt, until it hits the Cr saturation point (S).

Both, olivine and chromite will start to crystallise from the saturation point (S) following the cotectic line to form olivine chromite cumulates. The high magnesian komatiitic cumulates do not include chromite as a cumulus phase (Barnes 1998).

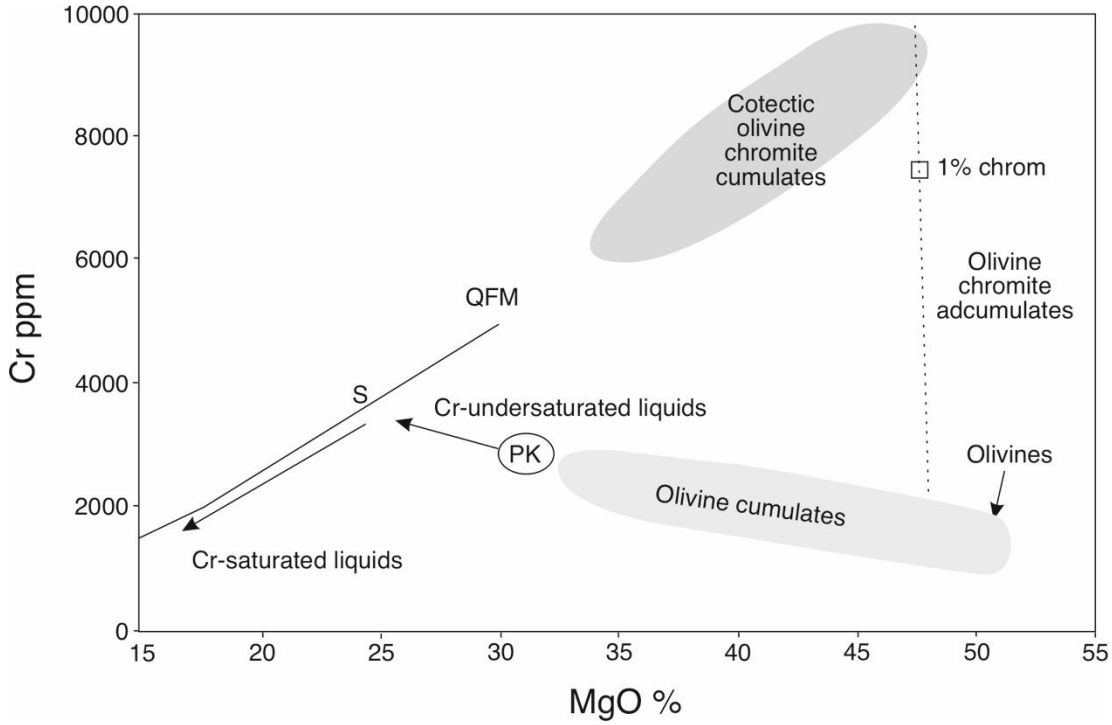

Figure 4.Theoretic presentation of Cr-MgO compositions in komatiitic liquids and cumulates. On the dashed line only 1 % chromite and 99 % olivine has crystallised. On the composition 'PK' only primitive olivine will crystallise. When the composition of liquid reaches to the saturation point S, the liquid begins to cool and crystallise chromite (and olivine). The crystallisation of chromite and olivine follows the cotectic line. Modified from Barnes (1998). Abbreviations QFM = Quartz-fayalite-magnetite buffer.

During subsolidus stage, when chromite and olivine re-equilibrate during cooling, FeO content is forced out of olivine into chromite and MgO from chromite into olivine (Roeder and Cambell 1985). The slower the cooling rate, the more Fe-enriched chromites can become (Barnes et al. 1996). Comparatively, when the cooling rate is high, chromites can retain their relatively high Mg content. In adcumulate rocks, where trapped intercumulus liquid is nearly absent, chromite and olivine do not have the opportunity to change their composition and thus are the most Mg-rich and Fe^{3+}-poor. In contrast, the orthocumulate hosted chromites are more oxidised and iron rich (Barnes et al. 1996). This variability in Fe and Mg content is evident in thin differentiated layered komatiite lava flows. In dunitic parts of the lava flow, chromite retains the unchanged Mg composition, while in orthocumulate parts of the flow, chromite is enriched in Fe^{3+} (Barnes 1998).

The main process that affects the chemical composition of chromite is the igneous evolution of the system. However, alteration and metamorphism also have an important role (Barnes et al. 1996). The interaction with the fluids during metamorphism commences the cation interchange process between the chromite and the silicate phases. The amount of exchange is dependent on the metamorphic grade and the type of the fluid. Serpentinisation of olivine leads to chromite becoming enriched in Fe, and the growth of pure magnetite veins along the open fractures and boundaries of the primary chromite (Barnes et al. 1996). In these magnetite veins, Fe^{2+} replaces Mg^{2+} in the spinel structure resulting in a lighter boundary (seen in the electron microprobe backscatter figures). Magnetite may also start to replace the igneous chromite core. In addition to creating a thin magnetite overgrowth, magnetite occurs as replacement of the primary chromite resulting in a Cr-bearing magnetite rim and chromite core. These chromites are referred as "ferritchromites". The nickel is usually more stable in Fe^{3+}-rich spinels, due to the inverse spinel structure (Barnes 1998). Nickel content of chromite is dependent on the magma's sulphide content. The content also varies between olivine and chromite (Barnes 1998). Both cumulus minerals are depleted from nickel in sulphide mineralised intrusions (Evans 2017).

Chromite is the only source of elemental chromium. Chromite is commonly deposited in thin layers, which only constitute around 1-2 % of the host rock's total volume. Chromitite (= chromite rock) ores consist ~30 % of chromite and is the economic source of Cr (Ripley 2013).

A new potential exploration tool for magmatic Ni-Cu-PGE systems is related to the behavior of platinum-group element ruthenium in chromite (Locmelis et al. 2013, 2018). Chalcophile ruthenium is compatible in chromite ($Kd_{chr/melt}$ ~150) and partitions strongly into the sulphide liquid ($Kd_{sulf/melt} > 10^4$), if the liquid is present. Meaning, in mineralised bodies the Ru content of chromite is low (<150 ppb) and in the barren bodies high (ca 150-600 ppb). Furthermore, Ru-content can be used as an indicator if the system has potential for nickel sulphide mineralisation.

3. GEOLOGICAL SETTING

3.1. Central Lapland greenstone belt

The Paleoproterozoic Central Lapland Greenstone Belt (CLGB) is one of the largest greenstone belts in the world. The CLGB covers an area of over 100x200 km, extending from Russian Karelia in the east, to the Norwegian coast in the northwest (Figure 5) (Hanski and Huhma 2005). The Fennoscandian Shield hosts many greenstone belts, but the CLGB is the largest.

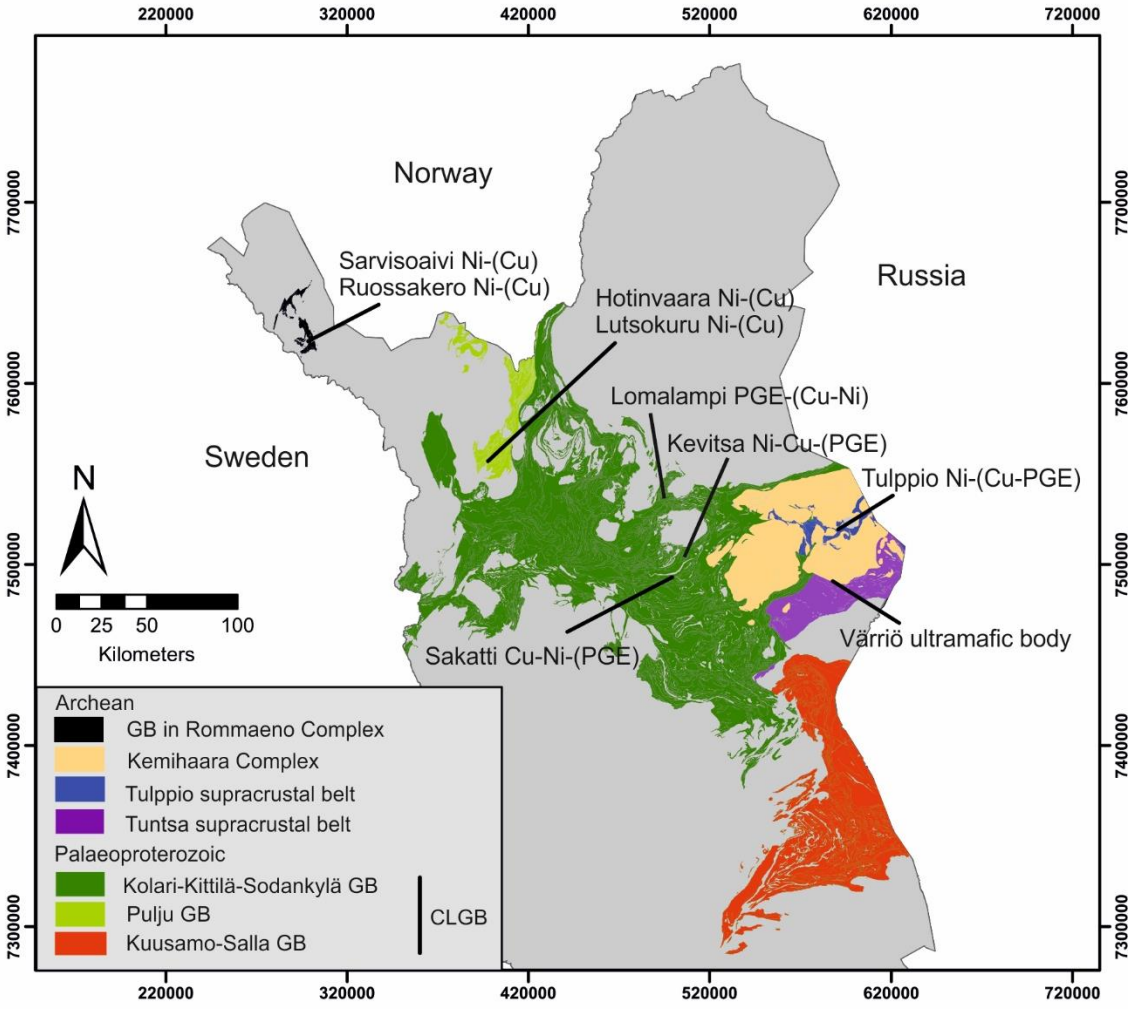

Figure 5. The Central Lapland Greenstone Belt (CLGB) divided into three belts, Kuusamo-Salla GB (red), Kolari-Kittilä-Sodankylä GB (green) and Pulju GB (light green). These belts represent the major komatiite bearing greenstone belts in northern Finland. The Archean complexes, Rommaeno (black) and Kemihaara (yellow) and the Tulppio (blue) and Tuntsa supracrustal belts also host Ni-Cu-PGE deposits in northern Lapland. Modified from Makkonen et al. (2017).

The complex emplacement and deposition history of the CLGB covers circa 600 Ma years from ~2.5 Ga to ~1.88 Ga (Hanski and Huhma 2005, Hölttä et al. 2007). Archean continental rifting events resulted in the emplacement of mostly tholeiitic and komatiitic lavas, dykes and intrusions (Hanski and Huhma 2005). Most of the Ni-Cu deposits elsewhere in the world are hosted by these rock types (Naldrett 2004). The CLGB can be divided into three sub-domains: 1) The Kuusamo-Salla belt, 2) the Kolari-Kittilä-Sodankylä belt and 3) the Pulju belt. There are currently two operating mines in the CLGB: the Kevitsa Ni-Cu-PGE- mine in Sodankylä (Boliden) and Agnico Eagle's Suurikuusikko gold mine in Kittilä (Niiranen 2015). Many exploration projects are ongoing in the region (TUKES 2020).

The CLGB is divided into five different lithostratigraphic Groups and one suite. From the oldest to the youngest are; Salla, Kuusamo (old name Onkamo), Sodankylä, Savukoski, Kittilä suite and Kumpu Group (Figure 6). The Kumpu Group, was previously divided into the Lainio and Kumpu Groups. (Luukas et al. 2017).

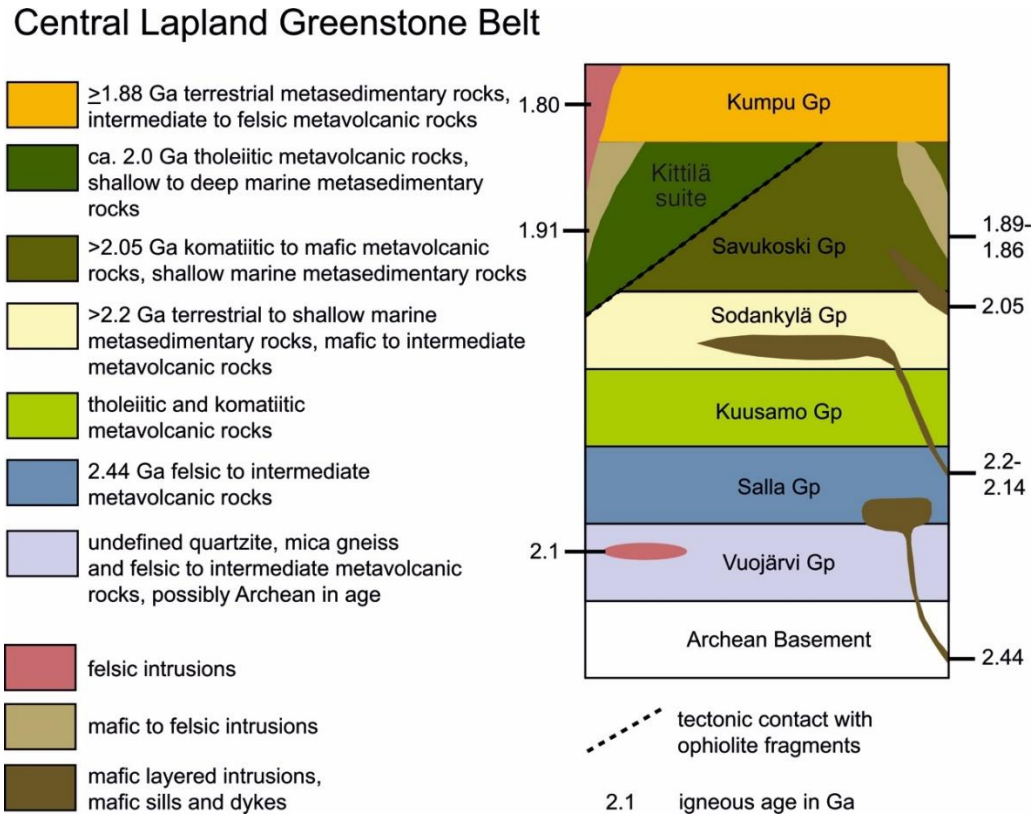

Figure 6. The lithostragraphic units and events comprising the CLGB Groups. Modified after Niiranen et al. (2015). Kittilä suite from Luukas et al. (2017).

The Salla Group metavolcanics (dacitic to rhyolitic tuffs and ignimbrites) formed when the Archean crust started to rift ~2.45 Ga ago. The Salla Group is situated on the boundary between Archean and Proterozoic rocks. Komatiitic to rhyolitic lavas erupted ~2.45 Ga on top of the Archean cratonic crust. These mantle plume-originated lavas also formed large layered intrusions at the same time. Crustally-contaminated hot lavas (up to ~1600 ºC) formed komatiites and picrites at the same time. Mg-rich basalts and mafic rocks formed the Kuusamo group. The Kuusamo Group can be considered to be younger than the Salla Group, as the Koitelainen layered intrusion (2.44 Ga) only intrudes the Salla Group volcanics (Figure 6). However, there is no significant difference in the age between these two Groups. (Hanski and Huhma 2005).

After the active volcanism period, a calm sedimentation phase occurred (Hanski and Huhma 2005). The Sodankylä Group deposited either on top of the Archean gneissic basement or the volcanic rocks of the older Salla or Kuusamo Groups. The Sodankylä Group, also called as the Sodankylä schist area (Räsänen and Huhma 1991) was deposited before ~2.2 Ga (Hanski and Huhma 2005). The Sodankylä Group formed a depositional basin when the volcanism ceased. The basin got wider, and a narrow continental rift was formed where the Sodankylä Group was deposited. The Sodankylä Group consists mainly of metasedimentary rocks, such as arkosic quartzites and mica schists. The minor rock types in the group are carbonate rocks and mafic volcanic rocks. These rocks are metamorphosed and represent tholeiitic basalts, basaltic andesites and amygdaloidal lavas. The Sodankylä Group metavolcanics are more TiO_2-rich than the Salla and Kuusamo Group volcanics (Hanski and Huhma 2005).

The Savukoski Group consists of fine-grained metamorphosed sedimentary rocks, such as phyllites, black schists and minor mafic tuffites. Komatiitic rocks are observed e.g. at the Sattasvaara site in the Sodankylä municipality and at the Jeesiörova site in the Kittilä municipality. There is no significant hiatus in the contact between the two Groups (Sodankylä and Savukoski). (Hanski and Huhma 2005).

The younger Kittilä suite was emplaced in a collisional event at ~1920 Ma ago, when the old oceanic lithosphere (~2000 Ma) was thrusted onto the older cratonic rocks (Hanski

and Huhma 2005, Hölttä et al. 2007). The Kittilä suite consists mainly of mafic metavolcanic rocks and is the most extensive greenstone formation in the whole Fennoscandian shield. The Kittilä suite also includes minor phyllites and black schists. (Hanski and Huhma 2005). Furthermore, it is suggested that close to the eastern margin of the Kittilä suite, there are some interpreted ophiolite fragments, which imply an oceanic origin for some parts of the Kittilä suite (Hölttä et al. 2007).

The Kumpu Group represents the youngest group within the CLGB, with an age of 1.88 Ga. This Group consists of thick immature sedimentary units and some intermediate to felsic volcanic rocks (Hanski and Huhma 2005). After the multiphase rifting event in the CLGB, the Svecofennian orogeny acted on the region between 1.91-1.79 Ga (Hanski and Huhma 2005). The CLGB has an excellent exploration potential for magmatic nickel sulphide deposits (Makkonen et al. 2017).

3.2. Nickel deposits in northern Finland

Northern Finland hosts several nickel deposits (Figure 5) that vary in age from Archean to Paleoproterozoic. The Palaeoproterozoic deposits include the Kevitsa Ni-Cu-PGE intrusion (2058 $\pm$ 4 Ma, Mutanen and Huhma 2001), Pulju belt deposits (Hotinvaara and Lutsokuru, Barnes et al. 1996), Lomalampi PGE-(Ni-Cu) deposit (2058 $\pm$ 93 Ma, Moilanen et al. 2019) and the Savukoski Group komatiites (2056 $\pm$ 25 Ma, Hanski et al. 2001) and the Archean deposits include the Ruossakero deposit (2990 $\pm$ 750 Ma, Moilanen et al. 2019) and the Tulppio dunite (Makkonen et al. 2017, Moilanen et al. 2019). Lithostratigraphic setting and typical host rocks define the different nickel deposit types. All of the Ni-Cu-PGE deposits in northern Finland are listed in Table 2. The majority of the Ni-deposits in the CLGB are related to komatiitic magmatism (Konnunaho 2016), but one of the significant nickel deposits in northern Finland, Kevitsa, is an intrusion (Santaguida et al. 2015).

Table 2. Grades and tonnages of Ni-Cu-PGE deposits of northern Finland. Locations of each deposit is shown in the Figure 5. (AUK= aluminum undepleted komatiite)

Deposit name	Deposit type	Magma type	Resources + (Production) Mt	Ni (%)	Cu (%)	Pd (ppm)	Pt (ppm)	Au (ppm)	Reference for resources
Sakatti	-	-	44.4	0.96	1.9	0.49	0.64	0.33	Anglo American plc (2016 and 2019)
Kevitsa	Intrusion	Picritic basalt	275	0.3	0.41	0.15	0.21	0.11	Santaguida et al. (2015)
Hotinvaara	Komatiite	Ti-depleted	0.30	0.66					Inkinen et al. (1984)
Lutsokuru	Komatiite	Ti-depleted							Barnes et al. (1996)
Ruossakero	Komatiite	Ti-depleted	4.20	0.52	0.01				Lahtinen (1996)
Sarvisoaivi	Komatiite	Ti-depleted							Konnunaho et al. (2015)
Lomalampi	Komatiite	AUK	3.06	0.17	0.06	0.12	0.27	0.07	Koistinen and Heikura (2010)

Kevitsa is a magmatic Ni-Cu-PGE deposit like Sakatti. However, ore grades at Kevitsa are significantly lower than those seen in Sakatti (Table 2). Kevitsa has moderately high Cu/Ni ratios compared globally to other Ni-Cu-PGE deposits (Santaguida et al. 2015). Similar Cu/Ni ratios are also observed in the Sakatti deposit (Brownscombe et al. 2015). The Kevitsa ultramafic intrusion was discovered in 1987, when the Geological Survey of Finland was conducting exploration in the area (Santaguida et al. 2015). The distance between the Kevitsa intrusion and the Sakatti deposit is less than 20 km (Figure 7). However, no direct relationship between these two deposits has been observed. The funnel-shaped Kevitsa intrusion consists of the lower ultramafic unit, overlain by gabbroic rocks (Santaguida et al. 2015). The central dunite body occurs in the middle of the intrusion. The ultramafic lower unit hosts the (main) economic mineralisation in its middle parts and is affiliated with olivine pyroxenites and websterites. Country rocks that surround the intrusion are phyllites and black shales, chloritic volcanic rocks, felsic and mafic metavolcanics and micaceous arkose rocks (Santaguida et al. 2015). The intrusion spreads out to ca. 16 km^2 surface area (Luolavirta et al. 2018). Cumulus chromite occurs in the central dunite unit with olivine and pyroxene (Luolavirta et al.2018). The TiO_2 content varies between 0.4 -2.5 wt.%, Cr_2O_3 between 30.1 to 40.9 wt.% and Al_2O_3 7.6 to

14.1 wt.%. In most of the inspected dunites the chromites occur as inclusions inside olivine. The composition of chromite suggests that the parental magma composition of the central dunite is rather picritic basalt than komatiite (Luolavirta et al. 2018).

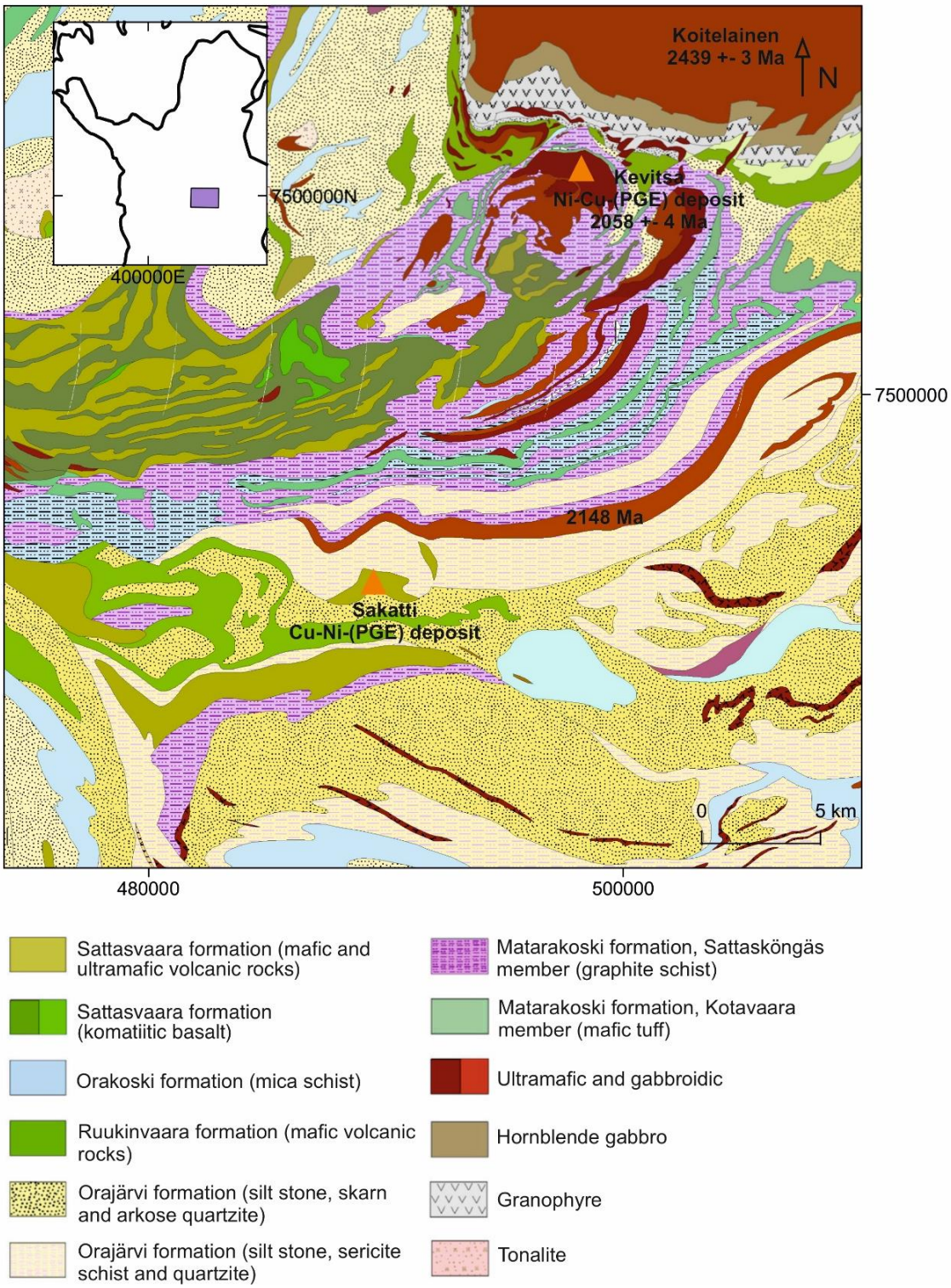

Figure 7. Geological map of the lithological units in the Sodankylä area modified after Digi KP – Bedrock map of Finland. The Sakatti deposit and the Kevitsa intrusion are marked with orange triangles.

The Rommaeno Complex in the Enontekiö-Käsivarsi area hosts Archean komatiitic Ni-deposits (Figure 5). The complex holds several cumulate bodies, but the Ruossakero and Sarvisoaivi are the largest cumulate bodies in the area. Both of the Ti-depleted komatiite bodies host disseminated Ni-(Cu) mineralisation. (Konnunaho et al. 2015).

The Pulju belt connects on the Norwegian side and continues as the Karasjok greenstone belt (Barnes and Often 1990). The Pulju belt includes two ultramafic units in different stratigraphic positions. The upper unit consists of non-fractionated non-cumulate komatiites which bear similarities with the Sattasvaara type of komatiites of Central Lapland (Barnes et al. 1996) and the Karasjok komatiites seen in Norway (Barnes and Often 1990). No chromite has been encountered in the upper unit. The lower unit is also a komatiite and consists of mainly of alteration minerals such as serpentine, tremolite and chlorite. The primary cumulate texture is still preserved. Roundish chromite grains occur in the rocks which were primarily olivine ad- and mesocumulates. A thin magnetite rim surrounds these grains. Barnes et al. (1996) studied chromite grains from Hotinvaara (Figure 5) and Lutsokuru areas. Spinels of the Pulju belt have rare intergrowths with chlorite. However, they are moderately homogenous and unzoned. The Pulju belt chromites have widely ranging Al/Cr ratio and low Fe^{3+} content. Increasing Al content correlates to increasing Mg#. This trend is comparable to that which is seen in layered intrusions. Chromites are low in nickel, which might be due to their extremely low Fe^{3+} content. The mineral chemistry of the Pulju chromites is regulated by equilibration with silicates, primarly chlorite (Barnes et al. 1996).

The Lomalampi area at the Kittilä-Sodankylä belt (Figure 5) hosts four massive komatiitic cumulate bodies. One of the bodies is host to a PGE-(Ni-Cu) mineralisation. Komatiitic ultramafic magmatism is aluminium undepleted and is most likely derived from a low-Mg komatiitic source, which was enriched in PGE. Contamination of PGE-rich komatiitic magma with the sulphur rich country rocks formed the mineralisation of Lomalampi. (Törmänen et al. 2016).

The Archean complexes in the NE of Finnish Lapland include the Kemihaara complex, and Tuntsa and Tulppio supracrustal belts (Figure 5). The Kemihaara complex hosts the Tulppio supracrustal belt, where the largest ultramafic body, the Tulppio dunite, is

located. The komatiitic Tulppio dunite body hosts mineral potential with the best intercept returning 3 m @ 1.12 ppm Pd+Pt, with 0.49 % Ni in the drill core R0320 (Heikura et al. 2010). The Tuntsa supracrustal belt hosts several komatiitic ultramafic bodies including the Värriö ultramafic body. These bodies can be interpreted as a feeder channel or a lava channel system for the komatiitic magma source (Vuollo 1986).

3.3. Geology of the Sakatti Cu-Ni-PGE deposit

The Sakatti Cu-Ni-PGE deposit is located 16 km NNE from the town of Sodankylä and 20 km southwest from the Kevitsa intrusion. The deposit is located under the Viiakiaapa mire, where no outcrops or any indications of the deposit can be seen on the surface (Halkoaho 2014). The deposit is surrounded by Matarakoski formation pelitic metasediments and the Sodankylä Group quartzites. The stratigraphical level of the Sakatti deposit has not yet been resolved and it does not convincingly resemble any specific part of the CLGB sequence (Brownscombe et al. 2015). The age of the Sakatti deposit has not yet been determined, however the nearby Kevitsa intrusion's age is 2058 +/- 4 Ma (Mutanen and Huhma 2001).

3.3.1. Lithologies

Sakatti is a Cu-Ni-PGE deposit, which is hosted by an olivine ortho-meso-adcumulate body (the main body), where both disseminated and massive sulphides occur. In addition, the mineralisation is also enriched in PGE's (Table 2). The body is surrounded by volcanic rocks, which form the footwall and part of the hanging wall. The major part of the hanging wall consists of polymict breccia. Mineralisation is hosted also by smaller peridotite satellite bodies, the northeast body (NE) and the southwest body (SW) (Figure 8). The unmineralised peridotite body, upper body, is situated on top of the main body and is surrounded by the hangingwall polymict breccia. The deposit comprises of the main host and wall rock units, the peridotitic unit, aphanitic unit, mafic suite, breccia unit and volcanoclastic unit. Olivine cumulates (peridotites) are the main host of the mineralisation with some minor parts also occurring in the aphanite unit. The sulphide mineralisation is generally copper-dominated, where a change to more nickel rich mineralisation occur towards the deeper parts of the main body. (Brownscombe et al. 2015).

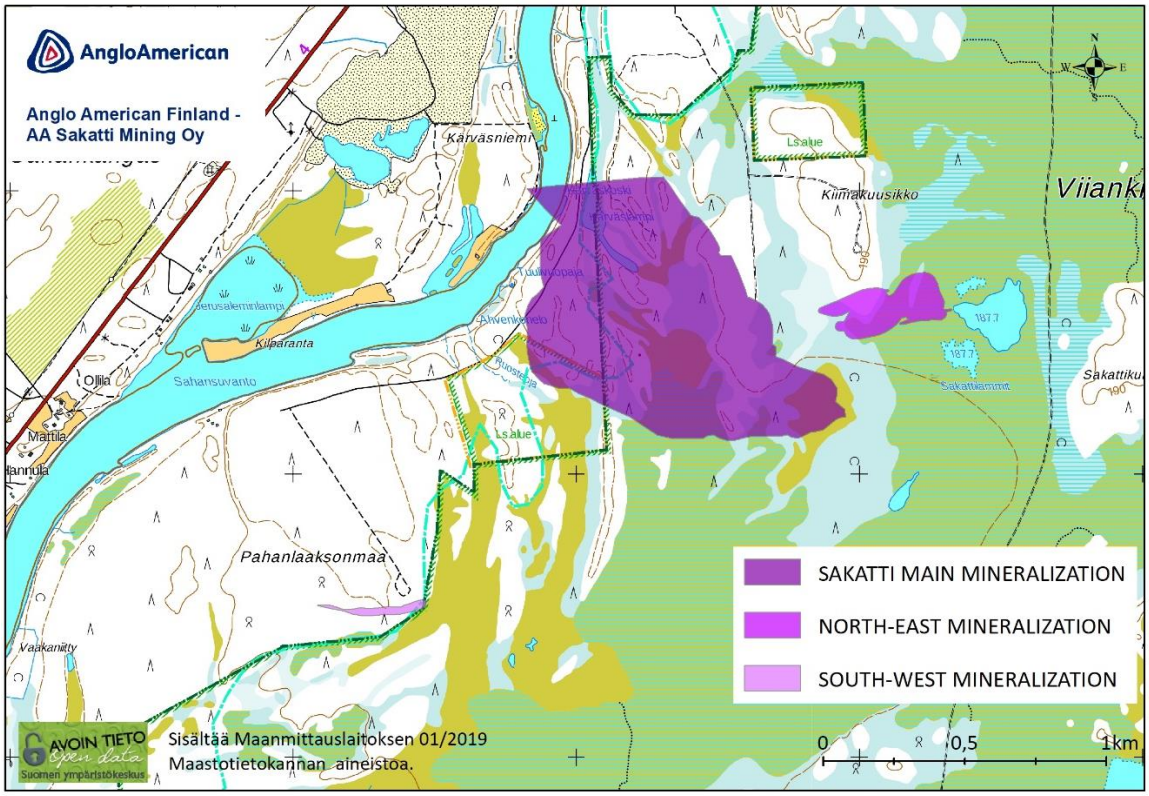

Figure 8. The location of the Sakatti Ni-Cu-PGE deposit in Central Lapland. Note the location of each peridotite body; the south-west body (SW), the north-east body (NE), the upper body and the main body. Courtesy of Anglo American Plc.

The largest peridotite (olivine cumulate) body, the main body, hosts the main massive sulphide mineralisation and the Cu-rich stockwork-style sulphide vein mineralisation. The body dips towards the northwest with a confirmed down-plunge extent of more than 1100 m and a maximum thickness upwards of 400 m. Cumulate textures are well preserved, even if the majority of the unit is extensively serpentinised. The dunite (olivine adcumulate) sub-unit is located in the bottom of the main body with non-serpentinised olivine cumulates. The talc-carbonate altered unmineralised upper body overlies the main peridotite unit and the breccia unit. The aphanitic and breccia units, mafic suite and the hanging wall volcanoclastics overlie on top of the main peridotite body. The aphanitic unit is located mainly on the south side of the main cumulate body and forms the footwall, sidewall and, locally, the hanging wall for the main body. The breccia unit (100-300 m thick) is present stratigraphically on top of the main body. The mafic suite includes three different units (the mafic volcanic rock, the scapolite-mica rock and the hanging-wall gabbro). The mafic suite is situated between the peridotite unit or aphanitic unit and lies below the breccia unit. The volcanoclastic unit is the topmost rock type in the Sakatti main deposits' hanging wall. It is composed of metamorphosed volcanic sediments.

Aphanite is the dominant rock type in the immediate footwall of the Sakatti main deposit. In the eastern part of the Sakatti main deposits a basal thrust structure occurs below the aphanite and separates the deposit's proximal geology from the rock types below. In the western part of the deposit, the structure is more often present directly underneath the main peridotite body. (Brownscombe et al. 2015).

The northeast body is smaller (Figure 8) and has a west-east strike with sub-vertical dip and elongated tail towards the depth. Talc-carbonate alteration of the ultramafic cumulates is more prominent here than in the main body peridotites. In the south and at depth the body is in contact with the breccia unit, and on the northern flank the ultramafics are bordered directly by the volcanoclastic unit. The ovoid shaped SW body occurs towards the southwest from the main deposit cumulate. It is surrounded by the polymict breccia unit in the south and at depth and by the scapolite-mica rock on the northern side. A comprehensive description of the different units is provided by Brownscombe et al. (2015).

3.3.2. Mineralisation

The main, the NE and the SW ultramafic cumulate bodies contain mineralisation in various different forms. The main body hosts several massive sulphide lenses that can reach a thickness of up to 25 m. Stockwork vein type sulphides occur in a minor scale throughout the Sakatti main cumulate unit but are most prominent in the shallow southeastern section of the host rock body. Disseminated style sulphide mineralisation is widespread in the main peridotite body but in the thick central and eastern parts of the cumulate package only the lower half hosts' significant interstitial mineralisation. Noticeable fractionation is manifested in the Ni-Cu ratios of the massive sulphide mineralisations of the main body. In the deeper western and northwestern parts, the massive sulphides are characterised with Ni-Cu ratios larger than one. When moving up-plunge in the main deposit the composition of the massive sulphides becomes increasingly chalcopyrite dominated. In the shallow southeastern part of the main cumulate unit the massive mineralisations have relatively low Ni-Cu ratio. The stockwork vein type sulphides in the southwest are predominantly composed of chalcopyrite which is generally also the main sulphide in the disseminated style interstitial mineralisation

throughout the main deposit. In the NE body, massive sulphides occur on the northern side of the ultramafic cumulates in the contact between the peridotite body and the volcanoclastic unit. Disseminated mineralisation also occurs in the NE cumulates but it is less significant when compared to the main deposit. Ni contents in the massive sulphides are more or less equal to or higher than the Cu contents and thus the metal tenors are similar as in the deeper parts of the main deposit. The SW cumulate rocks host mineralisation mainly in the form of semi-massive to massive sulphides. The metal tenors lean towards nickel with a value of Ni-Cu ratio being 2. (Brownscombe et al. 2015, Ahvenjärvi 2015, Fröhlich 2017).

The sulphur isotope data from the Sakatti sulphides implies that sulphur saturation in the deposit has not likely been caused by local in-situ assimilation of the sulphide-bearing sedimentary rocks of the Matarakoski formation occurring in the surrounding area (Brownscombe et al. 2015). Sulphide-rich sediments have not been detected by drilling in the immediate vicinity of the Sakatti deposit. Anhydrite is present in the Sakatti cumulate rocks. Brownscombe et al. (2015) state that based on the sulphur isotopic evidence, anhydrite can be interpreted to be an oxidation product of magmatic sulphides instead of being derived from an external source.

3.3.3. Petrogenesis

Whole-rock geochemical data from Sakatti displays MgO content (wt. %) typically varying between 19 and 22 wt. % but can range up to 30 %. It is suggested that the aphanitic unit and the main peridotite cumulate body may have formed in the same magmatic event and have the same magma source (Brownscombe et al. 2015). However, the main body may have formed slightly later as a subvolcanic intrusion, according to the theory that Sakatti is a conduit-like intrusion (Brownscombe et al. 2015). The formation model of the Sakatti deposit is under debate. According to Brownscombe et al. (2015), Sakatti is a somewhat younger intrusion into a lava flow field rather than a lava channel cumulate. Makkonen et al. 2017, suggest that Sakatti could be a komatiite-related deposit owing to the high MgO-content and contamination of crustal material. The magmatic affinity of the deposit is still under discussion.

4. MATERIALS AND METHODS

4.1. Samples

The sampling was carried out at the AA Sakatti Mining Oy office (AASMOY), in Sodankylä. Samples were taken from diamond drill cores, which had been drilled during the years 2011-2013 and 2017-2018. The sample selection was based on the whole rock geochemical data from the Sakatti deposit and on the Energy-dispersive X-ray spectroscopy (EDS) analysis that was carried out with the portable XRF-device (pXRF). If the whole rock composition has a content of at least 4,000 ppm of Cr, chromite should exist in the rock (Hanski and Kamenetsky 2013). Chromium content was measured with the pXRF device or was observed from the available whole-rock data. Some of the pXRF-analyses yielded chrome content of up to 1.21 wt.%. In order to study the variation in the composition of chromite, the samples were taken from different depths in the deposit above, between and below the massive sulphide layers.

In total 59 samples were selected for this study. In total 45 thin sections were made from the drill cores and additional 13 selected from a previous study (Halkoaho 2015). From the main body, 43 samples were taken from 8 different diamond drill cores. From the SW, NE and upper body five to six samples were taken from each as per one sampled drillhole for each body. The locations of the samples are presented in Figures 9,10 and 11.

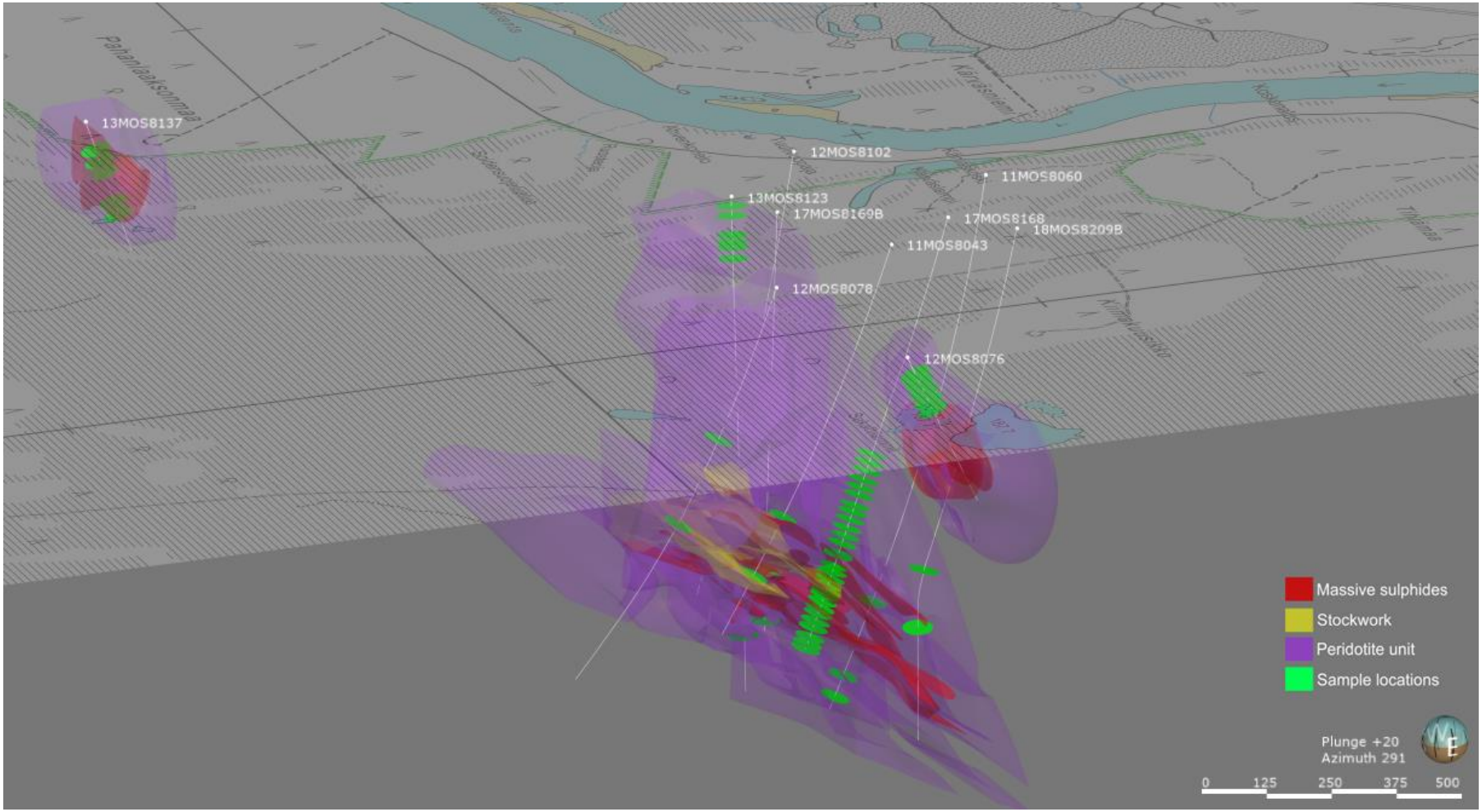

Figure 9. The Sakatti main body (center), the upper body (on top of the main body), the NE body (on the right) and the SW body (on the far left). The purple clouds represent peridotite units, the red volumes represent massive sulphides and the yellow volume represents the stockwork zone. Green disks mark the locations of the samples used in this study. The sample list can be found from Appendix 1. Image is looking from East to the West.

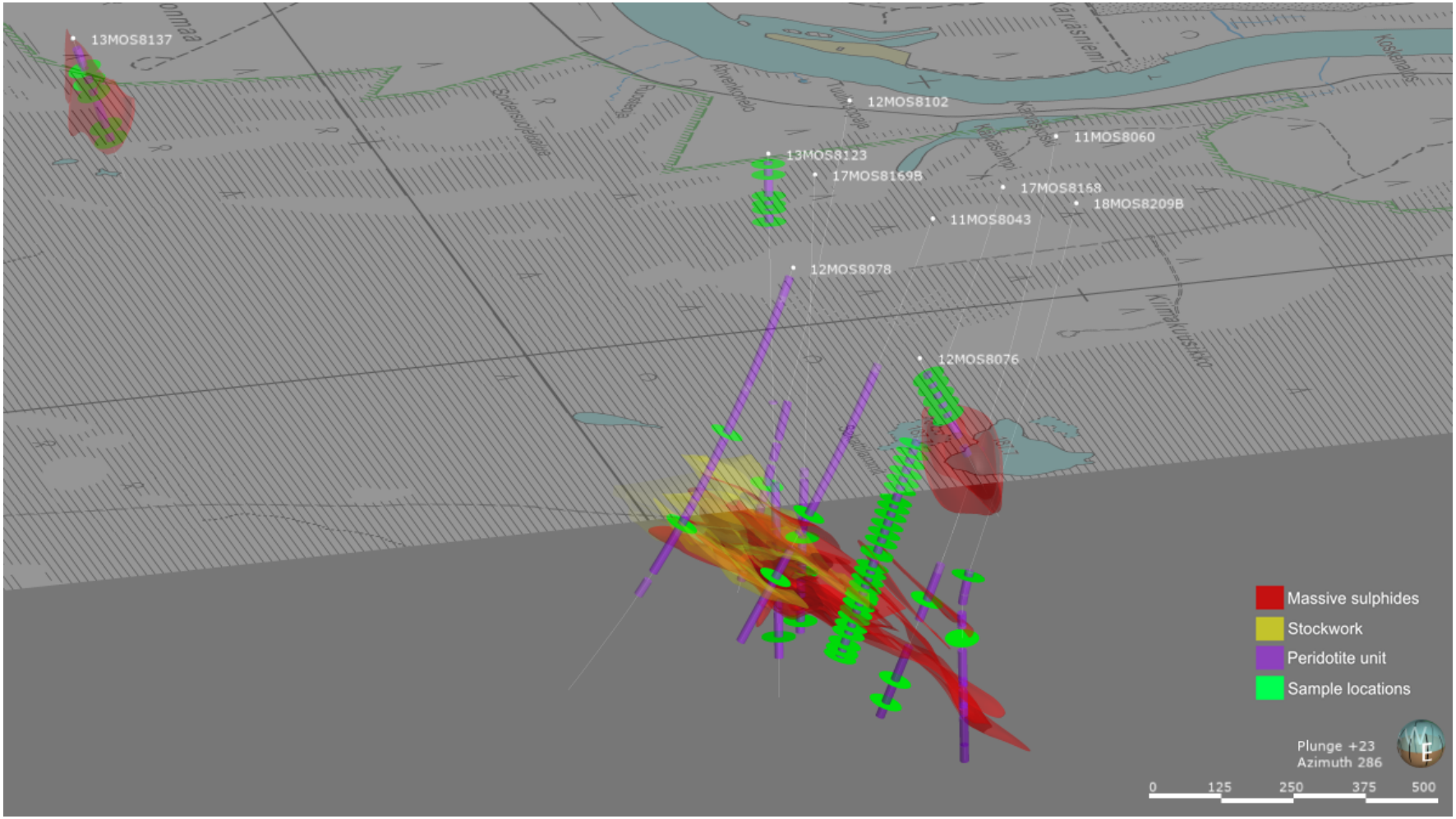

Figure 10. The Sakatti main body (center), the upper body (on top of the main body), the NE body (on the right) and the SW body (on the far left). The purple thick drillhole traces represent peridotite units, the red volumes present massive sulphides and the yellow volumes represents the stockwork zone. Green disks mark the locations of the samples used in this study. Image is looking from East to the West.

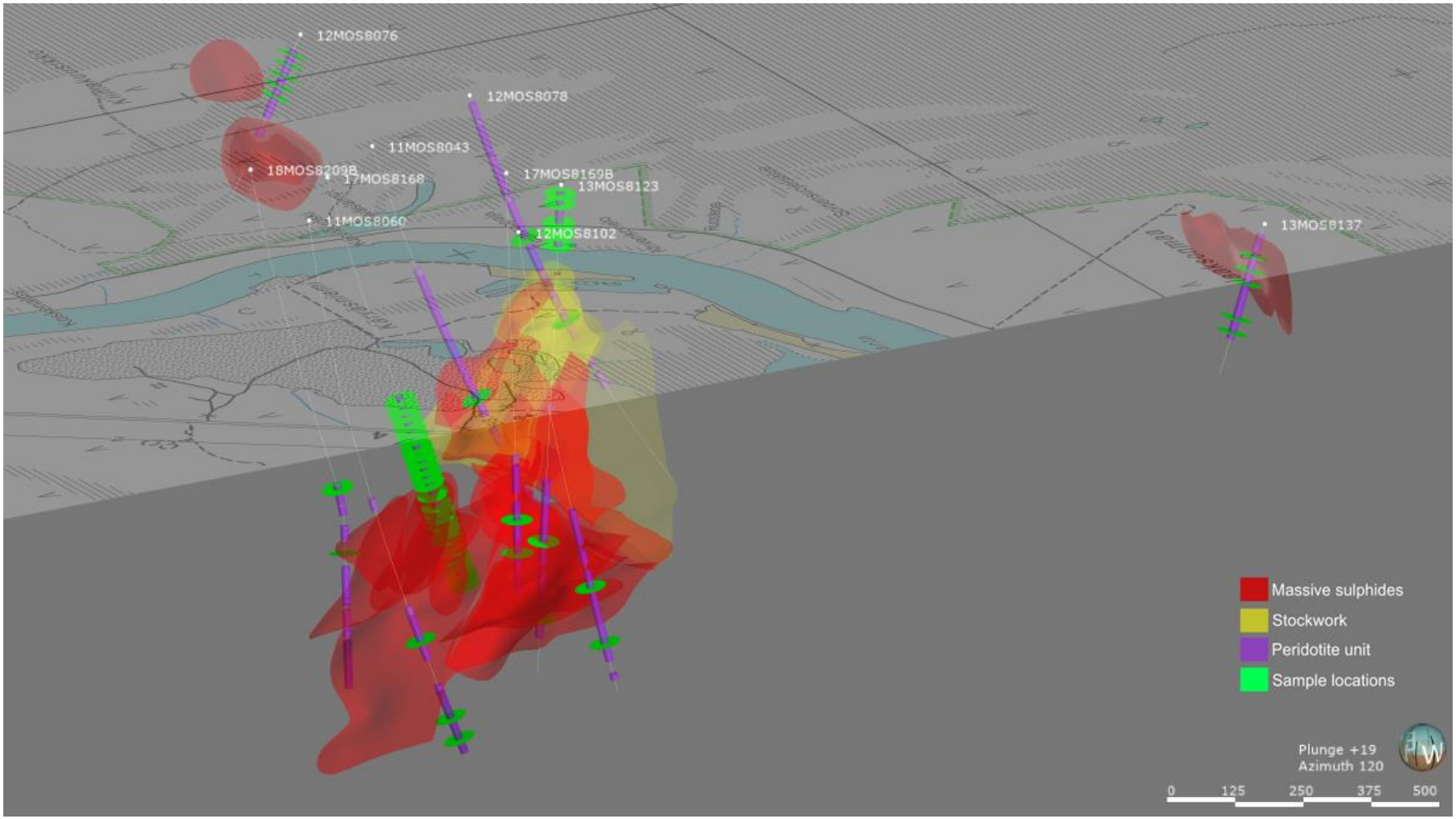

Figure 11. The Sakatti's mineralised bodies, the main (center), the NE (left), the SW (right) and the barren upper body (on top of main body). The purple thick drillhole traces represent peridotite, the red volumes represent massive sulphide lenses and the yellow volumes represents the stockwork zone. Green disks mark the locations of the samples used in this study. Image is looking from northwest to southeast.

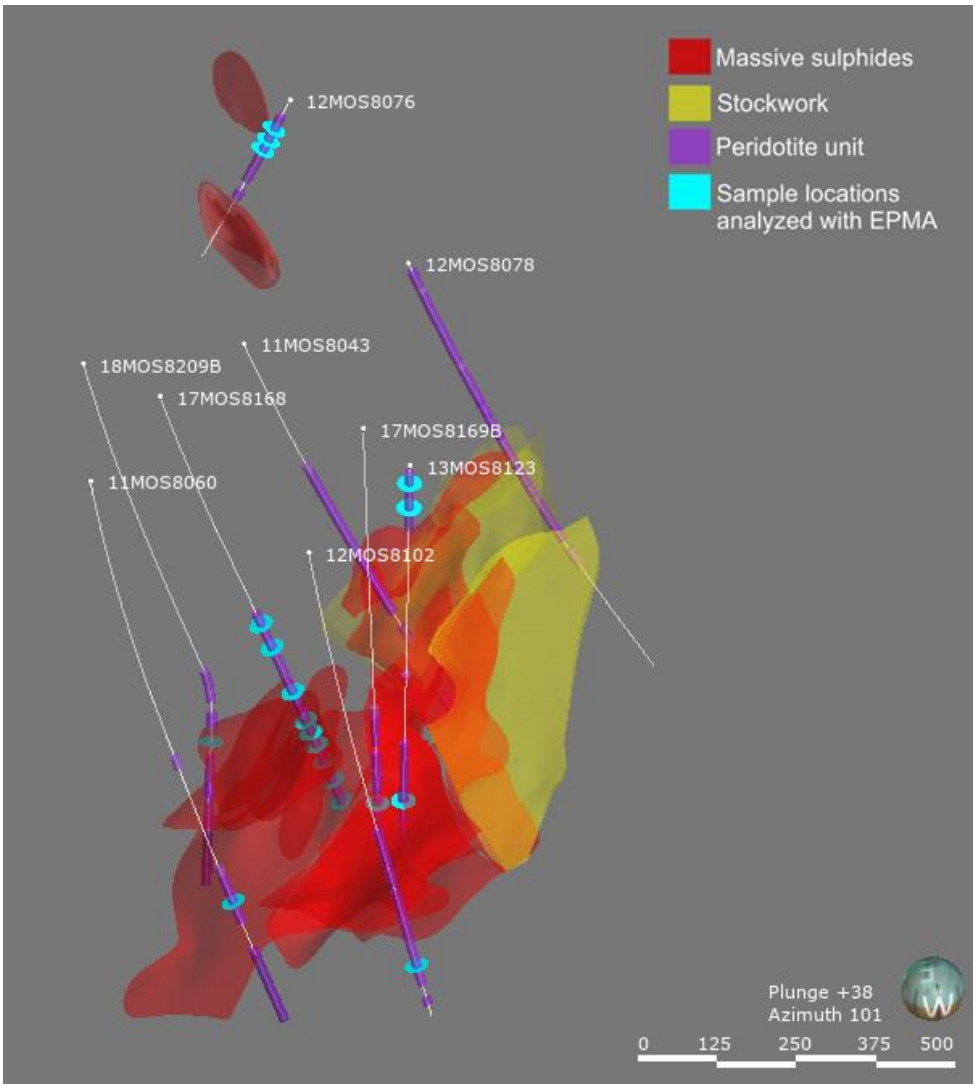

Figure 12. Location of the drill holes 11MOS8060, 18MOS8209B, 17MOS8168, 17MOS8169B, 12MOS8102, 11MOS8043, 12MOS8078 and 13MOS8123 in the main body and one drill hole, 12MOS8076 in the NE body (left corner). Purple thick drillhole traces represents the peridotite units, red volumes represent massive sulphide lenses and the yellow volumes represents the stockwork zone. The turquoise disks mark the exact locations of the samples analysed with EPMA. The drill hole 17MOS8168 is the "profile" hole, where samples have been taken between every intersected massive sulphide mineralisation unit.

4.1.1. Polished thin sections

Drill core samples for the thin sections were selected at the AASMOY where the samples were also sawed to the size of approximately 22 mm x 44 mm x 10 mm. In total, 45 individually packed samples were sent to Vancouver Petrographics Ltd in Canada (VanPetro ltd). A complete list of the samples and their locations can be found from the Appendix 1.

4.1.2. Thick sections

The thick sections were prepared at the laboratory in the University of Helsinki. The selection for the thick sections were based on 1) minimum alteration (low Fe^{3+}, MnO and ZnO contents of the chromites) (Locmelis et al. 2018), 2) the location of the samples and 3) visible primary cumulate textures (Table 4). The selection was based on petrography and mineral chemistry results. Based on the above criteria, two samples were taken above the main body massive sulphides (TS16_SHS18 and TS39_SHS18b) and one below (TS27_SHS18b). The two remaining samples were taken from mineralised bodies South-West (TS05_SHS18) and North-East (TS46_SHS18b) respectively one per each. The thickness of the prepared thick section was 100 microns.

Table 3. Thick section samples from the different mineralised bodies. Lithology 1B = peridotite and 1A = dunite.

Sample ID	Drill hole	Start depth (m)	End depth (m)	Body	Texture	Lithology
TS05_SHS18	13MOS8137	209.48	209.53	SW	orthocumulate	1B
TS16_SHS18	17MOS8168	656.95	657.00	MAIN	orthocumulate	1B
TS27_SHS18b	17MOS8168	808.13	808.18	MAIN	adcumulate	1A
TS39_SHS18b	13MOS8123	718.85	718,90	MAIN	mesocumulate	1B
TS46_SHS18b	12MOS8076	81.90	81,95	NE	orthocumulate	1B

4.2. Methods

4.2.1. Optical petrography

An optical microscope was used to analyse the thin and thick polished sections. From these, the samples' mineralogy, textures, deformation and metamorphic history were determined. After unravelling these features, the representative sections were selected for analysis with the Electron probe microanalyser.

4.2.2. Electron probe microanalyser

Spinel analyses were carried out in the SGL laboratory at the Geological Survey of Finland in Otaniemi, Espoo. In total, 22 representative thin sections from different locations (Figure 9, 10, 11 and 12) were selected for analysis with the electron probe

microanalyser (EPMA) Cameca SX 100. All in all, 96 spots were analysed from Cr-spinels with EPMA. The EPMA is able to determine the chemical composition of a mineral via identifying the X-ray spectra generated by each element in the sample, and comparing those numbers to the spectra generated by a standard sample of known composition. The EPMA has been widely utilised in previous studies in determination of Cr-spinel composition (Barnes 1998, Evans 2017).

The elements SiO_2, TiO_2, Al_2O_3, Cr_2O_3, V_2O_3, FeO, MnO, MgO, CaO, ZnO and NiO were analysed from each Cr-spinel grain using 15 kV accelerating voltage, 20 nA beam current and 1 µm beam diameter from two to five separate spots. In seven samples (TS01_MHP18, TS16_MHP18, TS45_SHS18, TS56_SHS18, 140657, 140778 and 140779), an analytical error occurred resulting in these sections being analysed with a beam current of 40 nA rather than 20 nA, decreasing the detection limits in these samples. The analytical conditions and detection limits are described in Table 5. To guarantee the accuracy of the analysis, at least three spots were analysed from each chromite grain's core. An average composition was then recalculated and is presented in Appendix 2. The majority of the grains were analysed just from the core, in order to analyse the primary chromite composition. In the upper and SW body the grains displayed compositional zoning and from few grains' analysis were taken from the core to the rim.

Table 4. Analytical conditions and detection limits in electron probe microanalyses in GTK's laboratory, Espoo. All the standards are laboratory's in-house standards.

			Range of detection limits (ppm)	
Element	**Line**	**Standard**	**40 nA**	**20 nA**
Si	Ka	Diopside, Astimex	218	253
Ti	Ka	Rutile, Astimex	251	175
Al	Ka	Almandine, Astimex	347	239
Cr	Ka	Chromite, Cr53	460	307
V	Ka	V, Astimex	475	321
Fe	Ka	Hematite, Astimex	601	359
Mn	Kb	Rhodonite, Astimex	2153	1182
Mg	Ka	Diopside, Astimex	495	293
Ca	Ka	Diopside, Astimex	190	140
Ni	Ka	Pentlandite, Astimex	324	201
Zn	Ka	ZnS, Astimex	1293	764

The EPMA data collected was reprocessed according to the method described in Barnes and Roeder (2001) before it was plotted. As the EPMA is unable to detect Fe_2O_3, the value must be calculated. Ferric iron content is calculated based on the stoichiometry as an ideal spinel formula is XY_2O_4, where X = (Fe^{2+}, Ni, Mn, Zn) and Y = (Cr^{3+}, Fe^{3+}, Al). The equation is based on the assumption that titanium is present in the ulvöspinel component and vanadium is appointed to a fictional $Fe_7V_2O_{12}$ component. Iron is split within ferrous and ferric to satisfy the circumstance $n_Y = 2n_X$. Trivalent cations per unit cell are the total n_Y and divalent cations per unit cell are the total n_X. The comprehensive analytical procedure to calculate ferric iron content is described in Barnes and Roeder (2001), and data has been processed according to the methods described by these authors. All geochemistry plots and trivalent cation diagrams were generated in IoGas-64 and in Microsoft Excel.

4.2.3. LA-ICP-MS

The Laser Ablation Induced Coupled Plasma Mass Spectrometer (LA-ICP-MS) is an effective method in analysing trace elements directly from solid geological samples from a percent down to the ppb (parts per billion) level. With this method, accurate trace element values and isotope compositions are acquired requiring only simple sample preparation (Eggins 2003, Liu et al. 2013). This method is also fast (Eggins 2003, Liu et al. 2013, Locmelis 2013) and relatively cost efficient (Liu et al. 2013) when compared to other methods.

A Geolas pro 193nm ArF laser connected to an Agilent 7900 ICP-MS was used to define the ruthenium contents in chromite grains. Ru analysis were carried out in LA-ICP-MS laboratory at the University of Helsinki. The operating parameters are descried in the Table 6. The instrument was calibrated against the NIST standard and the in-house standard. The samples were normalised to UQAC FeS_4 and Cr-content of 208000 µg/g.

Table 5. Operating parameters for LA-ICP-MS analysis.

Laser ablation system	
Instrument	Geolas pro 193nm ArF laser
Energy density	7 J/cm2
Spot size	60 µm
Pulse repetition rate	10 Hz
ICP-MS system	
Instrument	Agilent 7900 ICP-MS
He flow	1050 ml/min
Ar flow	850 ml/min

In total 32 grains were analysed, where in 29 grains both isotopes ^{101}Ru and ^{99}Ru were analysed independently. In the SW body sample, TS05_SHS18, the first three grains were determined only for ^{101}Ru. Sometimes the determined Ru content ratio can be over the natural isotope ratio (^{101}Ru/^{99}Ru = 1.34). The ratio is affected by the interference of ^{101}Ru (Locmelis et al. 2018). In this case ^{99}Ru values were used (TS46_SHS18b) instead of averaged values of both isotopes.

5. RESULTS

5.1. Petrography

All the thin sections have been categorised according to their optical properties in the diamond drill core and in the thin section. In total, five different groups were observed. These groups are the main body ortho- and mesocumulates, the main body adcumulates, the upper body mesocumulates, the NE body ortho-mesocumulates and the SW body ortho-mesocumulates. These textures were described in the Chapter 2.1. The rock type in all of the groups is peridotite. Almost half of the sections (29 sections out of 59 thin sections) fall into the main body ortho- and mesocumulate groups. The main body adcumulate group samples are well preserved and contain primary cumulus minerals. Fresh olivine occurs only in the main body and the NE body samples. In addition, more alteration and pyroxenes are observed in the NE thin sections and they are categorised into their own subgroup. Sulphides occur in the main body; the NE and the SW body samples. The upper body consists of mesocumulates and is free of sulphides. Pervasive

chloritisation is observed in the thin sections taken from the SW body cumulate rocks whereas in the sections from the NE body this type of alteration is observed to be significantly weaker.

Chromite grains are present in all of the thin sections. The size of the analysed grains varies from 100 to 1000 μm. Grains are generally euhedral, however, subhedral to anhedral grains are also observed. Majority of the grains are located within the intercumulus minerals, but chromites also occur inside olivine or olivine pseudomorphs. Typically, chromite grains have an overgrowth of magnetite on the outer rims. In the upper, SW and main body (TS24_SHS18), the chromite grains have outer zones composed from two up to four distinct rims of ferritchromite.

5.1.1. Main body, ortho- and mesocumulates

The samples taken from the main body are located mainly above and between the massive sulphides (Figure 10) or represent the disseminated parts of the main body. Orthocumulate texture is more abundant in the upper parts of the main body and mesocumulate texture is more common in the deeper parts of the main body. The amount of serpentinisation increases towards the surface of the deposit. A complete list of the samples and their locations in the main body are descried in Appendix 3.

The majority of olivine crystals display a clear preferred orientation (Figure 14). Olivine crystals are dark grey to black in the diamond drill core. Interstitial pyroxenes (ortho- and clinopyroxene) fill the intercumulus space. Chlorite veins occur throughout some of the samples (Figure 13). A talc seam commonly surrounds the chlorite veins.

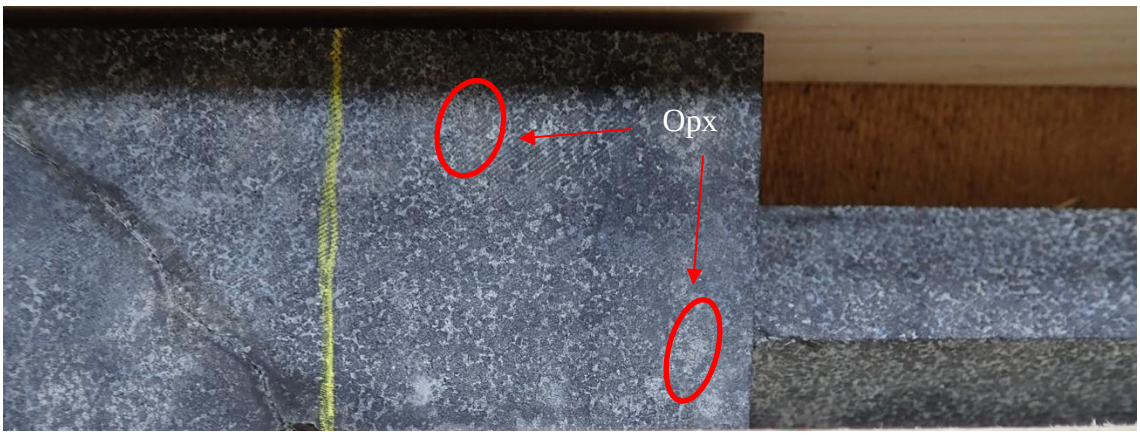

Figure 13. Photo of the sample TS16_SHS18 from the drill core 17MOS8168 (656.95 m). The texture of the rock is orthocumulate. Note the orthopyroxenes inside the red circles. The colour of the orthopyroxenes in the drill core is light pink to light brown. Abbreviations opx= orthopyroxene.

Figure 14. Photo of sample TS56_SHS18 from the drill core 12MOS8102 (837.83 m). The rock is bimodal olivine orthocumulate in texture. Note the clear preferred orientation of the olivine grains and the chlorite vein towards the top of the image, which is filled with chalcopyrite (inside the blue circle) and surrounded by a talc seam. The distance between the two yellow lines is 5 cm.

The Sakatti main peridotite body contains several massive sulphide layers. The contacts between the peridotites and massive sulphide layers is in most locations sharp. Disseminated sulphides are distributed along veins and in interstitial positions. The samples that occur closest to the massive sulphides are more affected by serpentinisation (Figure 15).

Figure 15. Photo of the sample TS24_SHS18 from the drill core 18MOS8168 (773.32 m). Dark bimodal olivine crystals are surrounded by intercumulus. The texture of the rock is olivine orthocumulate. A massive sulphide layer appears soon after the sample location. The distance between the two yellow lines is 5 cm.

The main minerals are cumulus olivine and chromite and interstitial pyroxenes (ortho- and clinopyroxene). Usually, olivine crystals (typically 0.3-3.5 mm in width) are rounded and surrounded by a serpentine mesh texture (Figure 16) or pyroxenes (Figure 17). Olivine crystals are euhedral and their colour varies from black to brownish black in the drill core. Cumulus olivine crystals display orientation and a clear orientation under the optical microscope. Larger hopper-like textured olivine crystals occur in some of the thin sections. Bimodal olivine populations are also common in the subgroup's sections. The amount of fresh olivine and its main alteration product serpentine varies at depth, and between the massive sulphide layers. Two thirds of the pyroxenes are orthopyroxene, the remaining third are clinopyroxenes. Pyroxenes occur as anhedral grains in the intercumulus together with alteration minerals. The amount of relic pyroxene is larger in the samples, where alteration is minimal. Pyroxenes form oikocrysts that surround the olivine grains (Figure 17). The identification of these oikocrysts is easier from the diamond drill core by naked eye (Figure 13), because the grains are partially destroyed and altered in the thin section. Serpentinisation of olivine is ubiquitous (up to 70 % of the mineral) and it occurs in several shapes. Serpentine forms a mesh texture in which it occurs along the olivine fractures and spreads to the rims of olivine, or additionally as flakes that occur as an interpenetrating texture throughout the primary olivine crystal. The mesh texture is mainly composed of serpentine, but also includes talc and chlorite. In the olivine pseudomorphs, the mesh texture has preserved an hourglass center geometry. The colour of serpentine varies from dark grey to blueish grey. Olivine pseudomorphs are easy to identify, because of the well-preserved cumulus texture. Chlorite and talc are common alteration products beside serpentine. Chlorite intersects as veins and replaces pyroxenes in the intercumulus (Figures 16 and 17). Talc appears as clusters of flakes after olivine. Talc is commonly in contact with chlorite and serpentine. Tremolite is an alteration product of clinopyroxene and is replacing the mineral in the intercumulus (Figures 16 and 17). Tremolite has a fibrous habit and high interference colours.

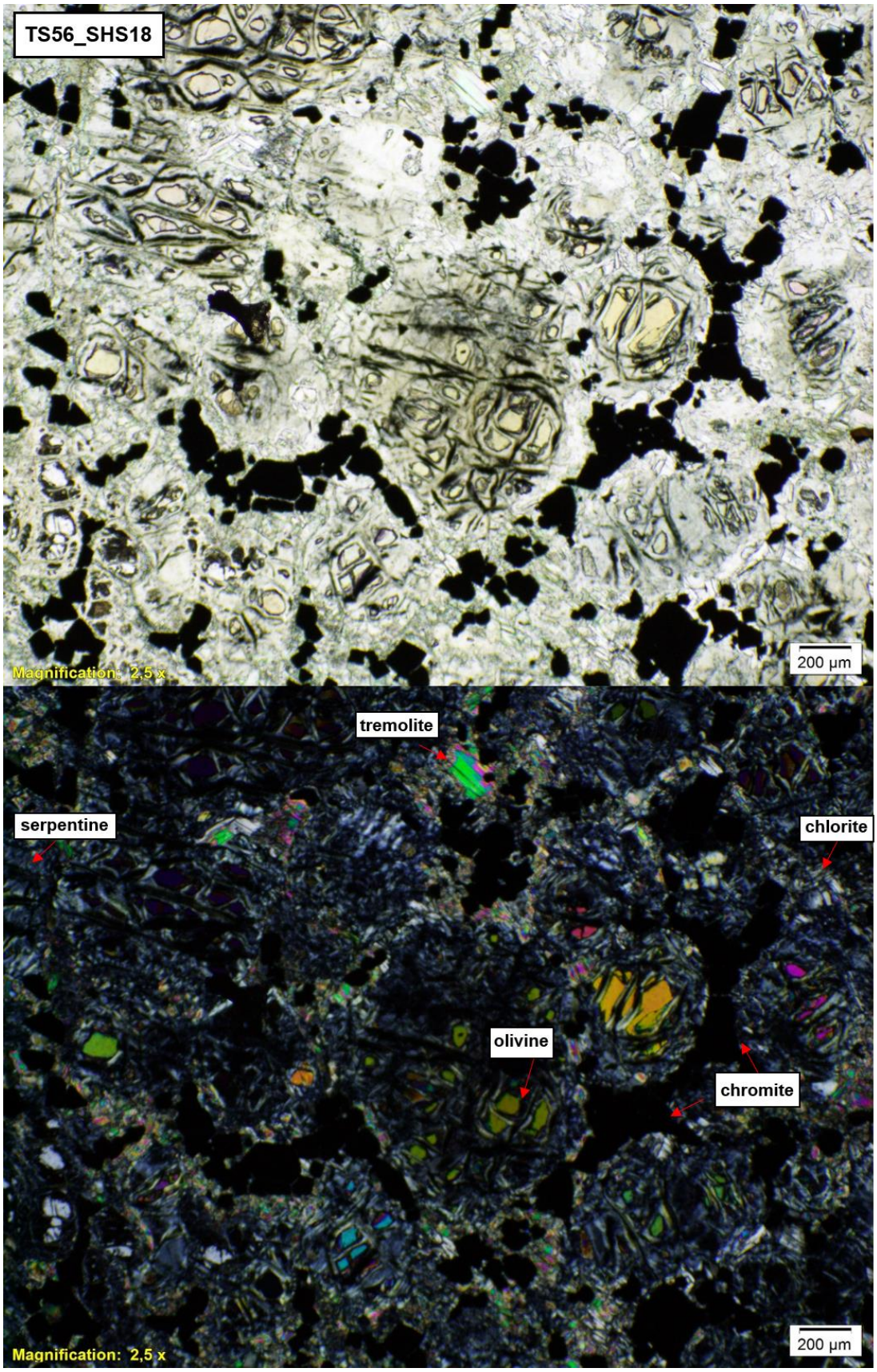

Figure 16. Photomicrograph photo of olivine ortho-mesocumulate (TS56_SHS18 from the drill core 12MOS8102, 837.83 m). Chromite and magnetite aggregates surround the olivine grain boundaries. The intercumulus space is occupied by serpentine, tremolite and chlorite. Upper image taken in plane- polarised light, lower image taken in cross-polarised light.

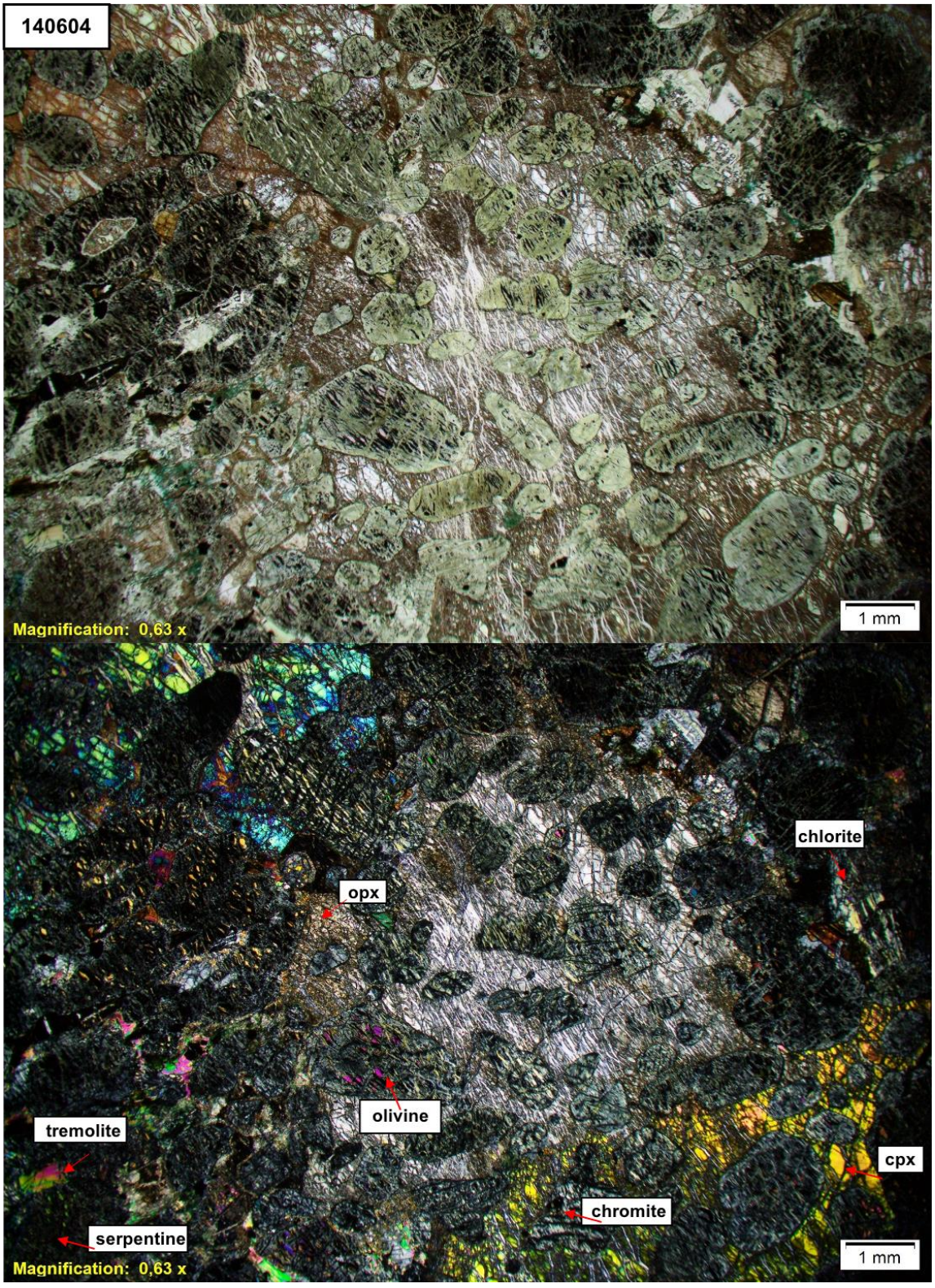

Figure 17. Photomicrographic photo of the sample 140604 from the drill core 13MOS8123 (718.8 m). The rock type is olivine orthocumulate with poikilitic pyroxene. The rock is composed of olivine, serpentine, orthopyroxene, clinopyroxene, chlorite, tremolite and chromite. Upper image taken in plane- polarised light, lower image taken in cross-polarised light. Abbreviations, cpx=clinopyroxene, opx= orthopyroxene.

Generally dark brown to purely opaque chromite grains occur on the grain boundaries of olivine and in the network of other opaque minerals (Figure 16 and 17). Opaque minerals include sulphides (chalcopyrite, pyrite, pyrrhotite), and oxides magnetite and ilmenite. In some sections, the chromites occur inside of both of the pyroxenes or inside of the olivine grains. Chromite grains are typically euhedral, but subhedral grains are also observed (Figure 18). The size of the chromite grains varies approximately between 100 and 750 μm. Some of the chromite grains display a pull-apart texture (Figure 18 a, c-d).

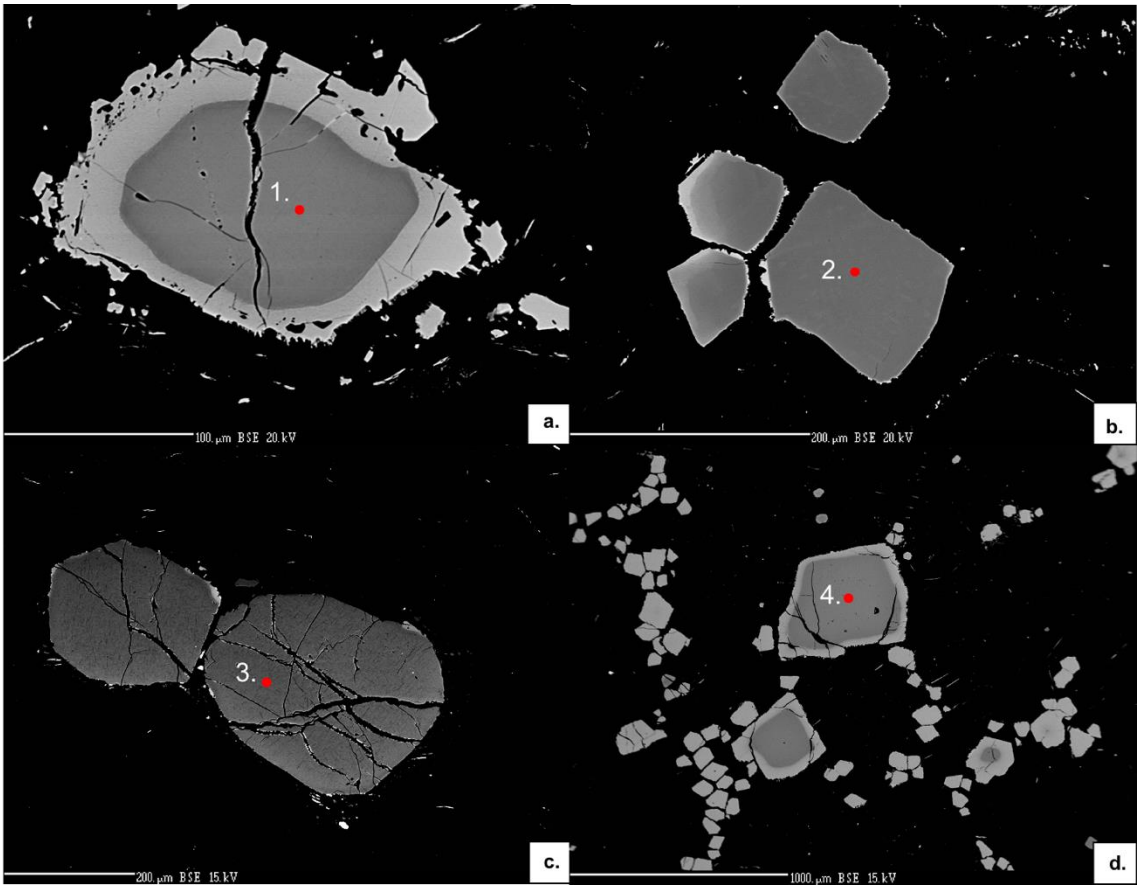

Figure 18. Chromite grains from the main body ortho-mesocumulate group. Samples TS16_SHS18 from the drill core 17MOS8168 (656.95 m), 140604 from the drill core 13MOS8123 (718.8 m) and TS56_SHS18 from the drill core 12MOS8102 (837.83 m). In the section **a)** (TS16_SHS18_b) magnetite overgrowth has created an irregular rim around the primary chromite grain. The grain occurs on the grain boundary of olivine and clinopyroxene. In the section **b)** (TS16_SHS18_d) euhedral chromites have a thin magnetite rim. The grain occurs in clinopyroxene. Small rutile needles are observed in the **c)** (140604_d) chromite grain that occurs inside an olivine crystal. Plate-like needles have one orientation direction. In the sample **d)** (TS56_SHS18_b) chromite (large and darker grains) and magnetite (smaller and lighter grains) has formed clusters around olivine grains. Red points represent the areas analysed by EPMA.

Thin magnetite rim is commonly observed in all of the chromite grains. Between the massive sulphide layers (TS22-TS25_SHS18 from the drill core 17MOS8168, depth between 746.35 and 781.1 meters) chromite grains have two to three different zones of

ferritchromite. Exsolutions of rutile needles occur in one sample (140604_d, Figure 18 c) between the massive sulphides. Needles appear as dark plate-like inclusions inside the chromite grain in the BSE-image, which is situated inside the olivine grain. Rutile needles are aligned with a common crystallographic orientation throughout the grain.

5.1.2. Main body, adcumulates

Adcumulates represent the dunite sub-unit of the main ultramafic cumulate rock body. All together 10 thin sections fell into the adcumulate group category. Adcumulates are located below the massive sulphides in the depth of ca. 800-1100 meters. The adcumulate texture (<10% of intercumulus material, Barnes 2006) can be distinguished both in the drillcore and under the optical microscope (Figure 19 and 20). In the diamond drill core, the dunite is fresh and represents an undeformed rock that is generally lacking sulphides. The surface of this rock type has a coarser feel to it than in other cumulate rock types of the main body. This is explained by the fact that the serpentinisation and the other types of characteristic alteration (chloritisation, tremolitisation, talc-alteration) are either significantly weaker or absent in the dunite/adcumulate unit. The colour of the olivine grains is brownish grey in the drill core.

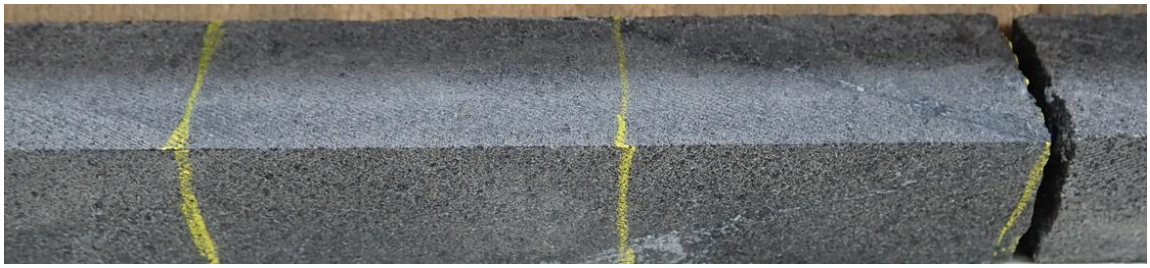

Figure 19. Photo of the sample TS31_SHS19 from the drill core 17MOS8168 (868.9 m). The rock represents the dunite sub-unit of the main cumulate body. Cumulus olivine (dark grains) occurs between the minor intercumulus material in the adcumulate-textured rock. The distance between the two yellow lines is 5 cm.

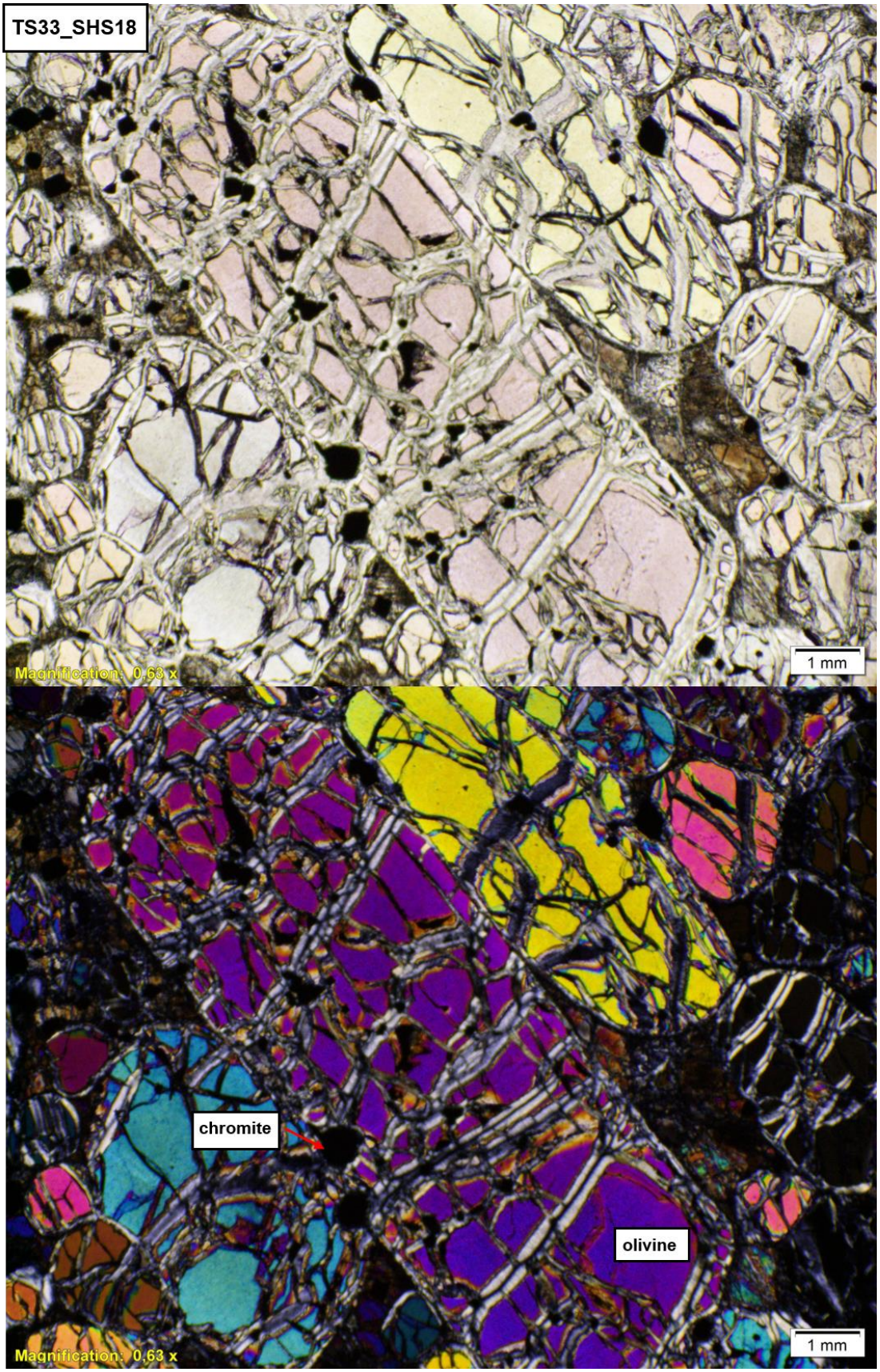

Figure 20. Photomicrograph photo of weakly altered bimodal olivine adcumulate (TS33_SHS18 from the drill core 17MOS8168, depth 894.05 m). Dunite consists of large elongated cumulus olivine grains and the only other cumulus mineral chromite. Upper image taken in plane- polarised light, lower image taken in cross-polarised light.

Olivine and chromite are the cumulus minerals of the adcumulate group. Olivine grains are euhedral and are often oriented. Bimodal olivines are present in half of the sections. Olivine grains display their characteristic fracture patterns and high interference colours (Figure 20). Serpentine mesh and minor talc are the alteration products of olivine. A serpentine mesh occurs along the olivine grain boundaries and fractures. Interstitial orthopyroxene fills the minor intercumulus space together with talc. Sulphides are only present in some of the sections. Chalcopyrite occurs as disseminations at the grain boundaries of olivine (TS33_SHS18 from the drill core 17MOS8168, depth 894.05 m).

Chromite occur along the olivine grain boundaries and as inclusions inside the olivine grains. The majority of the chromite grains represent primary magmatic chromite. Euhedral chromite grains are surrounded by intergrowths of magnetite (Figure 21). In BSE images some chromites have inclusions (likely melt inclusions of olivine or sulphides). The size of the chromite grains varies from 100 μm up to 400 μm, with a mean size of 150 μm.

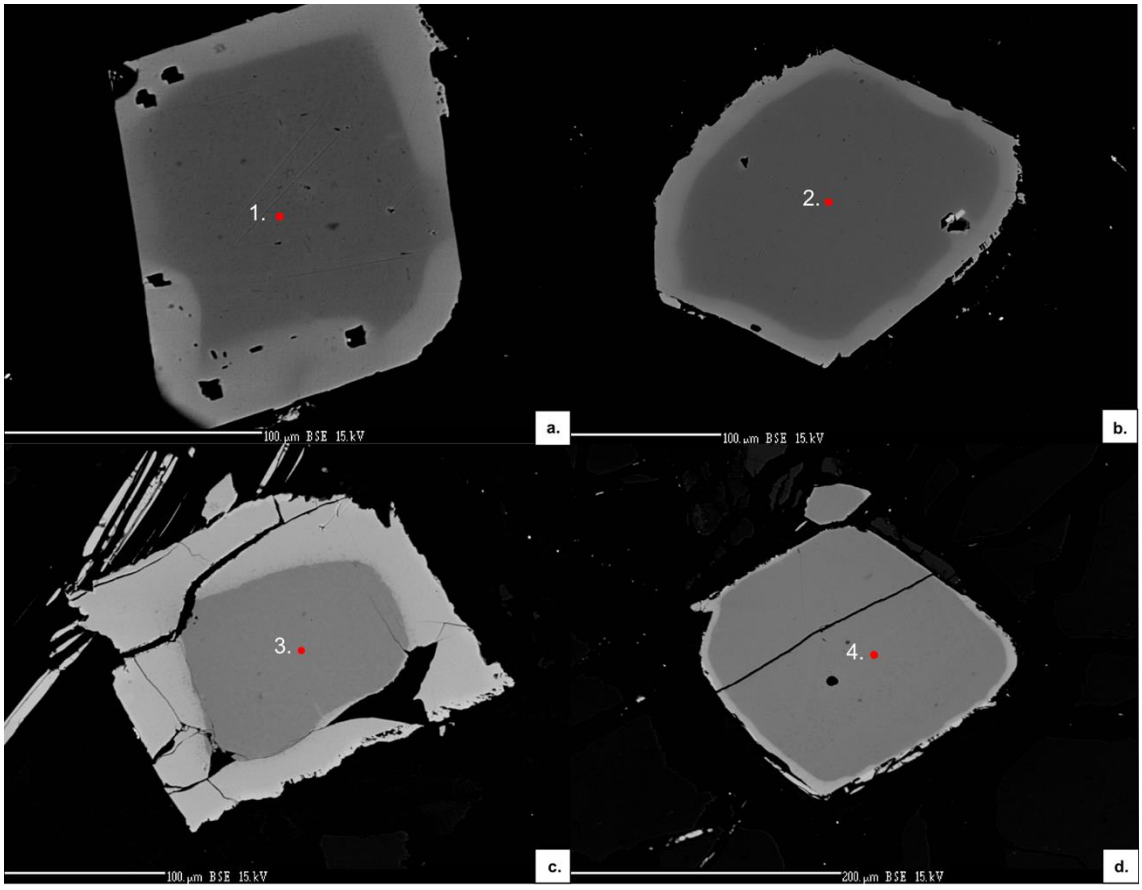

Figure 21. BSE images of chromite grains in the dunite sub-unit in the main cumulate body. Samples TS30_SHS18 (849.22 m) and TS33_SHS18 (894.05 m) from the drill core 17MOS8168. In the images **a)** and **b)** a magnetite rim is surrounding the euhedral chromite grain. The grain **c)** occurs on the alteration rim

of olivine (talc) and has thicker magnetite intergrowth compared to the other chromite grains. In **d)** the chromite grain has an inclusion and fracture inside. Red points represent the areas analysed by EPMA. Point 1 (TS30_SHS18_b), point 2 (TS30_SHS18_c), point 3 (TS33_SHS18_b) and point 4 (TS33_SHS18_d).

5.1.3. Upper body, olivine mesocumulates

The unmineralised upper cumulate body is located on the top of the main body and is enveloped by the Sakatti hangingwall rocktypes. The upper body was sampled with six thin sections taken from the sole diamond drill core 13MOS8123 between the depths of 18 and 122.55 meters. Oriented olivine grains occur in the upper body mesocumulate rock, where alteration products fill the intercumulus space between the grains (Figure 22). The darker mineral – olivine - occurs as aggregates (inside the red circle, Figure 22). Greenish white alteration minerals - talc and chlorite - occur in the intercumulus and also as fracture fillings in the rock.

Figure 22. Photo of the sample TS16_MHP18 from the drillcore 13MOS8123 (90.13 m). Serpentine aggregate after olivine pseudomorphs occur inside the red circle. The texture of the rock is mesocumulate.

Euhedral olivine pseudomorphs occur in aggregates (Figure 23). The mesocumulate texture is well preserved. Chromite occurs as the other cumulus mineral phase together with olivine. The comprehensive serpentinisation of olivine is ubiquitous in the upper body. Serpentinized olivine grains are poikilitic and enclose chromite grains. Talc borders olivine pseudomorphs and occasionally fills the fractures of the olivine pseudomorphs. Chlorite and serpentine are abundant in altered portions of rock. Tremolite and magnetite occur as accessories in the intercumulus. Neither primary olivine nor sulphides are present in these samples.

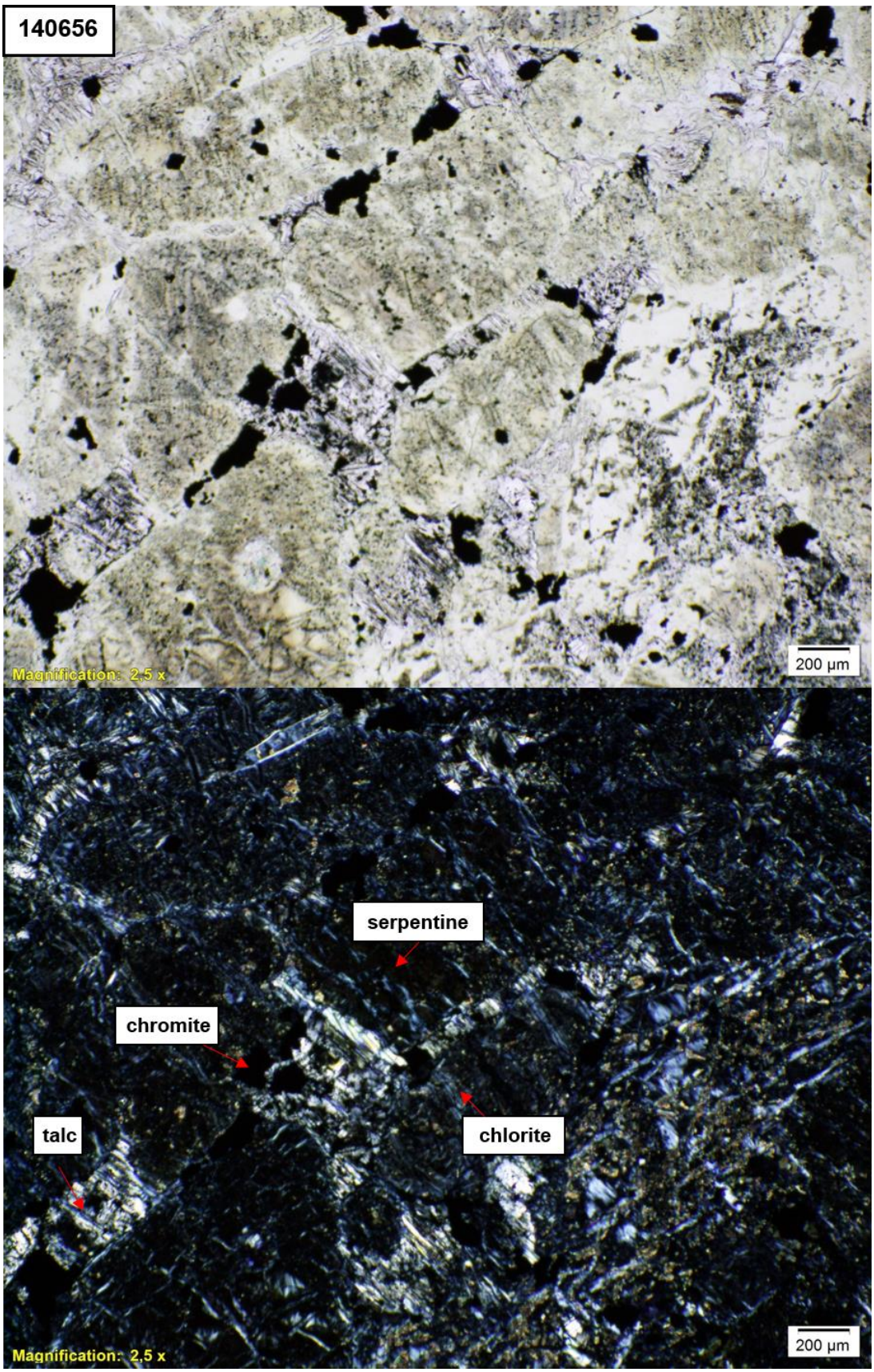

Figure 23. Photomicrograph photo of the thin section 140656 from the drill core 13MOS8123 (18.0 m). The olivine mesocumulate mainly consists of serpentine, chlorite and talc. Chromite is present along the grain boundaries or included in olivine pseudomorphs. Upper image taken in plane- polarised light, lower image taken in cross-polarised light.

Large chromites occur in the grain boundaries of olivine pseudomorphs and as inclusions inside these grains, and thus represent the primary chromites of the rock. Smaller grains in the serpentine mesh are secondary products, as magnetites and are not referred as chromites. The upper body chromites are generally subhedral and compositionally zoned (Figure 24). The size of the grain varies between 150 and 300 μm.

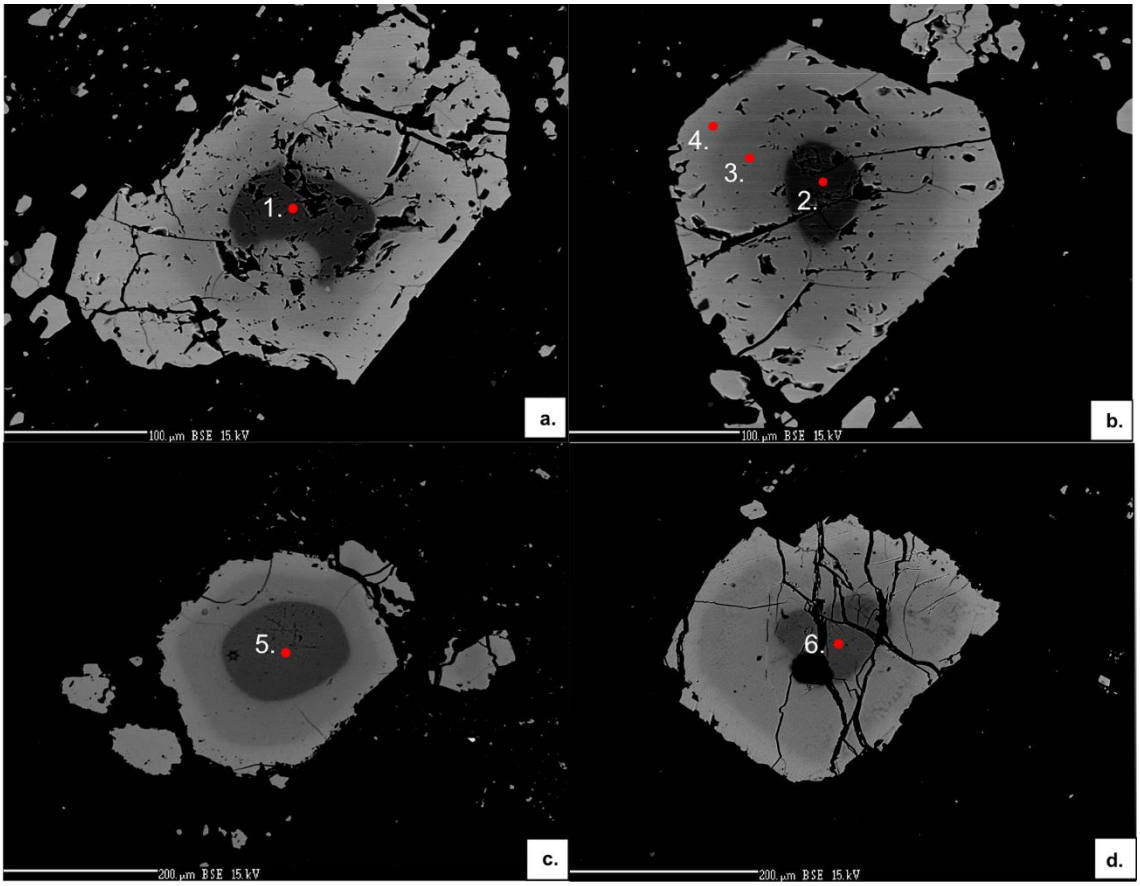

Figure 24. BSE images of chromite grains from the Upper body, drillcore 13MOS8123 from the depths between 37.6 and 90.13 meters. In the image **a)** the altered subhedral chromite grain displays compositional zoning and irregular grain boundaries. The same features are observed in the grain **b)**, which represents the typical chromite grain in the upper body. The euhedral **c)** grain has least alteration compared to other grains. The chromite grain **d)** is fractured through the whole grain. Red points represent the areas analysed by EPMA, starting from the point 1 (140657_c), point 2 (140657_e_core), point 3 (140657_e_rim1), point 4 (140657_e_rim2), point 5 (TS16_MHP18_c) and point 6 (TS16_MHP18_e).

5.1.4. North-East body, olivine ortho- and mesocumulates

The NE satellite ultramafic cumulate body is located to the north-east from the main peridotite body. All of the NE body samples are taken from the same drill core 12MOS8076 (Figure 12). The texture in the first two samples from the NE body are mesocumulates (140777 and TS45_SHS18) from the depths between ca. 39 and 60 meters. The other three orthocumulate thin sections (140778, 140779 and TS48_SHS18)

are taken from the depths between ca. 80 to 123 meters. Interstitial orthopyroxene pseudomorphs (light pink in drill core surface) surrounds olivine pseudomorphs (dark) in the diamond drill core (Figure 25). The rock is composed of olivine, serpentine-group minerals and pyroxenes. Several generations of serpentine veins crosscut the rock. Sulphides are observed in these samples visually in the diamond drill core. The massive sulphide layers occur deeper in the NE body, but not in the immediate vicinity of the samples (Figure 12).

Figure 25. Photo of the sample 140779 from the drill core 12MOS8076 (102.65 m). Cumulus olivine (darker minerals) are surrounded by interstitial orthopyroxene pseudomorphs (light pink inside the red circle) and alteration minerals (greenish grey). The texture of the rock is orthocumulate.

Olivine is the main cumulus phase and it occurs as euhedral to subhedral grains (Figure 26). Olivine crystals are strongly fractured, forming fragments with a mesh texture. The mesh texture is composed of serpentine and chlorite. Serpentine is occasionally radial in texture. The serpentine mesh in olivine pseudomorphs displays an unusual green colour in both plain and crossed-polarised light, indicating a Fe-bearing serpentine variant. Hopper-textured olivine crystals are observed in some of the sections. Clino- and orthopyroxene alongside plagioclase represent the primary intercumulus minerals. Serpentine, talc and chlorite have obliterated the primary minerals such as olivine and pyroxene(s). Occasionally clinopyroxene is altered to tremolite. Magnetite, pentlandite, chalcopyrite and pyrrhotite occur as accessory minerals.

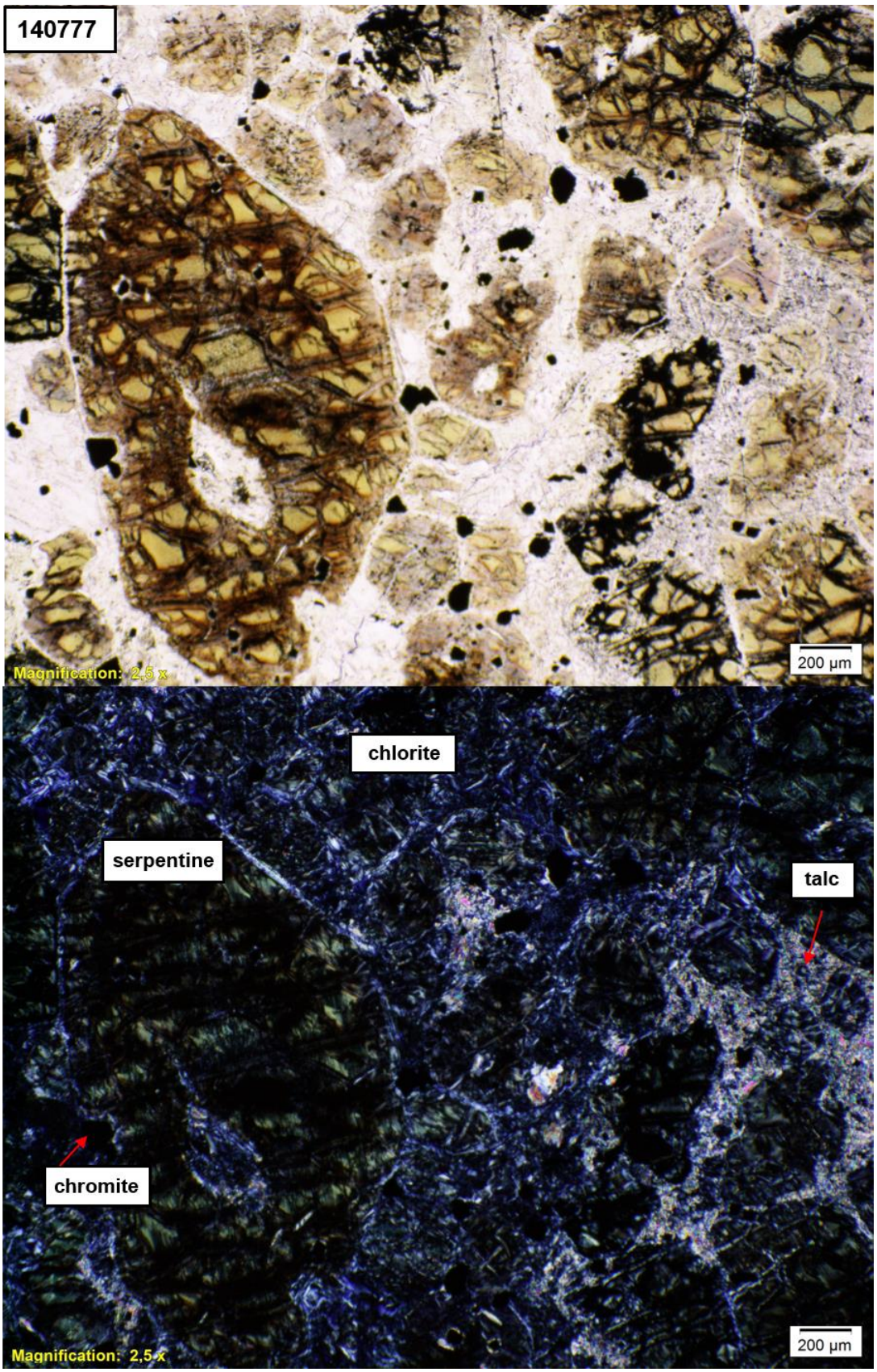

Figure 26. Photomicrograph of serpentinised olivine orthocumulate in the NE body (140779 from the drill core 12MOS8076, depth 102.65 m). Hopper-like textured olivine pseudomorphs are replaced by mesh textured serpentine and talc. Chromite grains occur inside olivine pseudomorphs, grain boundaries of other minerals and in intercumulus. Upper image taken in plane- polarised light, lower image taken in cross-polarised light.

Euhedral to subhedral chromite grains occur inside olivine or olivine pseudomorphs and are observed enclosed by clinopyroxene. In addition, chromite grains also occur on the grain boundaries of olivine. The more primary chromite cores comprise up to 95 % of the total grain areas (Figure 27). Secondary magnetite surrounds the outermost rims of the chromite grains. Generally, the rims of the grains are smooth but one grain (Figure 27 d) has lost its euhedral shape and has a symplectite texture. Some of the grains are in contact with sulphides or have melt inclusions. The size of the grains varies between 100 and 1000 μm with an average size of ca. 250 μm.

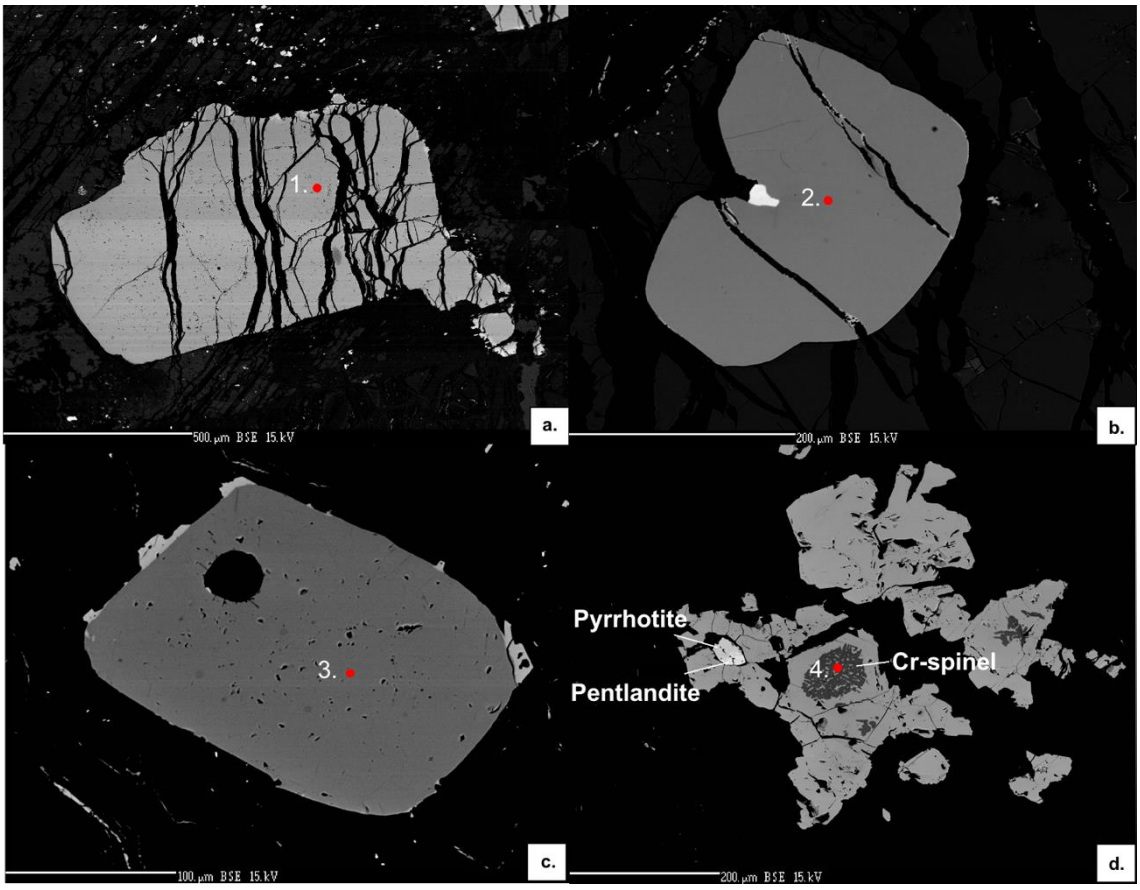

Figure 27. Chromite grains from the NE body. **a)** subhedral chromite grain, **b)** chromite is attached to chalcopyrite (bright white), **c)** chromite occurs inside olivine and has melt inclusions and **d)** grain, where chromite occurs next to sulphides, pentlandite (brighter) and pyrrhotite (darker) and has lost its euhedral shape. This texture is called symplectite, Red points mark the areas analysed by EPMA, starting from the point 1 (140778_b), point 2 (140779_b), point 3 (140779_c) and point 4 (140779_e). Samples 140778 and 140779 from the drill core 12MOS8076 (depths between 81.85 and 102.65 m, respectively).

5.1.5. South-West body, ortho- and mesocumulates

The mineralised SW satellite body is located to the southwest of the main body (Figure 8). All the samples represent olivine ortho- and mesocumulates. The samples have been

taken from the same drill core, 13MOS8137, from the depths of ca. 60 and 210 meters. Cumulate olivine grains display a clear orientation in the diamond drill core (Figure 28). Cumulate olivine grains are euhedral or subhedral. Intercumulus material is filled with serpenitinisation minerals (serpentine, talc and chlorite). Chromite or sulphides are not observed with the naked eye.

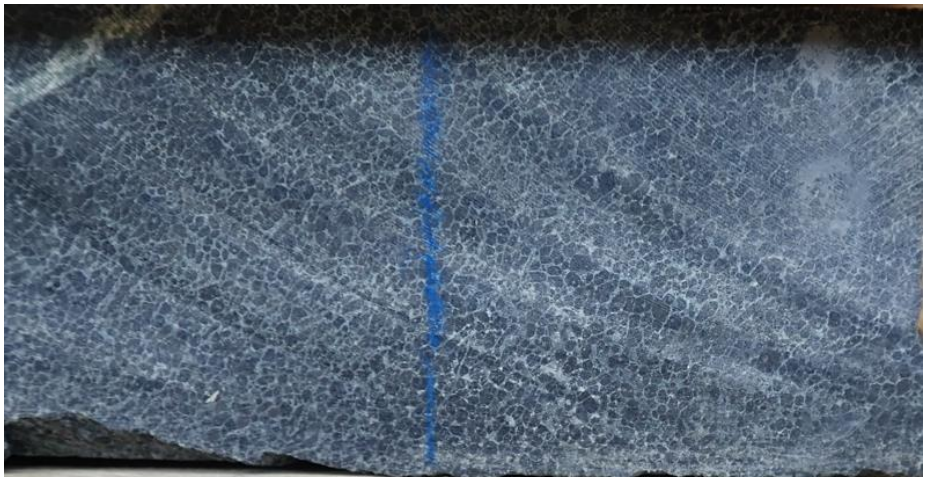

Figure 28. Photo of sample TS05_SHS18 from the drill core 13MOS8137 (209.48 m). Olivine grains display clear orientation. The texture of the rock is mesocumulate.

Unaltered magmatic olivine or pyroxenes are not observed in the SW body, as these minerals are pervasively altered. Primary cumulate textures (ortho-mesocumulate) are still preserved as the alteration minerals have retained the original shape of the magmatic minerals. Olivine pseudomorphs are surrounded by serpentine, talc and chlorite. Serpentinisation of olivine is pervasive (to almost 100 %) (Figure 29). Serpentine displays a mesh texture, where the flakes are oriented and sometimes radial. The interference colours of serpentine are sometimes blueish to greenish grey. Serpentine is associated with chlorite that outlines the olivine pseudomorphs. The contact between these two minerals is relatively sharp. The amount of chlorite in the cumulate rocks is greater in the SW body than in the other peridotite bodies in Sakatti (Figure 29). Talc occurs with serpentine and chlorite in the alteration mineral assemblage. Talc is observed as flakes after pyroxene. Tremolite is occasionally replacing original clinopyroxene.

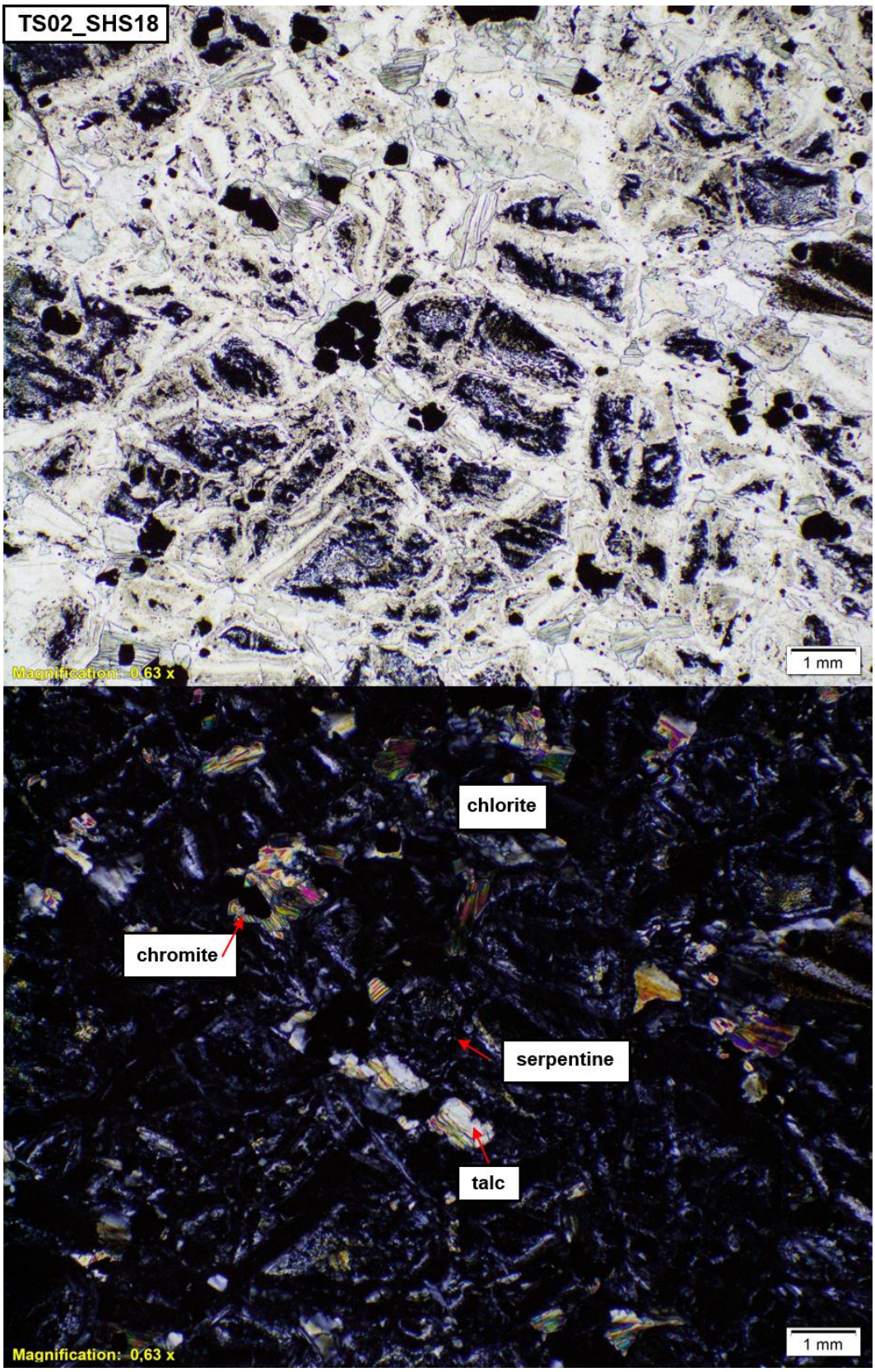

Figure 29. Photomicrograph of the olivine ortho-mesocumulate rock (TS02_SHS18 from the drill core 13MOS8137, depth 89.55 m) from the south-west cumulate body. The rock is strongly serpentinised, but has kept its primary olivine cumulate texture. Chromite grains occur in the intercumulus and in the grain boundaries of the olivine pseudomorphs. Talc and chlorite assemblage fill the intercumulus space. Serpentinisation of olivine is pervasive. Upper image taken in plane- polarised light, lower image taken in cross-polarised light.

Chromite grains in the SW ultramafic cumulate rocks are subhedral or euhedral, nearly opaque to dark brown and have high relief. Chromites are usually fractured and irregularly corroded. Grains have compositional zoning, with two up to four zones (Figure 32). Chromite grains occur as clusters within the olivine pseudomorphs and their original magmatic grain boundaries. The size of the chromite grains varies from 200 μm to 600 μm, with an average size of ca. 250 μm (Figure 30).

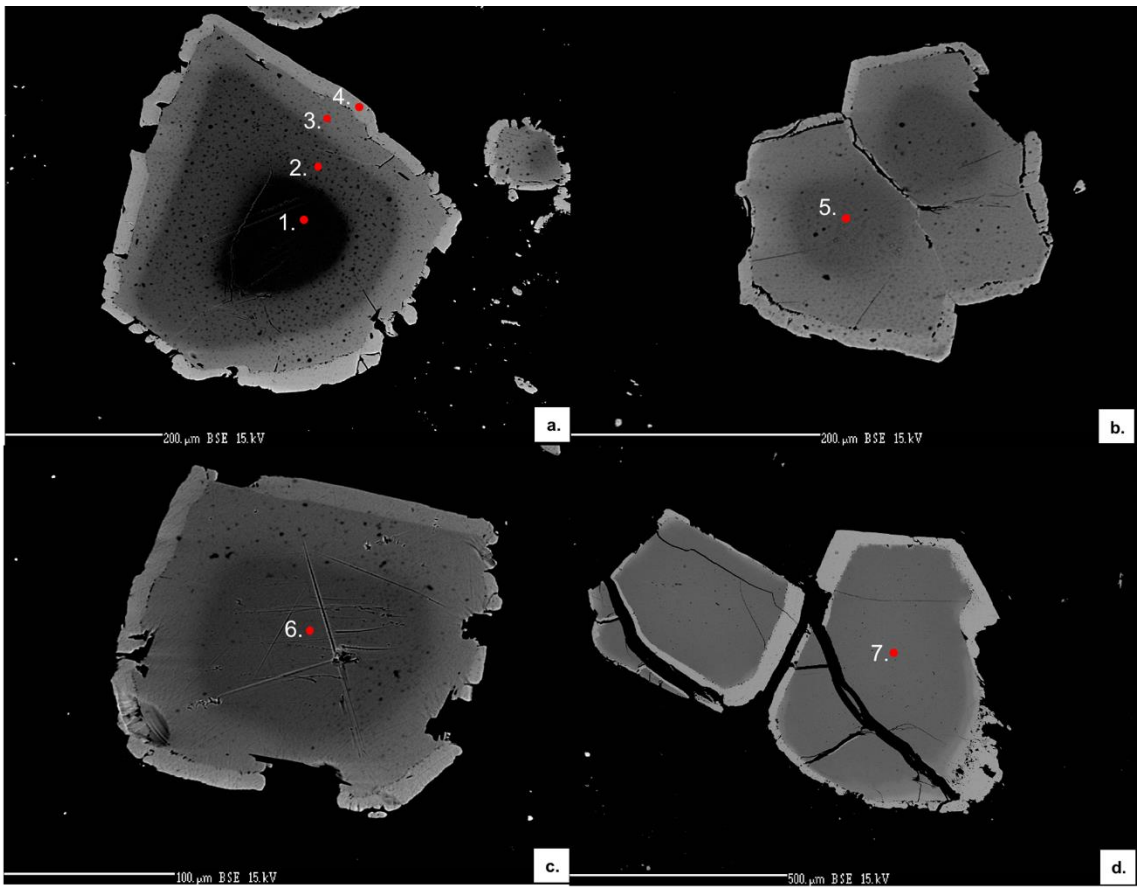

Figure 30. BSE images of chromite grains from the SW body from the drill core 13MOS8137, at the depths 89.55 m, 182.34 m and 209.48 m (TS02_SHS18, TS01_MHP18 and TS05_SHS18, respectively). **a)** Compositional zoning of the euhedral chromite grain. In total, the grain has four zones. **b)** Intergrowth of two euhedral chromite grains, where the outermost rim is secondary magnetite, **c)** euhedral chromite grain has an irregular magnetite rim and **d)** the chromite grain has a pull-apart texture and one secondary magnetite rim. The size of the grains varies between 200 to 600 μm. Red points mark the areas analysed by EPMA. Starting from point 1 (TS05_SHS18_a_core), point 2 (TS05_SHS18_a_rim1), point 3 (TS05_SHS18_a_rim2), point 4 (TS05_SHS18_a_rim3), point 5 (TS02_SHS18_a), point 6 (TS05_SHS18_d) and point 7 (TS01_MHP18_c).

5.2. Chemical composition of chromite

Cr-spinels in the Sakatti olivine cumulate rocks were principally analysed within the core of the grains. Occasionally rims and zones were analysed from the upper (140657) and

SW bodies (TS05_SHS18). The analysed Cr-spinels were classified on the basis of their trivalent cation compositions. The majority of the analysed points (76) plot within the field of chromite, while 23 analyses plot to the field of magnetite, with one sample plotting within the spinel field (Figure 31). The main body ortho-mesocumulate samples plot within the field of primary igneous chromite (blue field) and only some samples are enriched in Fe^{3+}, plotting within the border of magnetite and following the FeTi trend. Magnetites and some chromites follow the modified trend (dashed line). The main body adcumulates plot within the primary igneous chromite field. The upper body samples plot within the primary field and the rest of the upper peridotite body samples follow the curve of metamorphosed chromites. Sample compositions from NE body can be found from all of the trivalent cation fields, but mostly plot within the primary igneous chromite field. As a result of these findings, this study will only focus soley on chromites from this point onwards. All analysist data acquired by the EPMA instrument is available in Appendix 1 and the sample list in Appendix 3.

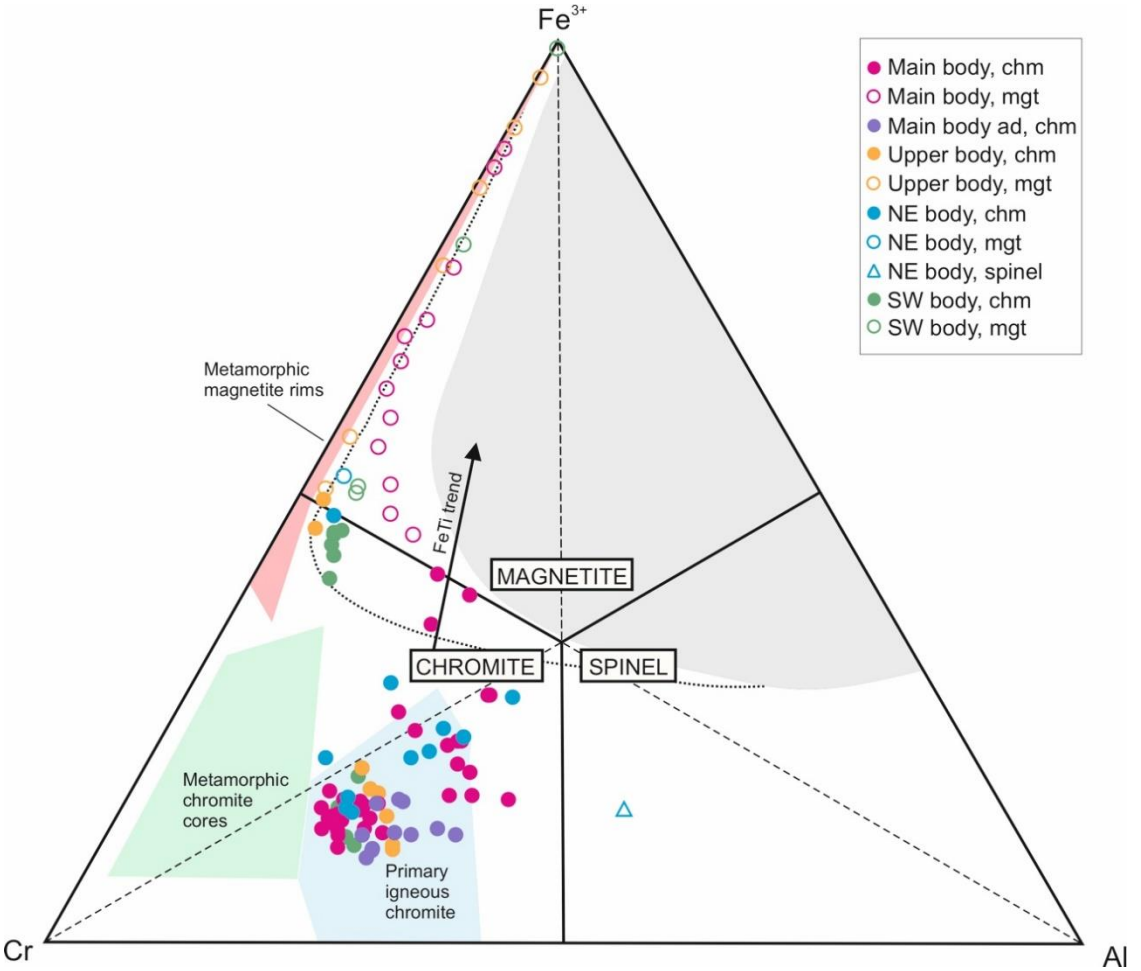

Figure 31. All analysed Cr-spinels plotted on a Fe^{3+}- Cr – Al trivalent cation diagram. Chromites have been plotted as filled circles, magnetites as outlined circles and the sole spinel as a triangle. Fields are drawn after Barnes et al. (1996). The FeTi trend is after Barnes and Roeder (2001). Abbrevations, chromite=chm, magnetite=mgt.

5.2.1. Major elements

The major elements in Cr-spinel are Mg, Fe, Al and Cr. Mg# varies between all the bodies, and differs also when comparing main body ortho-mesocumulates and adcumulates (Figure 32). The largest variation in Mg# is observed in the main body ortho-mesocumulates (0.18- 0.56). In the main body adcumulate Mg# varies between 0.31 and 0.45. Both the upper and SW body form groups on the diagram, where the analyses belonging to the first group have similar Mg# as the main body ortho-mesocumulates, and the representatives of the other compositional group have the Mg# values closer to magnetites. Interestingly, the NE body chromites have similar variation in their Mg# compared to the main body ortho-mesocumulates (0.19- 0.44). When Mg# and Fe^{3+}# are plotted together (Figure 32), a trend is shown where Fe^{3+}# increases and Mg# decreases can be observed. All other groups have elevated Fe^{3+}# values, aside from the main body adcumulates. In these groups the Mg# value is lower.

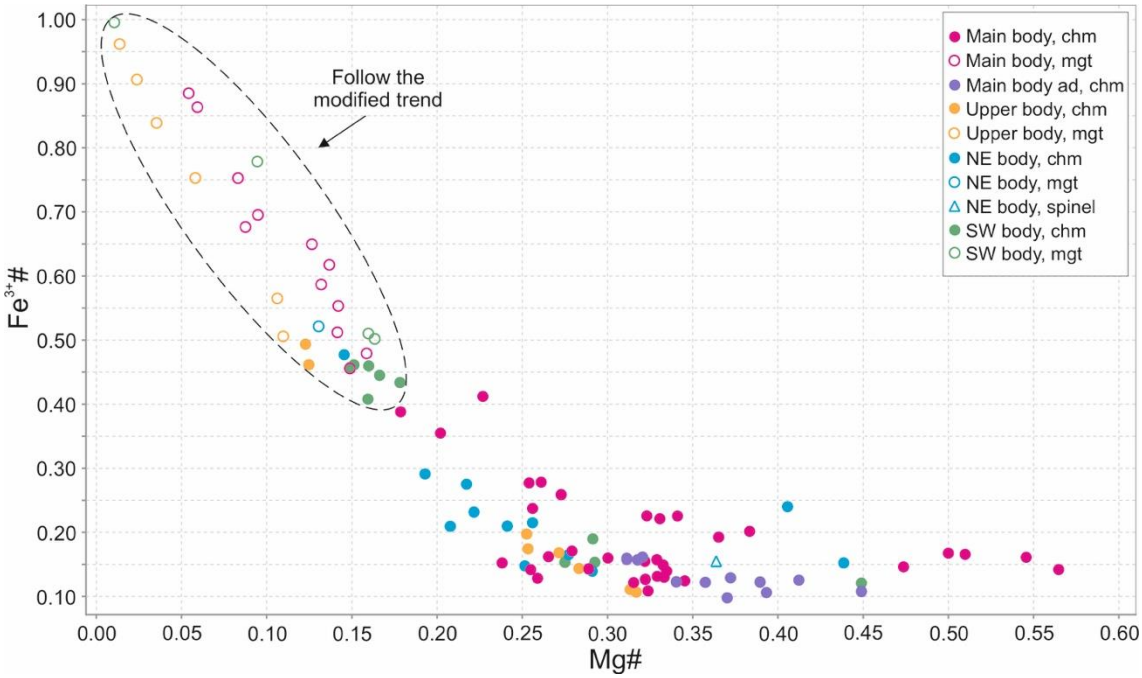

Figure 32. Mg# vs Fe^{3+}# plot of analysed Cr-spinels. Fe^{3+}# increases while Mg# decreases. The samples inside the dashed line follow the modified trend in the trivalent cation diagram (Figure 31).

The Fe^{3+}# of chromites varies between the bodies (Figure 32). The main body adcumulate group displays the minimum variation in the Fe^{3+}#, between 0.11 and 0.16. The main body ortho-mesocumulates form a narrow cluster, and the rest have higher concentrations

of Fe^{3+}#, from 0.11 up to 0.41. The Fe^{3+}# varies between 0.15 and 0.29 in the NE body. In addition, one sample from the NE body has a Fe^{3+}# of 0.48. Similarly, as with Mg#, the upper and SW bodies form two distinct groups. One group is Fe^{3+}#-poor and the other is Fe^{3+}#-rich.

The majority of the samples (main body ortho-mesocumulates and NE body) have Al# between 0.17 and 0.37 (Figure 33). Al# in chromites within adcumulates varies between 0.24 and 0.34. Chromites from the upper body and the SW body plot within two groups, where the other is depleted in Al#. When Fe^{3+}# and Al# are plotted, chromites are enriched in Fe^{3+}# when Al# decreases.

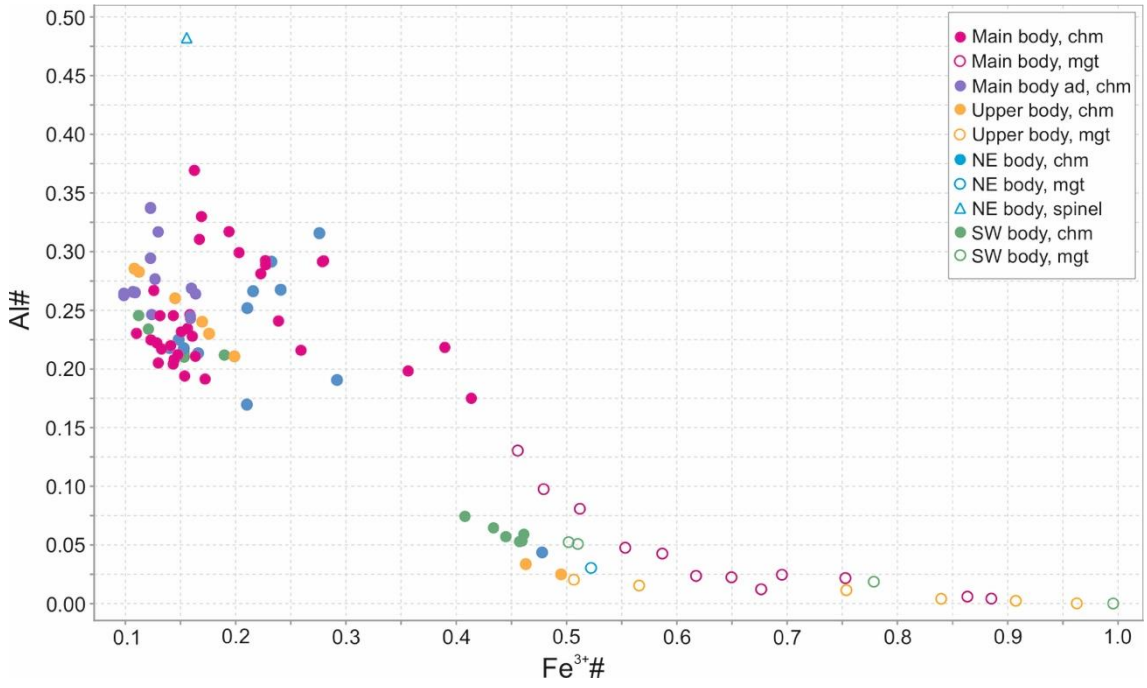

Figure 33. Fe^{3+}# vs. Al# plot of analysed Cr-spinels.

The Harker plot Mg# versus Al# displays (Figure 34) a linear trend, when Mg# ranges between 0.2-0.55. When Al# increases, Mg# increases. The main body ortho-mesocumulates and adcumulates generally follow this linear trend. The NE body chromites do not correlate with the general trend, and some of these chromites have elevated concentrations of Al#.

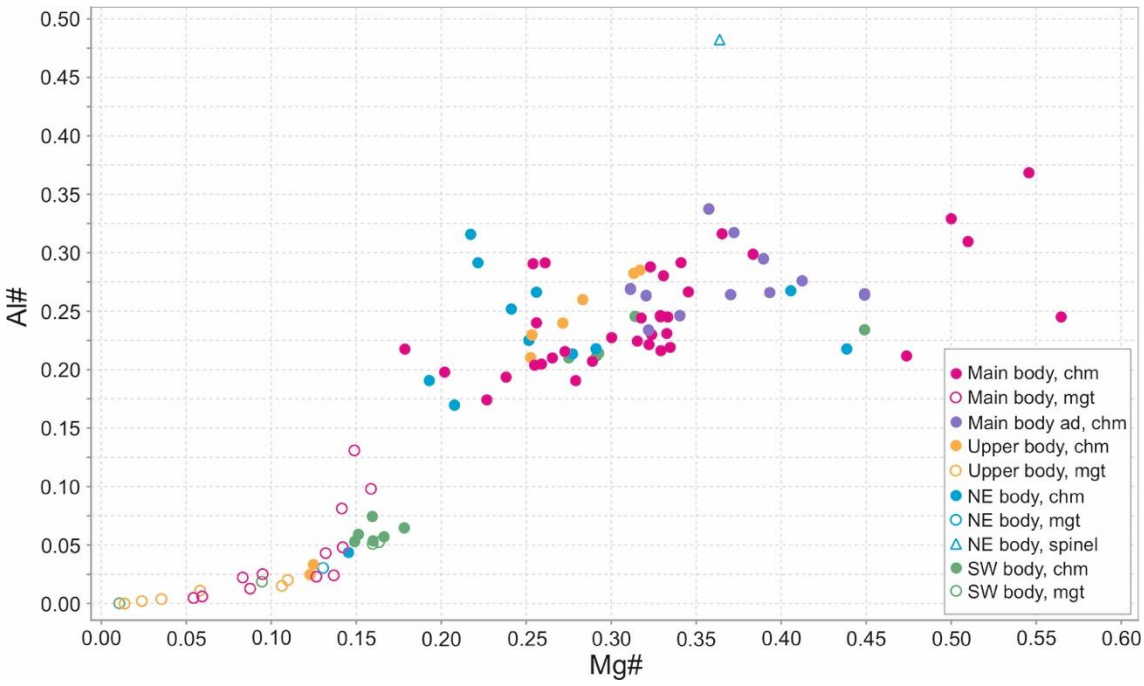

Figure 34. Mg# vs Al# plot of analysed Cr-spinels.

When considering Cr# the main body ortho-mesocumulates values vary between 0.56 and 0.77. A similar variation is observed in the NE body chromites (0.56- 0.79 and one point 0.92). The adcumulate group displays the least variation in Cr# with values ranging between 0.62 and 0.71. Most of the chromites from the SW body and the upper body have relatively high Cr# values, between 0.72 and 0.90, and between 0.68 and 0.95, respectively. At the Mg# and Cr# Harker plot (Figure 35), the majority of the chromites plot within the same cluster, where Mg# varies between ca 0.25 and 0.35 and Cr# stays constant between 0.5 and 0.7. In the analysed Sakatti chromites, from point to point, Fe^{3+}# varies between 0.10-0.50, whereas the variation in the Cr# is smaller with maximum differences being between 0.56 and 0.77 (in the main peridotite body ortho-mesocumulates) for any given Fe^{3+}# (Figure 36).

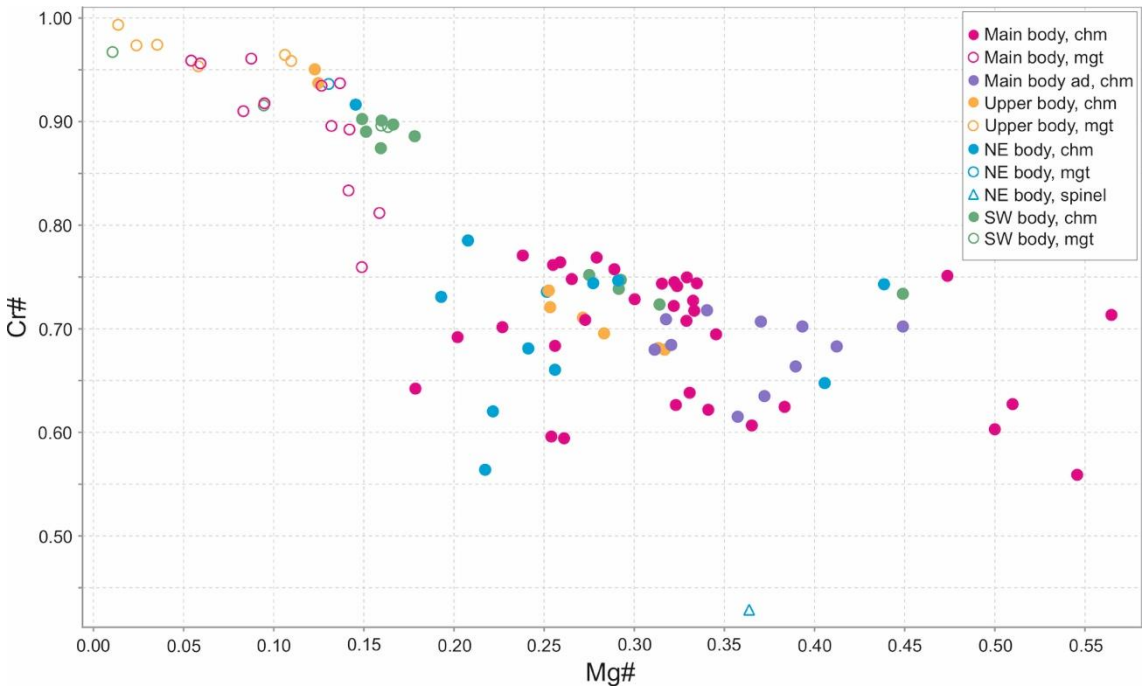

Figure 35. Mg# vs Cr# plot of analysed Cr-spinels.

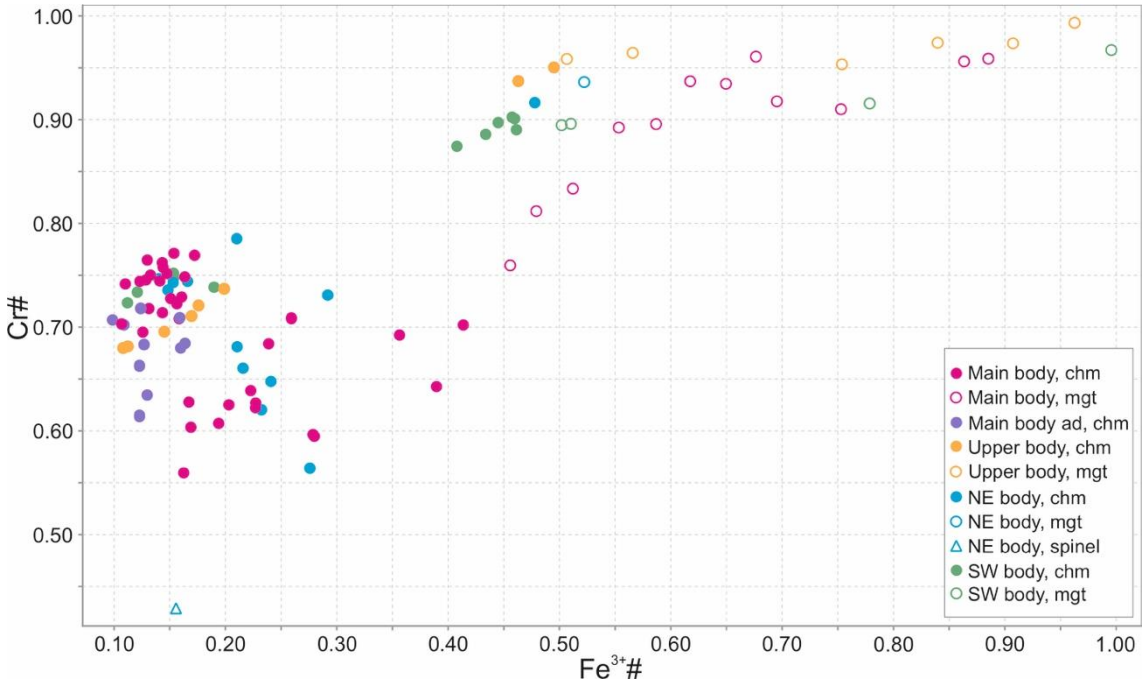

Figure 36. Fe^{3+}# vs Cr# of analysed Cr-spinels.

5.2.2. Minor elements

Minor elements in Cr-spinel of the Sakatti olivine cumulate rocks include MnO, V_2O_3, ZnO, NiO and TiO_2. In general, the majority of the variation in chromites with respect to minor elements contents occurs when #Mg varies between ca. 0.25-0.35 (Figures 37 and 38). However, in the case of the MnO a more pronounced correlation can be observed on the Mg# vs. MnO plot. The Mg# increases with decreasing MnO content. The main body ortho-mesocumulates and the NE body chromites displays the largest variation in the MnO content. In the main body adcumulates, MnO only varies between 0.21 and 0.37. A weak positive correlation can be distinguished between Mg# and V_2O_3 when the V_2O_3 content is in the range of 0.08 – 0.21 (Figure 37). In cases where the calculated Mg# is in the range of ca. 0.25 – 0.35 enriched levels of V_2O_3 can be seen to be present in some chromites from the main body ortho-mesocumulates, as well as in some from the upper and NE body samples. The analysed Sakatti chromites display a correlations in their ZnO, NiO and TiO_2 compositions when plotted against the Mg# (Figure 38). Samples from the main body ortho-mesocumulates, as well as from the upper and the NE body have elevated concentrations of ZnO and TiO_2 and are also depleted in Ni where the Mg# varies between ca. 0.25-0.35. The enrichment in TiO_2 is observed in all of the groups and bodies including the main body adcumulates and the SW ortho-mesocumulates.

Figure 37. Mg# vs MnO and V_2O_3 plots of analysed Cr-spinels. The polygon drawn for magmatic Cr spinels is after Evans and Frost (1975) and Mekhonoshin et al. (2020).

Figure 38. Mg# vs ZnO, TiO_2 and NiO wt.% plots of analysed Cr-spinels. Trend according to Groves et al. (1977).

In the main body ortho-mesocumulates and in the main body adcumulates nickel content increases in chromites where the calculated Mg# is over 0.35 (Figure 38). In addition to those chromite grains, some samples taken from the NE and SW bodies are also Ni-rich. Low Ni-content is observed in all of the samples in which the Mg# varies between 0.25 and 0.35. When considering the V_2O_3 content plotted with Fe^{3+}#, two groups are formed. The other group displaying a weak correlation between both of the elements and the other one constant has a similar V_2O_3 while Fe^{3+}# varies.

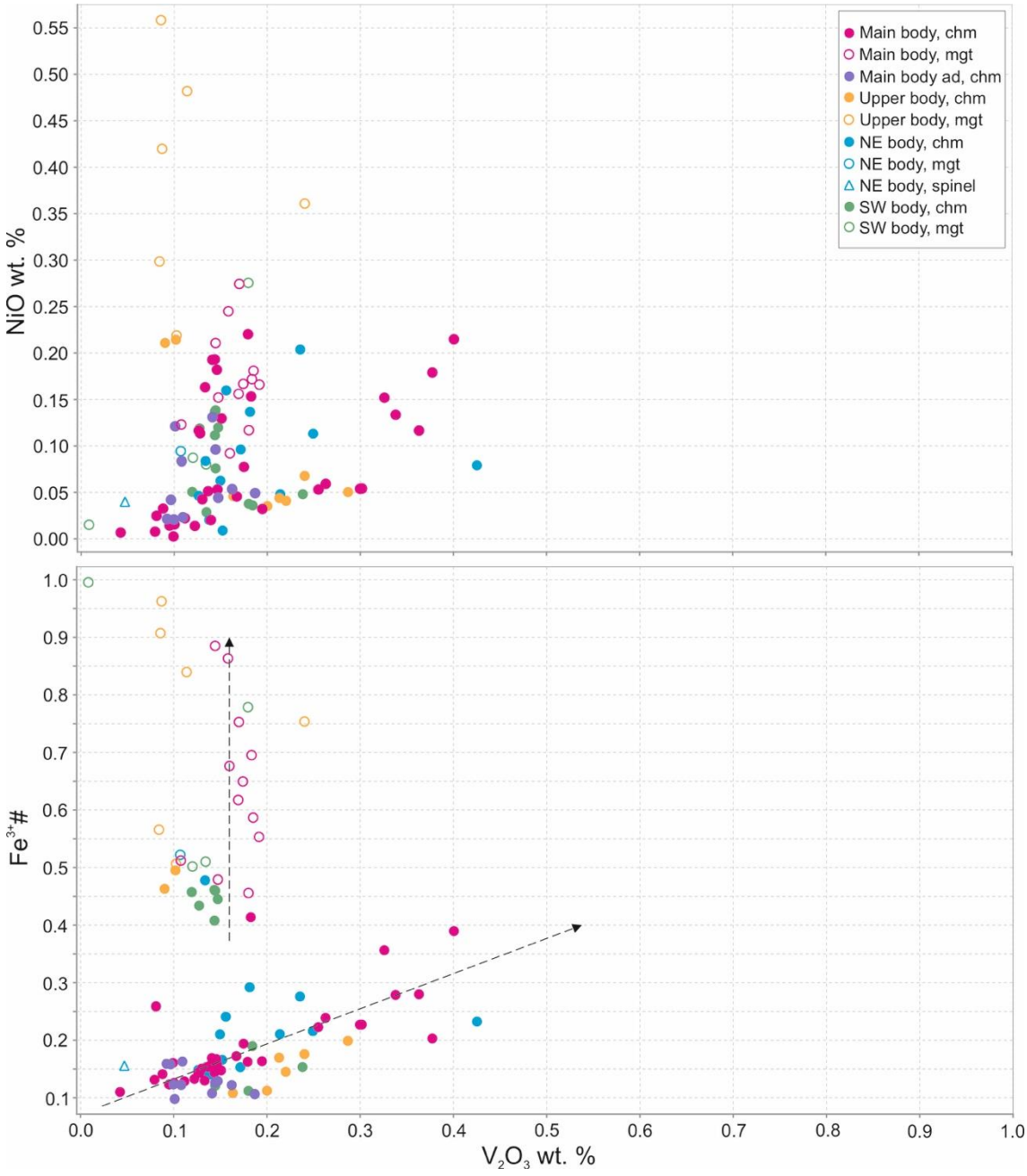

Figure 39. V_2O_3 wt.% vs Fe^{3+}# and NiO wt.% plots of the analysed Cr-spinels. Trends placed by naked eye.

Samples were taken from different depths from one of the Sakatti drill cores intersecting the main olivine cumulate body to study the variation in the chromite composition vertically across the body and with respect to the massive sulphide layers occurring inside the body (Figure 40). Three to four grains were analysed per thin section. The analysed grains occur in different positions in respect to the other minerals in the thin sections: 1) being enclosed by olivine or orthopyroxene, 2) on the grain boundary of olivine or 3) in the serpentine mesh. It can be observed that the nickel content of the analysed chromite grains is markedly lower in the samples which have been taken from the vicinity of the massive sulphide layers than in the samples taken further away from these units.

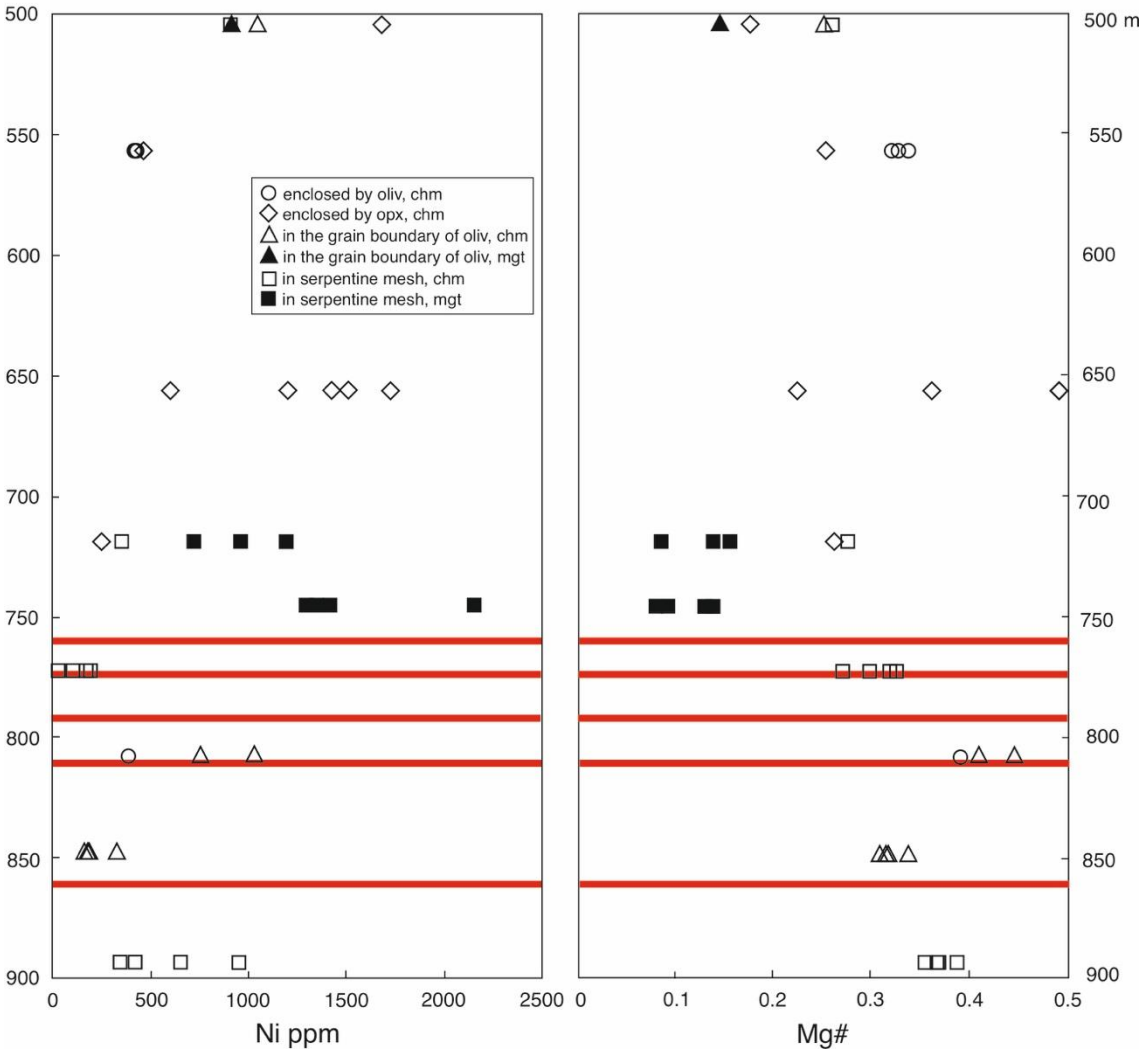

Figure 40. Chromite Ni content (ppm) and Mg# composition change by depth in the drill core 17MOS8168 from the Sakatti main olivine cumulate body. Red lines represent the massive sulphide layers. Abbrevations, oliv = olivine, opx= orthopyroxene, chm= chromite and mgt= magnetite.

Higher TiO_2 (<1.00 wt.%) values are observed in all of the bodies, in cases where the chromites are #Fe^{3+}-poor (0.11-0.28) and have V_2O_3 contents ranging between 0.14 and 0.37 (Figure 41).

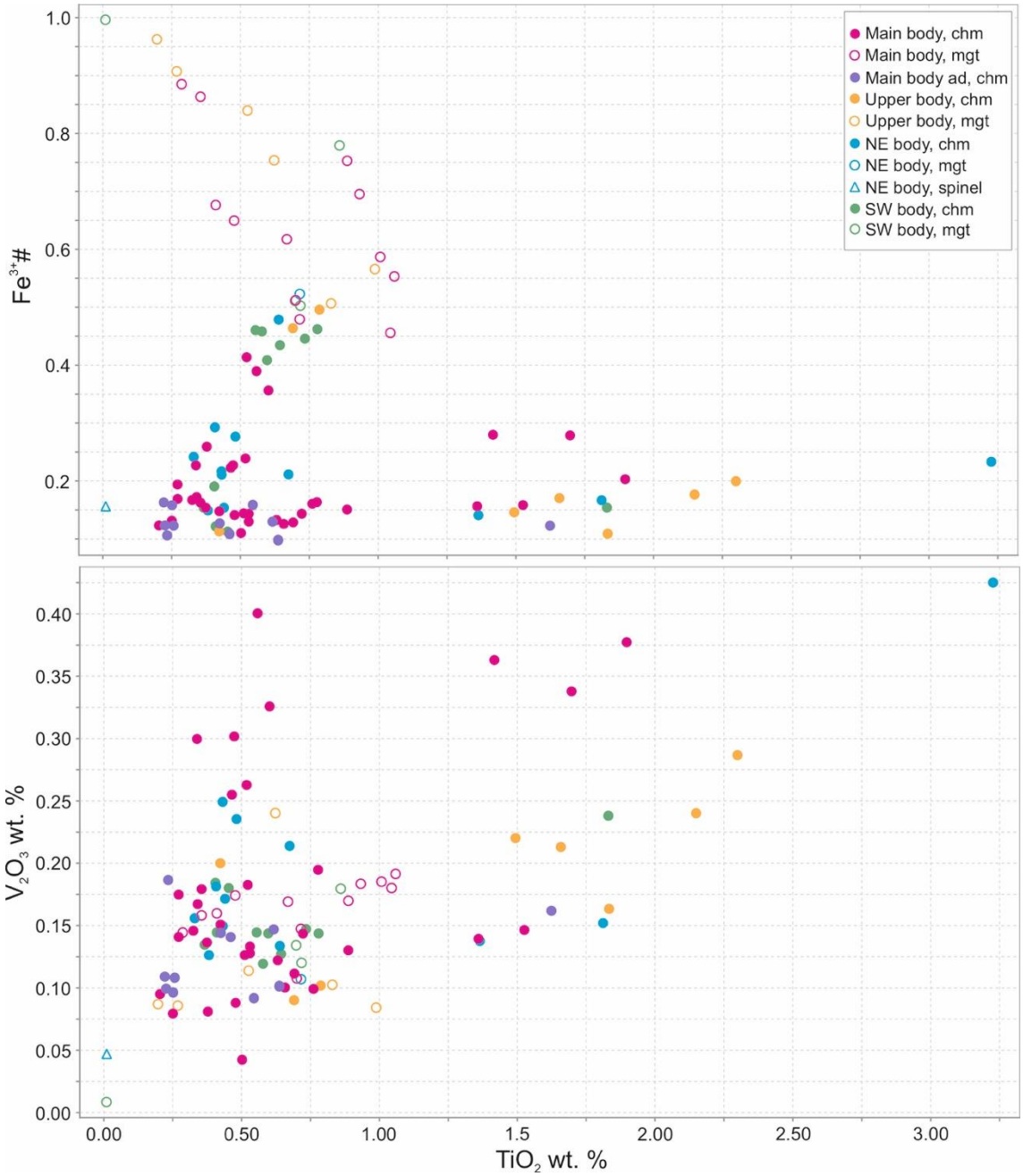

Figure 41. TiO_2 vs V_2O_3 and Fe^{3+}# plots of analysed Cr-spinels.

5.2.3. Trace element (Ru)

The ruthenium content of the chromite was measured using the LA-ICP-MS. In total, 32 grains were analysed from five thick section samples in three mineralised bodies (the main body, NE and SW body). The LA-ICP-MS results are presented in the Appendix 2. All of the Ru values plot under 1.5 ppb (Figure 42). 27 out of 32 analysis points plot between 0.05 and 0.77 ppb. The largest variation in Ru composition is observed in the NE body (0.15- 1.37 ppb). Ru values obtained from the SW cumulate body chromites are the lowest in comparison with the other Sakatti cumulates (0.05- 0.14 ppb). Samples TS05_SHS18, TS16_SHS18 and TS46_SHS18b represent peridotitic orthocumulate, TS27_SHS18b dunitic adcumulate and TS39_SHS18b peridotitic mesocumulate.

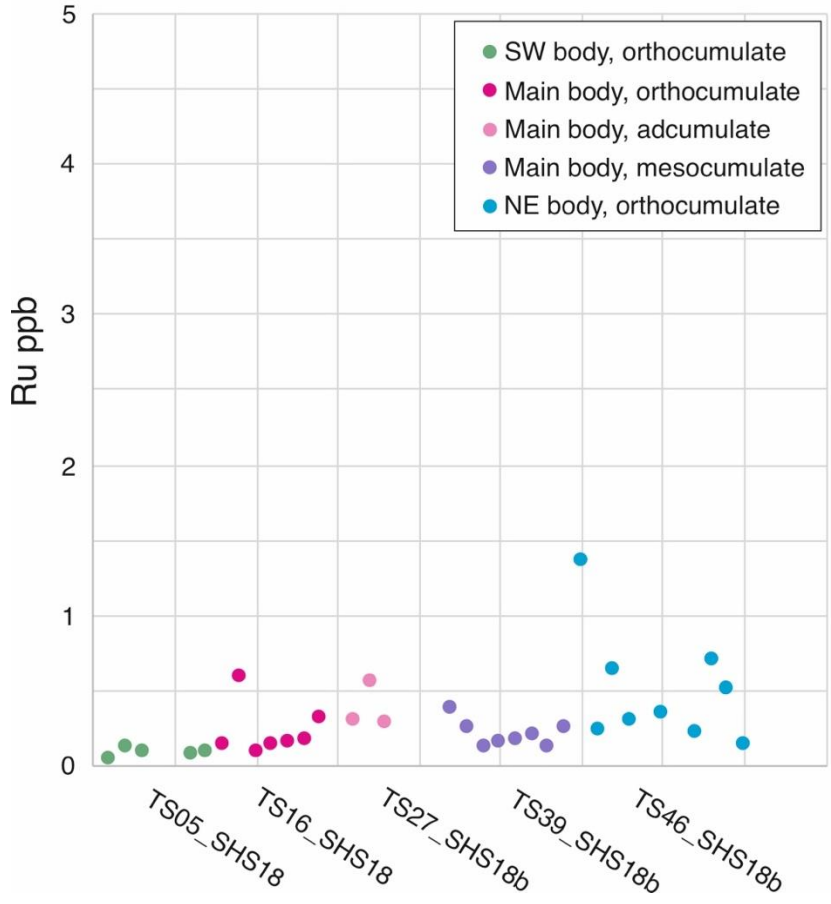

Figure 42. Ru pbb of analysed chromite grains from three mineralized bodies.

6. DISCUSSION

6.1. Magmatic affinity

All of the studied samples from the Sakatti peridotite bodies consist of cumulus olivine and chromite. Olivine occurs as unaltered grains and as olivine pseudomorphs within the main body and the NE body. Only serpentinised olivine is observed in the upper and SW bodies. Both pyroxene minerals occur in the intercumulus space in the main body and NE body. Disseminated sulphides are present in the main, NE and SW bodies. In addition to disseminated sulphides, massive sulphide layers occur in the main body (Figures 9, 10, 11 and 12). Bimodal olivines and hopper-like textured olivines are observed in the main body ortho-mesocumulates (Figure 18) and in the NE body (Figure 18). Hopper-like olivines are skeletal incomplete olivine crystals, which have been rapidly cooled and crystallised from the magma. Both of these textures (bimodal and hopper olivines) are products of supercooled turbulently flowing lavas, which only appear in komatiites (Arndt et al. 2008). A clear preferred orientation of olivine crystals is observed in the drill cores at the main cumulate body and the NE body. In addition to hopper and bimodal olivines, the clear preferred orientation of olivine grains could be an indicator of lava channel cumulate system (Naldrett 2004, Arndt et al. 2008).

Chromite grains occur in the Sakatti olivine cumulate rocks as: 1) enclosed by olivine and pyroxenes (ortho- and clinopyroxene), 2) on the grain boundaries of olivine or olivine pseudomorphs, and 3) in the alteration generated by serpentine mesh. Chromites, which occur as inclusions inside olivines, suggests that they were crystallised cotectically with the olivines (Barnes 1998). The melt inclusions in the NE body chromites indicate that the grains are primary and no alteration has occurred (Hanski et al. 2001). Petrographically, the Sakatti chromites can be divided into two groups: (1) chromites which have a thin magnetite rim, and (2) chromites which display compositional zoning throughout the whole mineral grain. Chromites with a thin magnetite rim are observed in the main olivine peridotite body ortho-mesocumulates and adcumulates and in the NE body, and they represent unaltered chromite grains. In contrast, the upper peridotite body and the SW body hosts zoned chromites also referred as ferritchromites. Zoned chromites are an effect of serpentinisation and metamorphism when Cr-magnetite starts to replace

the primary chromite (Barnes et al. 1996). In the low-temperature serpentinisation process, chromite grains become enriched in iron and due to the increase of Fe^{3+} in the mineral, chromites create magnetite veins along the grain boundaries and cracks (Barnes et al. 1996, Mekhonoshin et al. 2020).

The composition of chromite can be used as indicators of petrogenetic origin (Irvine 1965, Irvine 1967, Dick and Bullen 1984) and tectonic setting (Arai 1992, Barnes and Roeder 2001) indicator. According to Barnes (1998) and Evans (2017), magnesium number, Mg# [Mg/(Mg+Fe^{2+})], chromium number, Cr# [Cr/(Cr+Al)] and tribasic iron number, Fe^{3+}# [Fe^{3+}/(Cr+Al+Fe^{3+})] indicate the cooling history of chromites. The Mg# versus Cr# systematics of chromite is characteristic to different type of deposits (Figure 43). Chromite produced by fractional crystallisation in layered intrusions have a wide range of Mg# and a comparatively low range of Cr# (Dick and Bullen 1984). Cr# in the Sakatti chromites (0.56-0.79) is similar to layered intrusions (Irvine 1967), even though the Mg# varies between 0.18 and 0.56 in the Sakatti chromites. The chromites from the MtKeith komatiites (Barnes 1998) have high Cr#, between 0.61 and 0.81 and more variable Mg# between 0.12 and 0.7, compared to the Sakatti chromites. According to Barnes and Roeder (2001), komatiitic chromites usually have constant Cr# and Fe^{3+}# and more variable Fe^{2+}#. The Mg# ratio appears to be higher (0.5-0.55) in the Sakatti chromites that are enclosed by orthopyroxene in the adcumulates (Table 7). The zoned grains in the upper and SW bodies have higher Fe^{3+}# and lower Mg# than the non-zoned grains (Table 7). The chromites in the Sakatti main body chromites adcumulates have lower Cr# and higher Mg# (Figure 43), than the chromites in the main body ortho-mesocumulates. In addition to higher Mg#, the chromites in the main body ortho-mesocumulates have elevated Fe^{3+}# compared to the chromites in the main body adcumulates. During re-equilibration and cooling the chromites in adcumulates have only limited amount of trapped intercumulus liquid to interact with and thus are poorer in Fe^{3+}# (Barnes 1998). Most of the Sakatti chromites have variable Al# [Al/(Al+Cr+Fe^{3+})] and Cr# when Fe^{3+}# is constant (Figures 33 and 36). Some of the Sakatti chromites have decreasing Al# and Cr# when Fe^{3+}# increases, which is due to the reaction with trapped intercumulus liquid while cooling and crystallisation (Barnes and Kunilov 2000).

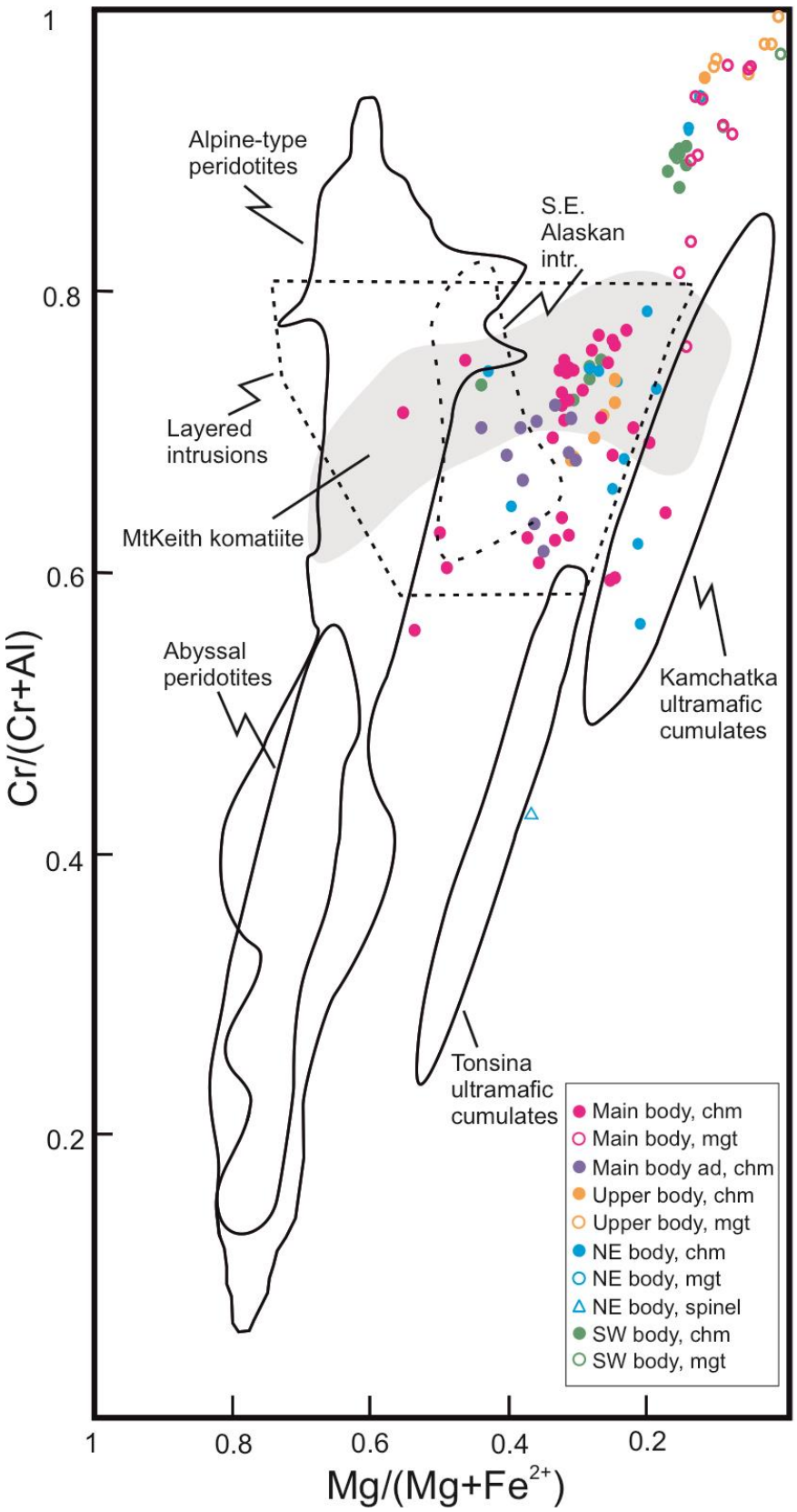

Figure 43. Compositional fields of the Sakatti chromites Mg# vs Cr#. Compositional fields of chromites from different types of deposits, Alpine-type and abyssal peridotites (Dick & Bullen 1984), layered intrusions and Alaskan type intrusions (Irvine 1967), Kamchatka ultramafic cumulates (Kepezhinskas 1993) and Tonsina ultramafic cumulates (DeBari & Coleman 1989) and MtKeith komatiites (Barnes 1998) are presented for comparison.

Table 7. Typical composition of the chromite grains from the different cumulate bodies. Complete EPMA-analyse list can be found from Appendix 1. Abbreviations, opx= orthopyroxene and chm= chromite.

Body	MAIN	MAIN (opx)	MAIN AD	UPPER	NE	SW
Sample	TS20_SHS18_a chm	TS16_SHS18_a chm	TS27_SHS18_c chm	TS16_MHP18_c chm	140778_b chm	TS01_MHP18_c chm
Weight % oxides						
SiO_2	0.05	0.10	0.02	0.01	0.09	0.02
TiO_2	0.34	0.27	0.42	1.66	0.38	1.83
V_2O_3	0.17	0.14	0.14	0.21	0.13	0.24
Al_2O_3	9.87	18.43	14.78	11.98	11.43	10.30
Cr_2O_3	48.93	41.75	47.48	43.88	47.48	46.54
FeO	21.21	15.20	18.57	22.34	22.66	22.73
Fe_2O_3	12.62	12.68	9.84	12.56	11.04	11.41
MnO	0.53	0.17	0.31	0.37	0.41	0.30
MgO	5.65	11.06	8.77	5.48	5.08	5.55
CaO	0.01	0.01	0.01	0.00	0.00	0.00
NiO	0.05	0.19	0.10	0.04	0.05	0.05
ZnO	0.68	0.09	0.10	0.82	0.18	0.34
Total	100.10	100.09	100.54	99.36	98.92	99.31
Cr	1.26	1.00	1.18	1.15	1.24	1.25
Ti	0.01	0.01	0.01	0.04	0.01	0.05
V	0.00	0.00	0.00	0.00	0.00	0.01
Al	0.38	0.66	0.55	0.47	0.45	0.41
Fe^{3+}	0.34	0.34	0.25	0.33	0.29	0.30
Fe^{2+}	0.71	0.50	0.59	0.73	0.75	0.73
Mn	0.01	0.00	0.01	0.01	0.01	0.01
Mg	0.27	0.50	0.41	0.27	0.25	0.28
Ni	0.00	0.00	0.00	0.00	0.00	0.00
Zn	0.02	0.00	0.00	0.02	0.00	0.01
Mg#	0.28	0.50	0.41	0.27	0.25	0.28
Cr#	0.77	0.60	0.68	0.71	0.74	0.75
Fe^{3+}#	0.17	0.17	0.13	0.17	0.15	0.15
Al#	0.21	0.33	0.28	0.24	0.23	0.21
Ni ppm	358	1514	759	345	363	377

In several studies researchers (Barnes 1998, Barnes and Tang 1999, Luolavirta et al. 2018, Mekhonoshin et al. 2020) have used the Al_2O_3 versus TiO_2 plot to reflect the parental magma composition (Figure 44). TiO_2 can retain some of the original composition of the original tectonic setting (Barnes et al. 1996). Typically, komatiites have a low TiO_2 content (less than 2 wt.%) (Barnes and Roeder 2001) and, picrite basalts (such as parental magma for the Kevitsa intrusion) have higher TiO_2 content and they are low in Al_2O_3 (Luolavirta et al. 2018). Chromites from komatiites in Zimbabve and Munro have low TiO_2 content (Arndt et al. 1977, Zhou and Kerrich 1992). On the Al_2O_3 wt.% vs TiO_2 wt.% plot (Figure 44), most of the chromites in Sakatti main body ortho-mesocumulates

and the chromites in the NE body plot within the komatiite field in contrast to the chromites of Kevitsa intrusion (Figure 44). According to Hanski and Kamenetsky (2013), Paleoproterotzoic chromites in the CLGB can be divided into Ti-rich and Ti-poor populations (Figure 44). Ti-rich chromites are associated with picritic parental magmas and Ti-poor chromites with komatiitic parental melts. Most of the Sakatti chromites are Ti-poor compared to the Kevitsa chromites (Luolavirta et al. 2018) and plot closer to the chromite compositions from the Zimbabwe and the Munro komatiites (Figure 44). A specific feature observed at Sakatti is that some of the main body chromites have notably high TiO_2 content (TS07_SHS18, 140604, TS33_SHS18). Increases in TiO_2 content are clear in those chromite samples, which contain rutile needles (Figure 18), in which case some grains contain up to 3.22 wt.% of TiO_2. Majority of these high-TiO_2 chromite grains occur in the samples taken from the main olivine cumulate body ortho-mesocumulates and one has also been found from the main body adcumulate rock sample. Lesher et al. (2019) suggests that the Ti-enricment can be an effect of dynamic raise of Fe/Ti oxide during the crystallisation of chromite, when the magma partially melts an iron-rich lithology (e.g. ferrogabbro). The Sakatti deposit hanging-wall stratigraphy contains a sequence of gabbroic sills. The sills intersect the mafic volcanic and scapolite-mica rocks, which form a part of the hanging-wall stratigraphy. However, the sills do not intersect the main cumulate body (Brownscombe et al. 2015). Therefore, the magmatic phase that formed the Sakatti main olivine cumulate body could have been contaminated by the gabbroic sills during its emplacement/deposition.

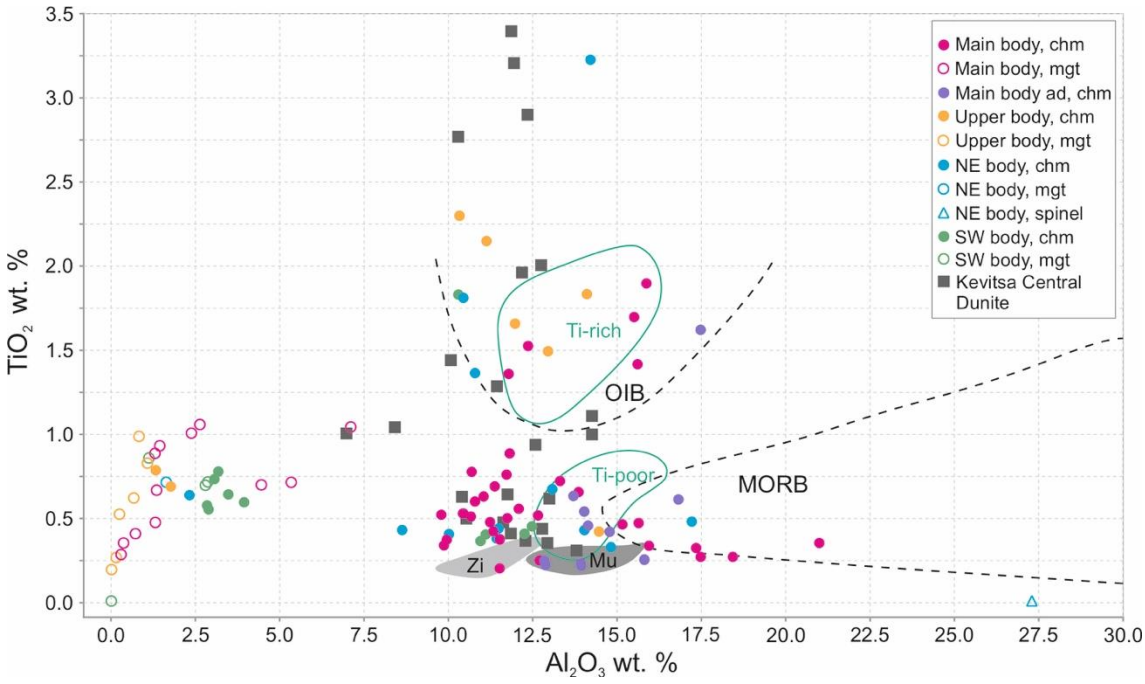

Figure 44. Al_2O_3 wt.% vs. TiO_2 wt. %. Fields for komatiites from Zimbabwe (Zi) and Munro, USA (Mu) after Zhou and Kerrich (1992) and Arndt et al. (1977), respectively. Fields for OIB and MORB after Kamenetsky et al. (2001). Dark grey squares present chromites from Kevitsa Central dunite after Luolavirta et al. 2018. Ti-poor and Ti-rich fields after Hanski and Kamenetsky (2013). Abbreviations OIB = oceanic island basalts and MORB = mid-ocean ridge basalts.

Three of the chromite analyses obtained from the samples taken from the Sakatti main cumulate body follow the Fe-Ti compositional trend (Figure 31). These chromite grains (thin sections: TS07_SHS18_b, TS16_SHS18_b and 140604_d) are enclosed by orthopyroxene or orthopyroxene pseudomorphs. According to Barnes and Roeder (2000) the Fe-Ti trend can be recognised in chromites that crystallises during fractional crystallisation of pyroxene (or olivine) from the parent magma. This results in the enrichment of titanium and in the rise of the Fe/Mg ratio of the melt. The composition of these three chromite samples from the main body orthocumulates suggests that chromites have reacted with the trapping intercumulus liquid.

Unaltered chromites display a negative correlation between MnO and Mg# (Evans and Frost 1975). In the Sakatti chromites, most of the grains have MnO content between 0.13 and 0.63 (Figure 37). Majority of the chromites plot within the polygon for magmatic Cr-spinel (Evans and Frost 1975, Mekhonoshin et al. 2020), while some of the grains from the main body ortho-mesocumultates have higher MnO content (0.66- 0.90). These grains

are enclosed by chloritised orthopyroxe or occur in the alteration generated by serpentine mesh. Therefore, it can be attributed that these grains are altered due to metamorphism (Barnes et al. 1996).

6.2. Ni content of chromite

Nickel content in the Sakatti deposit chromites is generally low (down to 1730 ppm), especially in the parts where massive sulphide layers occur (less than 500 ppm, Table 7). The Ni content of the chromites can be observed to follow the magmatic trend (liquidus control) in cases where the value of Mg# is <0.35 (Figure 45). During fractional crystallisation, the Mg# in the magma decreases, when olivine and other silicates crystallise from the magma and extract magnesium from the melt. The result of this is that the amount of iron increases in the residual magma, and thus more iron for chromite crystallisation is available (Barnes 1998). In the main body ortho-mesocumulate the chromites have relatively low nickel contents between 20 and 608 ppm, except the chromites enclosed by orthopyroxene (mostly 1430-1730 ppm Ni). The nickel content is controlled by the sulphide liquid, when the Mg# is less than <0.35 (Figure 45). The liquidus trend associated by fractional crystallisation of the silicate melt in the system can be observed in the chromite samples where Mg# is over 0.35. Majority of the chromites from the main body adcumulates are Ni-undepleted (Figure 45). The effect of Ni-depletion associated with the formation of a separate sulphide liquid phase can be observed in the composition of the chromites in drill core 17MOS8168 which intersects the whole Sakatti main olivine cumulate body and several massive sulphide rock units hosted by this ultramafic formation (Figure 40). The lowest chromite nickel contents in this drill core are measured from the cumulate rocks which are closely spatially associated with the massive sulphide units. Further away from the massive sulphides the Ni-content of the chromites can be observed to be higher. In addition, Mg# increases slightly in the same depth.

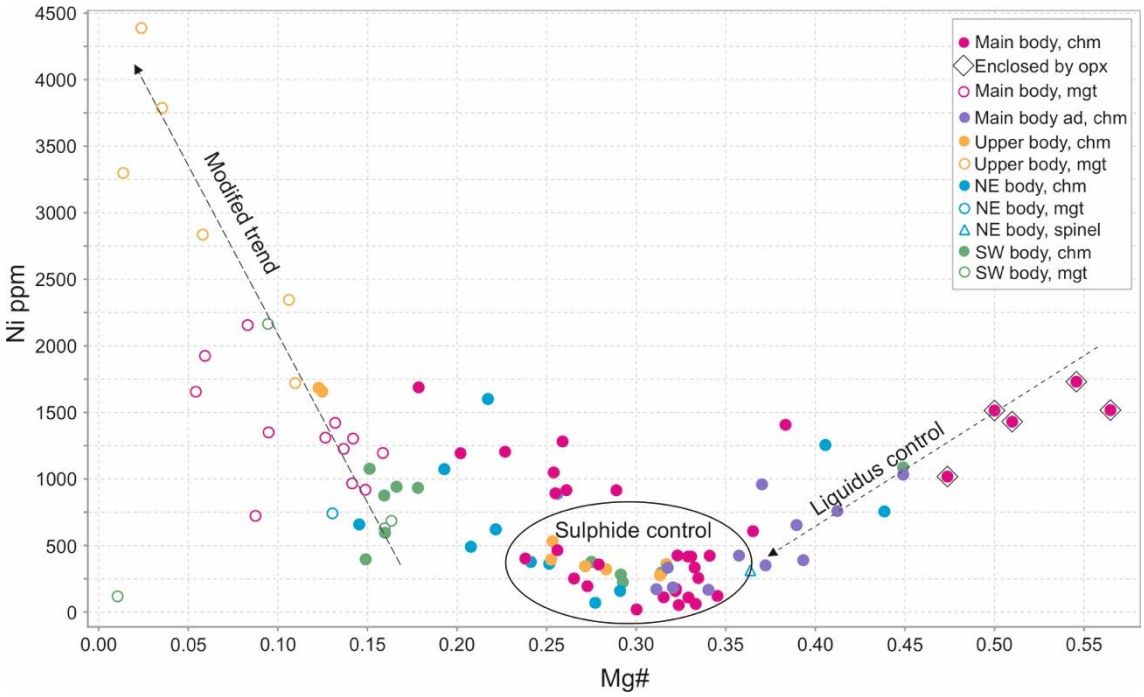

Figure 45. Mg# vs Ni ppm. Ni-depleted chromites occur inside the sulphide control circle. The high Mg# occurs in chromites that are enclosed by orthopyroxene (surrounded by rhombus). Modified trend and the liquidus control trend placed on naked eye.

In the upper and SW bodies, the nickel content of the chromite grains increases from the core towards the outer rims. This a natural outcome of alteration of the ultramafic cumulates when olivine is transformed to serpentine and magnetite starts to replace chromite (Barnes et al. 1996, Barnes 2000). In the Sakatti upper peridotite body, the nickel content of the chromites is proposed to be strongly controlled by serpentinisation and as a consequence the growth of magnetite, due to portioning of nickel from chromites to magnetite and sulphides (Barnes 2000). Similarly, in the majority of the SW cumulate body chromites nickel content is suggested to be controlled by the serpentinization process. The NE cumulate body chromite grains have wider scatter in their Ni-values, resembling the main peridotite body chromites.

According to Barnes and Kunilov (2000) lower chromite nickel contents (for given Fe^{3+}) are found from mineralised deposits, whereas in the sulphide barren formations chromites have more constant and higher nickel content. Barren formations display steep correlation with NiO and Fe^{3+}, when the mineralised deposits show a much widespread scatter and mostly lower Ni contents. Barnes and Kunilov (2000) suggest that this observation can be explained by two ways, 1) chromites with low nickel content have crystallised from Ni-depleted magma, due to the extraction of sulphide liquid or, 2) the chromites are

reduced in nickel while reacting and re-equilibrating with nickelferous magmatic sulphides during cooling and solidification. If the former alternative interpretation is assumed to be valid in the case of Sakatti chromites, also the cumulus olivines in the sampled rocks should be depleted in nickel. At the time of the writing of this thesis the composition of the cumulus olivine in the samples from which the chromite analyses were performed in the course of this study is still to be investigated. The latter suggested alternative interpretation cannot be true in the case of the Sakatti chromites, due to the fact that the studied grains do not occur in close contact or immerdiate vicinity of the sulphide mineral grains in the samples. Therefore, it could be assumed that the Ni-depletion of chromites in Sakatti can be attributed to magmatic extraction of a separate sulphide liquid phase producing Ni-depleted chromites. In contradiction to the proposed interpretation Browncombe et al. (2015) suggests that the sulphide liquid formation and fractioning occurred before the Sakatti main peridotite body cumulus silicates formed which is presented to be evidenced by the high concentrations of Ni in the main body cumulus olivines.

The Sakatti chromites display two separate trends when Fe^{3+}# versus NiO wt. % are plotted (Figure 46). The first trend is suggested to be present with sharply increasing NiO content, when the Fe^{3+}# is in the range of 0.1-0.2 and the second with a directly proportional positive correlation between the two variables. Compared to other deposits (Figure 46), the Sakatti chromites have similar NiO content with komatiites from MtKeith and Wiluna (Barnes 1998). With Fe^{3+}#, more similarities are observed with Jinchuan intrusion's Cr-spinels (Barnes and Tang 1999),

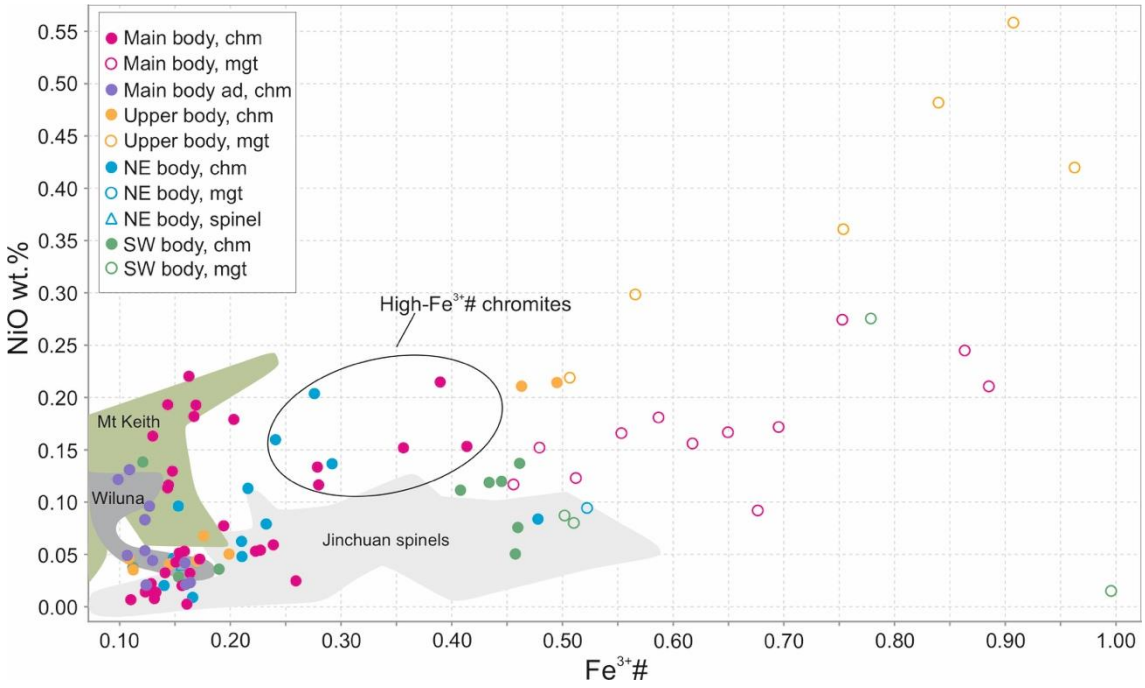

Figure 46. Fe^{3+}# vs NiO wt. % plot of analysed Cr-spinels. Light grey field represents the Cr-spinels from Jinchuan intrusion by Barnes and Tang (1999), darker grey field the Cr-spinels from Wiluna komatiites and green field Mt Keith komatiite Cr-spinels by Barnes (1998). Inside the circle high-Fe^{3+}# chromites after Barnes and Kunilov (2000).

6.3. Implications for exploration

Chromite is a common accessory mineral ultramafic and mafic rocks, and the study of the chromite composition can yield important information about the parental magma composition, oxygen fugacity and possible contamination source of the magma which formed these rocks (Evans 2017). Chromite can retain information about the chemical and physical conditions of the past geological environments as it is less susceptible to chemical alteration caused by metamorphism than most of the silicates and sulphides (Barnes and Roeder 2001, Evans 2017).

Generally, the high ZnO (0.5 > ZnO wt.%) content of chromite has been considered as an effect of mineralisation process (Groves et al. 1977, Lamberg and Peltonen 1991, Peltonen 1995b) or as a sign of metamorphic alteration (Barnes et al. 1996, Barnes 2000). It has been proposed that the driving factor behind the high Zn content observed in chromite is the contamination of the magma with Zn-rich country rocks (Lamberg 1991, Peltonen 1995b). According to Alapieti et al. (1990) and Lamberg and Peltonen (1991) high Zn content is due to a contamination of the ultramafic magma with sulphide bearing

country rocks. The occurrence of Zn-rich chromite has been suggested to indicate a favourable system for the assimilation of sulphide bearing sediments which has possibly experienced sulphide saturation during its evolution (Peltonen 1995b). The Sakatti chromites are enriched in ZnO (up to 1.11 wt.%), with the exception of the SW body (down to 0.34 wt.%). The chromite grains of the Sakatti main cumulate body in which the ZnO content exceeds 0.5 wt. % are spatially associated with the current known massive sulphide units (Figure 47, Table 7). The high Zn content is observed also in the upper body and the NE body chromites. Zinc content of the magma can remain high, although the sulphide saturation and fractionation have already taken place (Lamberg 1990), which could potentially explain the high Zn-content of the chromite found from the upper peridotite body (Figure 38).

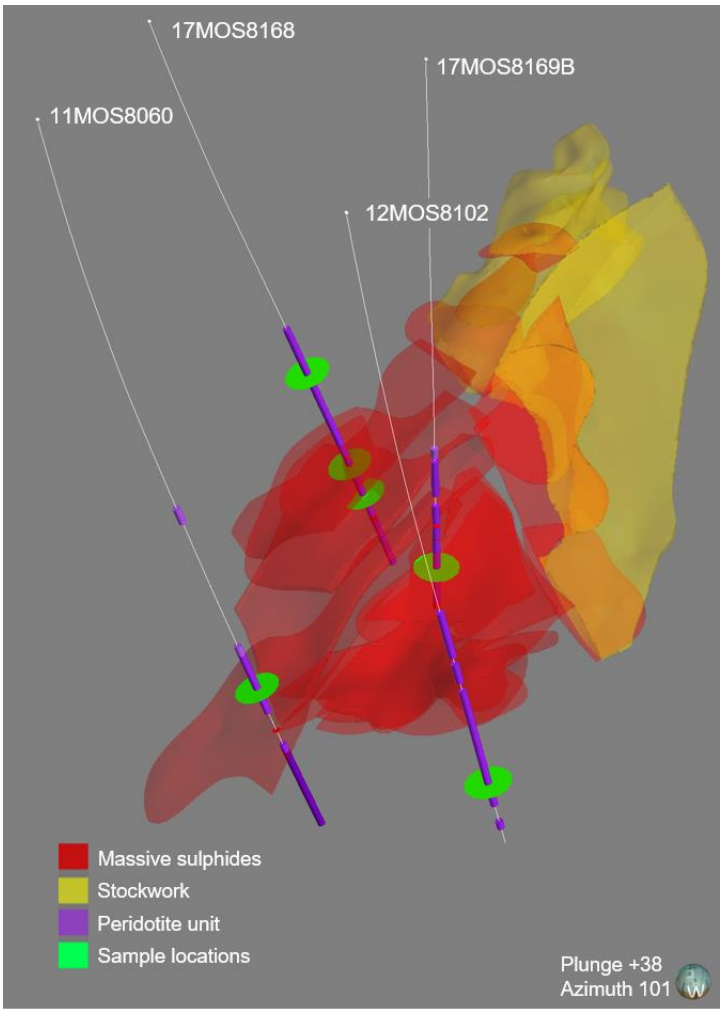

Figure 47. 3D model of the Sakatti Cu-Ni-PGE deposit main olivine peridotite body, where the high ZnO-content (<0.5 wt. %) is displayed. The purple thick drillhole traces represent peridotite, the red volumes represent massive sulphide lenses and the yellow volumes represents the stockwork zone. Green disks mark the locations of the samples with the high ZnO-content (<0.5 wt. %).

The Matarakoski formation hosts sulphide-bearing sedimentary rocks (Hanski and Huhma 2005). According to sulphur isotope data from the Sakatti sulphides, the Matarakoski sedimentary rocks could be the sulphur source for the deposit (Brownscombe et al. 2015). As mentioned, a sediment contamination in the magma would increase the ZnO content of the chromites (Peltonen 1995b). However, this requires some more studies to confirm that the Matarakoski sediments are high enough of ZnO to support this hypothesis. Another possible sulphur source in the Sakatti deposit is an evaporite rock, anhydrite, that occurs both as interlayers in the mica schist and as inclusion in the olivine ortho-mesocumulate (Halkoaho 2014). If the sulphur source for the Sakatti deposit was anhydrite, assimilation of sulphide-rich country rock should cause oxidation of the magma and crystallisation of high proportions of relatively Fe^{3+}-rich spinels (Barnes and Kunilov 2000). Barnes and Kunilov (2000) observed Fe^{3+}-rich spinels in Talnakh, where the Fe^{3+}# of the spinels varies between 0.27 and 0.82. In Talnakh, the Fe^{3+}# in the spinels represents a primary magmatic feature of the chromites. The Sakatti chromites (analysed from the core) have lower Fe^{3+} content than the Talnakh spinels, varying between 0.11 and 0.50 (Figure 46). Portion of the analysed Sakatti unzoned chromite grain cores have high Fe^{3+}# and this is suggested to represent a primary magmatic feature of the mineral. Thus, the high Fe^{3+}# of these chromites is proposed to indicate sulphide saturation in the system during the magmatic phase and act a marker of the processes which were involved in the formation of the Sakatti deposit.

V_2O_3 values in chromite reflect the oxidation state of the magma, when plotted against the Fe^{3+}# (Evans 2017). In the Harker plot (Figure 39), the upper groups' samples are oxidised, as the V_2O_3 stays close to constant (the group contains magnetites and chromites mainly from the upper and SW peridotite bodies) and the lower groups' samples are reduced, where both of the elements are high. Alteration process in the upper peridotite body and in the SW body chromite grains has been pervasive. Thus, the composition of these chromites do not present the primary features anymore, and the chromite compositions plot to the oxidised group (Figure 39).

New exploration method was recently introduced by Locmelis et al. (2013, 2018). The trace element ruthenium can be used as a tracer for magmatic sulphide deposits. However, the use of Ru as a tracer is still under development to fully understand the elements

behaviour in different kinds of magmatic systems. Ru partitions into sulphide phase in mineralised systems rather than into chromite. Thus, it could be assumed that the Ru content of the Sakatti chromites is extremely low (Figure 48). Compared to other deposits (Locmelis et al. 2013, 2018), the low Ru-content of the chromites clearly classifies Sakatti as a mineralised system (Figure 48). However, interpreparation of the LA-ICP-MS results is difficult, due to the lack of EPMA data from the exact same chromite grains. One contributing factor is likely to be the correction value (Cr-content of 208000 µg), which might be too high for the Sakatti chromites. More consistent correction values would be created with the EPMA data and by comparing those values, the interpreparation would be more even. Lastly, only 32 grains were measured. To get a proper perspective on how the Ru content varies in the Sakatti chromites, further studies on the subject would be needed.

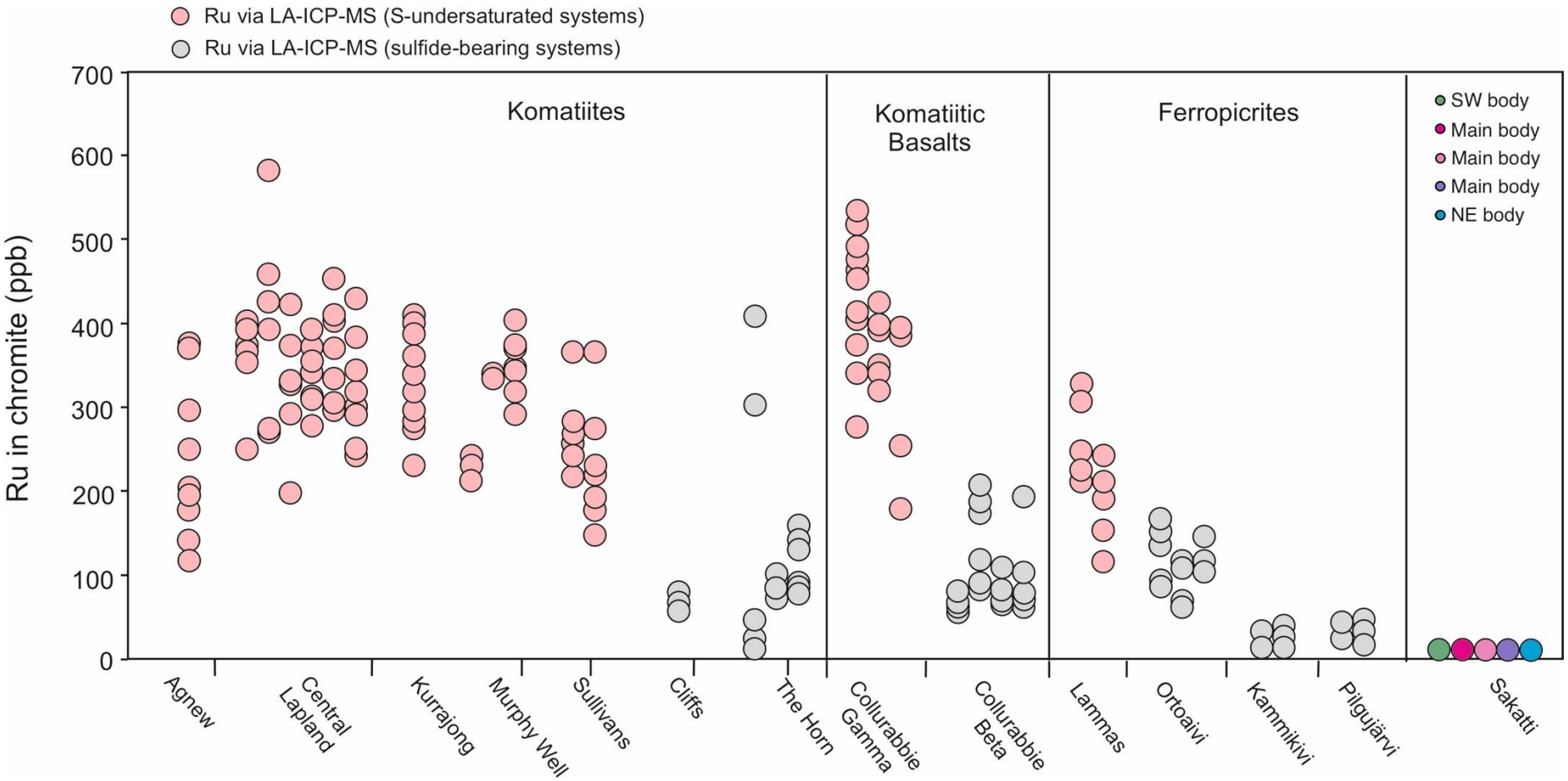

Figure 48. Ru contents in chromites. Ru content in the Sakatti chromite grains is presented by an average from each thick section. Detailed presentantion of the data is found from the figure 42. Data from komatiites, komatiitic basalts and ferropicrites from Locmelis et al. 2018. Unmineralised data marked on light pink and mineralised with gray. Modified from Locmelis et al. 2018.

7. CONCLUSIONS

The main results of this study are:

- The Sakatti chromites can be optically and chemically divided into two groups: 1) unzoned chromite grains from the main mineralised olivine peridotite body and the NE mineralised olivine cumulate body and 2) zoned chromite grains with several ferritchromite outer rims of the barren upper olivine cumulate body and the mineralised SW olivine cumulate body.
- The composition of the Sakatti chromites display similarities to both chromites from komatiites and from layered intrusion with their calculated Mg# and Cr# values and and thus they can not be unequivocally chemically categorised by looking only to these compositional variables. Including the Al_2O_3 and TiO_2 composition and textural features (olivine grain appearance and orientation), the Sakatti chromites resemble more chromites which saturate from komatiitic magmas than chromites which are associated with picritic or basaltic melts. Compared to the chromites from the Kevitsa intrusion, the majority of the analysed Sakatti olivine cumulate rock chromites are Ti-poor. Enrichment of Ti was observed in the clear minority of the Sakatti chromite analyses in which case the mineral's titanium content was found to be at similar levels with the Ti-rich chromites reported from the Kevitsa intrusion.
- A subset from those Sakatti chromites which are spatially associated with massive sulphide rock units were found to be enriched in ZnO and TiO_2. The source behind the elevated Zn-levels could indicate assimilation of sulphide bearing sediments to the magma. However, this requires some more studies for confirmation. The Ti enrichment could be explained by the magma being contaminated by iron-rich gabbro during its evolutional history.
- The nickel content of the chromite in the studied Sakatti olivine cumulate rocks is generally low and the majority of the analysed chromite grains can be considered as Ni-depleted. The proposed cause for this feature in the chromite chemistry is the separation of a sulphide liquid phase during the magmatic evolution of the Sakatti geological environment which contributed directly to the formation of the

orthomagmatic sulphide deposit in conjunction with the development of the olivine cumulate rock bodies.

- Portion of the Sakatti primary magmatic chromites is enriched in tribasic iron (Fe^{3+}) which could be interpreted to reflect their crystallisation from a melt which has potentially assimilated sulphur-rich evaporitic rocks in the course of the magmatic evolution. This remains hypothesis and would require more detailed studies for verification.
- The content of the trace element ruthenium was determined to be less than 5 ppb in the Sakatti cumulate rock chromites. Ru levels of the chromite can be used as a petrogenetic indicator in separating between mineralised and barren magmatic formations. Therefore, the low ruthenium values of the of the Sakatti chromite are an indication of a mineralised geological environment.
- The high Zn, high Ti, low Ni and high Fe^{3+} compositions represent pure magmatic features in the Sakatti olivine cumulate hosted chromites. These elemental compositions of the chromite are a tracer for the exploration potential of the Sakatti deposit rocks and these features could be tested for also elsewhere in the Central Lapland Greenstone Belt.

8. ACKNOWLEDGEMENTS

Firstly, I would like to thank AA Sakatti Mining Oy for providing me the background material and samples for the study. I highly appreciate the opportunity to work with the thesis subject and to be part of the Sakatti project. Especially I want to thank my co-supervisor Tuomas Väliheikki. My first summer in Lapland 2018 could not have been better as I learned the basics of being a geologist. I want to thank my supervisor, the professor of practice, Petri Peltonen for guidance and ideas for the thesis study.

Furthermore, I would also like to give my gratitude to Radek Michallik for the sample preparation and EPMA analysis and Christoph Beier for the LA-ICP-MS analysis. Lasse Pakkanen is thanked for the help with the EPMA analysis in the GTK mineral laboratory.

Finally, I want to thank my fellow students, with whom I spent hours and hours in the computer room working with various projects during the years. I also appreciate the support and solidarity of my family and friends during the writing.

9. REFERENCES

Ahvenjärvi, O. 2015. Sulfide and platinum group mineralogy of massive sulphide ore in the Sakatti Cu-Ni-PGE deposit. Master's thesis, University of Oulu, Department of Geosciences, Division of Geology and Mineralogy, 74 pp.

Alapieti, T. T., Kujanpää, J., Lahtinen, J. J. and Papunen, H. 1989. The Kemi stratiform chromitite deposit, northern Finland. Economic Geology and the Bulletin of the Society of Economic Geologists 84, 1057-1077 pp.

Anglo American plc. 2016. Ore Reserves and Mineral Resources Report 2016. 54 pp.

Anglo American plc. 2019. Ore Reserves and Mineral Resources Report 2019. 54 pp.

Anglo American plc. 2013. Anglo American group exploration. Webpages visited 06.05.2020. http://www.ama.org.uk/wp-content/uploads/2013/09/Group-Exploration Overview_Association-of-Mining-AnalystsFINAL.pdf

Arai, S. 1992. Chemistry of chromian spinel in volcanic rocks as a potential guide to magma chemistry. Mineralogical Magazine 56, 173-184.

Arndt, N. T., Naldrett, A. J. and Pyke, D. R. 1977. Komatiitic and iron-rich tholeiitic lavas of Munro Township, northeast Ontario. Journal of Petrology 18, 319-369.

Arndt, N. T., Barnes, S. J. and Lesher, C. M. 2008. Komatiite. Cambridge: Cambridge University Press, New York, 466 pp.

Barnes, S-J. and Often, M. 1990. Ti-rich komatiites from northern Norway. Contributions Mineralogy and Petrology 105, 42-54.

Barnes, S.-J. and Lightfoot, P. 2005. Formation of magmatic nickel sulfide ore deposits and processes affecting their copper and platinum group element contents. In: Hedenquist, J.W., Thompson, J. F. H., Goldfarb, R. J. and Richard J. P. (Eds.) Economic Geology: One Hundreth Anniversary Volume, Society of Economic Geologists Inc., Littleton, Colorado, 179-214.

Barnes, S. J., Halkoaho, T., Papunen, H. and Perring, C. 1996. Chromite in Komatiites: a comparative study of chromite in komatiites from the Forrestania Greenstone Belt, Western Australia and the Pulju and Kuhmo Greenstone Belts, Finland. CSIRO Australia Division of exploration and Mining, Exploration and Mining Report 273R, 70 pp.

Barnes, S. J. 1998. Chromite in komatiites, 1. magmatic controls on crystallization and composition. Journal of Petrology 39, 1689-1720.

Barnes, S. J., and Tang, Z., 1999. Chrome spinels from the Jinchuan Ni-Cu sulfide deposit, Gansu province, People's Republic of China. Economic Geology 94, 343-356.

Barnes, S. J. and Kunilov, V. Y. 2000. Spinels and Mg ilmenites from the Noril'sk 1 and Talnakh intrusions and other mafic rocks of the Siberian flood basalt province. Economic Geology 95, 1708-1717.

Barnes, S. J. and Roeder, P. L. 2001. The range of spinel compositions in terrestrial mafic and ultramafic rocks. Journal of Petrology 42, 2279-2302.

Barnes S. J. 2006. Komatiite-hosted nickel sulfide deposits: geology, geochemistry, and genesis. In: Barnes, S. J. (Ed.) Nickel deposits of the Yilgarn craton: geology, geochemistry, and geophysics applied to exploration, Special Publications 13, Society of Economic Geologists Inc., Littleton, Colorado, 51-118.

Barnes, S. J., Cruden, A. R., Arndt, N. and Saumur, B. M. 2016. The mineral system approach applied to magmatic Ni-Cu-PGE sulphide deposits. Ore Geology Reviews 76, 296-316.

Bedrock of Finland – DigiKP. Digital map database, Geological Survey of Finland. Webpages visited 10.09.2020. http://gtkdata.gtk.fi/Kalliopera/index.html

Bliss, N. W. and MacLean, W. H., 1975. The paragenesis of zoned chromite from central Manitoba. Geochimica et Cosmochimica Acta 39, 973-990.

Brownscombe, W., Ihlenfeld, C., Coppard, J., Hartshorne, C., Klatt, S., Siikaluoma, J. K. and Herrington, R. J. 2015. The Sakatti Cu-Ni-PGE sulfide deposit in Northern Finland. In: Maier, W., Lahtinen, R. and O'Brien, H. (Eds.) Mineral deposits of Finland, Elsevier, Amsterdam, Netherlands, 211-252.

Deer, W. A., Howie, R. A., Zussman, J. 1992. Spinel group: spinel series, magnetite series,

chromite series. In: Deer, W. A., Howie, R. A., Zussman, J. (Eds.) An Introduction to the rock-forming minerals. Longman Scientific & Technical, Harlow, Essex, England, 558-568.

DeBari, S. M. and Coleman, R. G. 1989. Examination of the deep levels of an island arc: evidence from the Tonsina ultramafic-mafic assemblage, Tonsina, Alaska. Journal of Geophysical Research 94, 4373-4391.

Dick, H. J. B. and Bullen, T. 1984. Chromian spinel as a petrogenetic indicator in abyssal and alpine-type peridotites and spatially associated lavas. Contributions to Mineralogy and Petrology 86, 54-76.

Dupuis, C., Beaudoin, G. 2011. Discriminant diagrams for iron oxide trace element fingerprinting of mineral deposit types. Mineralium Deposita 46, 319-335.

Eggins, S.M. 2003. Laser Ablation ICP-MS analysis of geological materials prepared as lithium borate glasses. The Journal of Geostandards and Geoanalytical research 27, 147-162.

Evans, B. W. and Frost, B. R 1975. Chrome-spinel in progressive metamorphism – a premilinary analysis. Geochemica et Cosmochimica Acta 39, 959-972.

Evans, D. 2017. Chromite compositions in nickel sulphide mineralized intrusions of the Kabanga-Musongati-Kapalagu Alignment, East Africa: Petrologic and exploration significance. Ore Geology Reviews 90, 307-321.

Fröhlich, F. 2017. Sulphide vein mineralization of the shallow eastern stockwork zone and its genetic relation to the massive sulphide mineralization at the Sakatti Cu-Ni-PGE deposit, Finland. Master's thesis, TU Bergademie Freiberg, Department of Mineralogy, Division Economic Geology, 167 pp.

Groves, D. I., Barrett, F. M., Binns, R. A. and McQueen, K. G. 1977. Spinel phases associated with metamorphosed volcanic-type iron-nickel sulfide ores from Western Australia. Economic Geology 72, 1224-1244.

Halkoaho, T. 2014. Petrology of Sakatti Ni-Cu-PGE deposit, Sodankylä, Finland version 1. Anglo American Internal Report.

Halkoaho, T. 2015. Petrology of Sakatti Ni-Cu-PGE deposit, Sodankylä, Finland part 2 thin section descriptions. Anglo American Internal Report.

Hanski, E., Huhma, H., Rastas, P. and Kamenetsky, V. S. 2001. The palaeoproterozoic komatiite-picrite association of Finnish Lapland. Journal of Petrology 42, 855-876.

Hanski, E. and Huhma, H. 2005. Central Lapland greenstone belt. In: Lehtinen, M., Nurmi, P.A., Rämö, O.T. (Eds.), Precambrian geology of Finland- Key to the evolution of the Fennoscandian shield, Elsevier B. V., Amsterdam, 141-194.

Hanski, E. and Kamenetsky, V. S. 2013. Chrome spinel-hosted melt inclusions in Paleoproterozoic primitive volcanic rocks, Northern Finland: Evidence for coexistence and mixing of komatiitic and picritic magmas. Chemical geology 343, 25-37.

Heikura, P., Törmänen, T., Iljina, M., Salmirinne, H. 2010. Mineral exploration report of relinquished claims Tulppionkariste 1-5 (mining reg. id. 8246/1-5) in Savukoski, northern Finland. Geological Survey of Finland, archive report M06/4723/2009/68, 50 pp.

Hölttä, P., Väisänen, M., Väänänen, J. and Manninen, T. 2007. Paleoproterozoic metamorphism and deformation in central Lapland, Finland. Geological Survey of Finland 44, 7-56.

Inkinen, O., Ilvonen, E., Pelkonen, R., 1984. Report of investigations of the Pulju schist belt and Hotinvaara area in 1982–1984. Outokumpu Oy, Lapin Malmi Exploration, archieve report 001/2742/OI, EI, RP/84/21, 54 pp.

Irvine, T. N. 1965. Chromian spinel as a petrogenetic indicator, part 1. Theory. Canadian Journal of Earth Sciences 2, 648-672.

Irvine, T.N. 1967. Chromian spinel as a petrogenetic indicator 2. Petrologic applications. Canadian Journal of Earth Sciences 4, 667-715.

Kamenetsky, V. S., Crawford, A. J. and Meffre, S. 2001. Factors controlling chemistry of magmatic spinel: an empirical study of associated olivine, cr-spinel and melt inclusions from primitive rocks. Journal of Petrology 42, 655-671.

Kepezhinskas, P.K., Taylor, R.N. and Tanaka, H. 1993. Geochemistry of plutonic spinels from the North Kamchatka Arc: comparison with spinels from other tectonic settings. Mineralogical Magazine 57, 575-589.

Keyas, R.R. and Lightfoot, P.C. 2009. Crustal sulfur is required to form magmatic Ni-Cu sulfide deposits: evidence from chalcophile element signatures of Siberian and Deccan Trap basalts. Mineralium Deposita 45, 241-257.

Koistinen, E., Heikura, P., 2010. Mineral resource assessment and 3D modelling of the Lomalampi deposit, Sodankylä Finland. Geological Survey of Finland, archive report M19/3732/2010/50.

Konnunaho, J. 2016. Komatiite-hosted Ni-Cu-PGE deposits in Finland: their characterization, PGE content, and petrogenesis. Geological Survey of Finland, Special Publication 92, 38 pp. (PhD Thesis).

Konnunaho, J., Halkoaho, T., Hanski, E. and Törmänen, T. 2015. Komatiite-hosted Ni-Cu-PGE deposits in Finland. In: Maier, W., Lahtinen, R. and O'Brien, H. (Eds.) Mineral deposits of Finland, Elsevier, Amsterdam, Netherlands, 93-131.

Lahtinen, J. 1996. Nickel mineral resource estimate of the Ruossakero nickel deposit, Enontekiö, northwestern Finland. Lapin Malmi Oy, archive report 035/1834/JJL/96. 21 pp.

Lamberg, P. and Peltonen, P. 1991. Chromian spinels in barren and fertile (Ni-Cu) Svecofennian 1.9 Ga ultramafic intrusions. Terra Abstracts 3(1), 111 p.

Lamberg, P. 1991. The use of chromian spinel as a toll in nickel exploration – a test with the samples from Hälvälä nickel mine. Geoanalytical Laboratory of Outokumpu Mining Services report 073, 23 pp.

Lehtonen, M., Airo, M-L., Eilu, P., Hanski, E., Kortelainen, V., Lanne, E., Manninen, T., Rastas, P., Räsänen, J. and Virransalo, P. 1998. Kittilän vihreäkivialueen geologia -The stratigraphy, petrology and geochemistry of the Kittilä greenstone area, northern Finland. Geological Survey of Finland, Report of Investigation, 140 pp.

Lesher, C.M., Carson, H. J. E. and Houle, M. G. 2019. Genesis of chromite deposits by dynamic upgrading of Fe ± Ti oxide xenocrysts. The Geological Society of America 47, 207-210.

Liipo, J. P., Vuollo, J. I., Nykänen, V. M. and Piirainen, T. A. 1995. Zoned Zn-rich chromite from the Näätäniemi serpentinite massif, Kuhmo greenstone belt, Finland. The Canadian Mineralogist 33, 537-545.

Liu, Y. S., Hu, Z. C. and Li, M. 2013. Applications of LA-ICP-MS in the elemental analyses of geological samples. Chinese Science Bulletin 58, 3863-3878.

Locmelis, M., Fiorentini, M., Barnes, S. and Pearson, N. 2013. Ruthenium variation in chromite from komatiites and komatiitic basalts – a potential mineralogical indicator for nickel sulfide mineralization. Society of Economic Geologists 108, 355-364.

Locmelis, M., Fiorentini, M., Barnes, S., Hanski, E. and Kobussen, A. 2018. Ruthenium in chromite as indicator for magmatic sulphide equilibration in mafic-ultramafic systems. Ore Geology Reviews 97, 152-170.

Luolavirta, K., Hanski, E., Maier, W. and Santaguida, F. 2018. Characterization and origin of dunitic rocks in the Ni-Cu-(PGE) sulphide ore-bearing Kevitsa intrusion, northern Finland: whole-rock and mineral chemical constraints. Bulletin of the Geological Society of Finland 90, 5-32.

Luukas, J., Kousa, J., Nironen, M. and Vuollo, J. 2017. Major stratigraphic units in the bedrock of Finland, and an approach to tectonostratigraphic division. Geological Survey of Finland, Special Paper 60, 9-40.

Makkonen, H., Halkoaho, T., Konnunaho, J., Rasilainen, K., Kontinen, A. and Eilu, P. 2017. Ni-(Cu-PGE) deposits in Finland – Geology and exploration potential. Ore geology Reviews 90, 667-696.

Mekhonoshin, A. S., Kolotilina, T. B., Doroshkov, A.A. and Pikiner, E.E. 2020. Compositional variations of Cr-spinel in high-Mg intrusions of the Primorsky ridge (Western Baikal, Russia). Minerals 10, 608.

Mitra, S. and Samanta, A. K. 1996. Rutile exsolution in Fe^{3+} chromites: a case study from layered granulitic complex of Sittampundi, S. India. Journal Geological Society of India 47, 75-82.

Moilanen, M., Hanski, E., Konnunaho, J., Yang, S.-H., Törmänen, T., Li, C. and Zhou, L. M. 2019. Re-Os isotope geochemistry of komatiite-hosted Ni-Cu-PGE deposita in Finland. Ore Geology Reviews 105, 102-122.

Moilanen, M., Hanski, E., Konnunaho, J., Törmänen, T., Yang, S.-H., Lahaye, Y., O'Brien, H. and Illikainen, J. 2020. Composition of iron oxides in Archean and Paleoproterozoic mafic-ultramafic hosted Ni-Cu-PGE deposits in northern Fennoscandia: application to mineral exploration. Mineralium Deposita 55, 1515-1534.

Murck, B. W and Campbell, I. H. 1986. The effects of temperature, oxygen fugacity and melt composition on the behavior of chromium in basic and ultrabasic melts. Geochimica et Cosmochimica Acta 50, 1871-1887.

Mutanen, T. 1997. Geology and ore petrology of the Akanvaara and Koitelainen mafic layered intrusions and the Keivitsa-Satovaara layered complex, northern Finland. Bulletin of Geological Survey of Finland, Bulletin 395, 233 pp.

Mutanen, T., Huhma, H. 2001. U-Pb geochronology of the Koitelainen, Akanvaara and Kevitsa layered intrusions and related rocks. In: Vaasjoki, M. (Ed.) Radiometric age determinations from Finnish Lapland and their bearing on the timing Precambrian volcano-sedimentary sequences. Geological Survey of Finland, Special Paper 33, 229-246.

Naldrett, A.J. 1999. World-class Ni-Cu-PGE deposits: key factors in their genesis, Mineralium Deposita 34, 227-240.

Naldrett, A.J. 2004. Magmatic Sulfide Deposits: Geology, Geochemistry and Exploration. Springer, Berlin, 728 pp.

Naldrett, A. J. 2010. Secular variation of magmatic sulphide deposits and their source magmas. Economic Geology 105, 669-688.

Niiranen, T., Lahti, I. and Nykänen, V. 2015. The orogenic gold potential of the Central Lapland greenstone belt, northern Fennoscandian shield. In: Maier, W., Lahtinen, R. and O'Brien, H. (Eds.) Mineral deposits of Finland, Elsevier, Amsterdam, Netherlands, 733-752.

Peltonen, P. 1995a. Petrology, geochemistry and mineralogy of ultramafic rocks and associated Ni-Cu deposits in the Vammala belt, southwestern Finland. Geological Survey of Finland, Espoo, 108 pp. (PhD thesis).

Peltonen, P. 1995b. Magma – country rock interaction and the genesis of Ni-Cu deposits in the Vammala Nickel Belt, SW Finland. Mineralogy and Petrology 52, 1-24.

Ripley, J. 2013. Ore deposit geology. Cambridge University Press, Colorado State University, 398 pp.

Robbins, M., Wertheim, G. K., Sherwood, R. C. and Buchanan, D. N. E. 1971. Magnetic properties and site distributions in the system $FeCr_2O_4$–Fe_3O_4 ($Fe^{2+}Cr_{2-x}$ $Fe^{3+}O_4$). Journal of Physics and Chemistry of Solids 32, 717-729.

Räsänen, J. and Huhma, H. 2001. U-Pb datings in the Sodankylä schist area, central Finnish Lapland. Geological survey of Finland Special paper 33, 153-188.

Santaguida, F., Luolavirta, K., Lappalainen, M., Ylinen, J., Voipio, T. and Jones, S. 2015. The Kevitsa Ni-Cu-PGE deposit in the Central Lapland Greenstone Belt in Finland. In: Maier, W., Lahtinen, R. and O'Brien, H. (Eds.) Mineral deposits of Finland, Elsevier, Amsterdam, Netherlands, 195-210.

Sheng-Hong, Y., Maier, W. D., Hanski, E. J., Lappalainen, M., Santaguida, F. and Määttä, S. 2013. Origin of ultra-nickelferous olivine in the Kevitsa Ni-Cu-PGE-mineralized intrusion, northern Finland. Contributions to Mineralogy and Petrology 166, 81-95.

TUKES, Finnish safety and chemicals agency. 2020. Mining register map service. Webpage visited 06.05.2020 http://gtkdata.gtk.fi/kaivosrekisteri/

Törmänen, T., Konnunaho, J., Hanski, E., Moilanen, M., Heikura, P. A., 2016. Palaeoproterozoic komatiite-related PGE mineralization at Lomalampi, central Lapland greenstone belt, northern Finland. Mineralium Deposita 51, 411-430.

Vuollo, J. 1986. Värriöjoen ultraemäksisen intruusion petrografia, mineralogia ja geokemia. Master's Thesis, University of Oulu, 108 pp.

Wager, L. R., Brown, G. M. and Wadsworth, W. J. 1960. Types of igneous cumulates. Journal of Petrology 1, 73-85.

Wang, C. Y., Zhou, M. & Zhao, D., 2005. Mineral chemistry of chromite from the Permian Jinbaoshan Pt-Pd- sulphide-bearing ultramafic intrusion in SW China with petrogenetic implications. Lithos 83, 47-66.

Zhou, M. and Kerrich, R. 1992. Morphology and composition of chromite in komatiites from the Belingwe Greenstone Belt, Zimbabve. The Canadian Mineralogist 30, 303-317.

APPENDIX 1.

Table 6. The EPMA data from the main body samples. See how the data was reprocessed from the chapter 4.2.2.

Body	MAIN	MAIN	MAIN	MAIN	MAIN	MAIN	MAIN	MAIN	MAIN	MAIN	MAIN	MAIN	MAIN	MAIN	MAIN	MAIN	MAIN	MAIN	MAIN
Sample	TS07_ SHS18 _a mgt	TS07_ SHS18 _b chm	TS07_ SHS18 _c chm	TS07_ SHS18 _d chm	TS10_ SHS18 _a chm	TS10_ SHS18 _b chm	TS10_ SHS18 _c chm	TS10_ SHS18 _d chm	TS16_ SHS18 _a chm	TS16_ SHS18 _b chm	TS16_ SHS18 _c chm	TS16_ SHS18 _d chm	TS16_ SHS18 _e chm	TS20_ SHS18 _a chm	TS20_ SHS18 _b chm	TS20_ SHS18 _c mgt	TS20_ SHS18 _d mgt	TS20_ SHS18 _e mgt	TS22_ SHS18 _a mgt
Weight % oxides																			
SiO_2	0.06	0.11	0.07	0.10	0.09	0.11	0.13	0.08	0.10	0.07	0.07	0.05	0.06	0.05	0.08	0.05	0.04	0.04	0.03
TiO_2	1.04	0.56	1.70	1.42	0.52	0.34	0.46	0.47	0.27	0.52	0.35	0.27	0.32	0.34	0.78	0.70	0.72	0.41	0.93
V_2O_3	0.18	0.40	0.34	0.36	0.26	0.30	0.26	0.30	0.14	0.18	0.18	0.17	0.15	0.17	0.19	0.11	0.15	0.16	0.18
Al_2O_3	7.11	12.09	15.51	15.61	12.66	15.95	15.16	15.64	18.43	9.79	20.99	17.48	17.34	9.87	10.69	4.46	5.34	0.72	1.44
Cr_2O_3	33.48	32.36	34.11	34.10	40.77	39.11	39.89	39.11	41.75	34.32	39.69	40.21	43.53	48.93	47.32	33.28	34.36	26.47	24.02
FeO	23.74	23.32	22.65	22.10	21.52	19.34	19.66	19.94	15.20	21.69	14.00	19.38	14.92	21.21	21.97	23.15	22.79	24.33	24.70
Fe_2O_3	30.87	27.24	20.24	20.20	17.06	16.54	16.21	16.58	12.68	28.56	12.33	14.59	12.54	12.62	12.07	33.99	31.92	44.49	46.24
MnO	0.52	0.28	0.34	0.37	0.66	0.52	0.70	0.68	0.17	0.55	0.12	0.25	0.16	0.53	0.90	1.20	1.14	1.06	0.38
MgO	3.25	3.92	5.52	5.65	5.32	7.32	7.03	6.90	11.06	5.04	12.31	7.98	11.29	5.65	5.33	3.08	3.43	1.98	2.19
CaO	0.00	0.00	0.02	0.01	0.01	0.01	0.00	0.00	0.01	0.00	0.01	0.01	0.01	0.01	0.01	0.00	0.00	0.01	0.01
NiO	0.12	0.21	0.13	0.12	0.06	0.05	0.05	0.05	0.19	0.15	0.22	0.08	0.18	0.05	0.03	0.12	0.15	0.09	0.17
ZnO	0.28	0.39	0.36	0.48	0.57	0.65	0.64	0.70	0.09	0.27	0.06	0.16	0.11	0.68	0.80	0.48	0.43	0.33	0.22
Total	100.65	100.89	100.97	100.51	99.49	100.23	100.21	100.47	100.09	101.15	100.34	100.63	100.61	100.10	100.17	100.62	100.47	100.10	100.53
Cr	0.81	0.77	0.84	0.84	1.03	0.95	0.98	0.96	1.00	0.81	0.93	0.97	1.04	1.26	1.23	0.80	0.83	0.61	0.55
Ti	0.02	0.01	0.04	0.03	0.01	0.01	0.01	0.01	0.01	0.01	0.01	0.01	0.01	0.01	0.02	0.02	0.02	0.01	0.02
V	0.00	0.01	0.01	0.01	0.01	0.01	0.01	0.01	0.00	0.00	0.00	0.00	0.00	0.00	0.00	0.00	0.00	0.00	0.00
Al	0.26	0.43	0.57	0.57	0.48	0.58	0.56	0.57	0.66	0.35	0.73	0.63	0.62	0.38	0.41	0.16	0.19	0.03	0.05
Fe^{3+}	0.90	0.77	0.54	0.55	0.47	0.45	0.44	0.45	0.34	0.82	0.32	0.39	0.33	0.34	0.32	1.01	0.94	1.34	1.37
Fe^{2+}	0.85	0.81	0.75	0.74	0.73	0.65	0.66	0.67	0.50	0.77	0.45	0.63	0.49	0.71	0.72	0.85	0.83	0.90	0.90
Mn	0.01	0.01	0.01	0.01	0.02	0.01	0.02	0.02	0.00	0.01	0.00	0.01	0.00	0.01	0.03	0.03	0.03	0.03	0.01
Mg	0.15	0.18	0.26	0.26	0.25	0.34	0.33	0.32	0.50	0.23	0.54	0.36	0.51	0.27	0.26	0.14	0.16	0.09	0.09
Ni	0.00	0.01	0.00	0.00	0.00	0.00	0.00	0.00	0.00	0.00	0.01	0.00	0.00	0.00	0.00	0.00	0.00	0.00	0.00
Zn	0.01	0.01	0.01	0.01	0.01	0.01	0.01	0.02	0.00	0.01	0.00	0.00	0.00	0.02	0.02	0.01	0.01	0.01	0.00
Mg#	0.15	0.18	0.25	0.26	0.26	0.34	0.33	0.32	0.50	0.23	0.55	0.37	0.51	0.28	0.27	0.14	0.16	0.09	0.09
Cr#	0.76	0.64	0.60	0.59	0.68	0.62	0.64	0.63	0.60	0.70	0.56	0.61	0.63	0.77	0.75	0.83	0.81	0.96	0.92
Fe^{3+}#	0.46	0.39	0.28	0.28	0.24	0.23	0.22	0.23	0.17	0.41	0.16	0.19	0.17	0.17	0.16	0.51	0.48	0.68	0.70
Al#	0.13	0.22	0.29	0.29	0.24	0.29	0.28	0.29	0.33	0.17	0.37	0.32	0.19	0.21	0.22	0.08	0.10	0.01	0.03
Ni ppm	919	1688	1049	916	465	423	417	425	1514	1204	1731	608	1430	358	252	967	1195	723	1350

Table 7.The EPMA data from the main body samples.

Body	MAIN	MAIN	MAIN	MAIN	MAIN	MAIN	MAIN	MAIN	MAIN	MAIN	MAIN	MAIN	MAIN	MAIN	MAIN	MAIN	MAIN	MAIN
Sample	TS22_SHS18_bmgt	TS22_SHS18_cmgt	TS22_SHS18_dmgt	TS24_SHS18_achm	TS24_SHS18_bchm	TS24_SHS18_cchm	TS24_SHS18_dchm	TS27_SHS18_achm	TS27_SHS18_bchm	TS27_SHS18_cchm	TS30_SHS18_achm	TS30_SHS18_bchm	TS30_SHS18_cchm	TS30_SHS18_dchm	TS33_SHS18_achm	TS33_SHS18_bchm	TS33_SHS18_cchm	TS33_SHS18_dchm
Weight % oxides																		
SiO_2	0.02	0.03	0.02	0.05	0.04	0.06	0.05	0.10	0.02	0.02	0.02	0.05	0.08	0.08	0.05	0.10	0.02	0.04
TiO_2	1.06	1.01	0.89	0.63	0.69	0.76	0.38	0.23	0.46	0.42	0.23	0.22	0.25	0.54	0.64	1.62	0.62	0.26
V_2O_3	0.19	0.19	0.17	0.12	0.11	0.10	0.08	0.19	0.14	0.14	0.10	0.11	0.10	0.09	0.10	0.16	0.15	0.11
Al_2O_3	2.63	2.38	1.30	11.05	11.37	11.73	11.53	13.93	14.14	14.78	12.88	13.94	12.85	14.03	13.71	17.48	16.82	15.81
Cr_2O_3	32.59	30.54	19.69	49.34	49.55	46.92	41.79	48.99	49.72	47.48	48.87	45.08	46.73	44.43	49.31	41.65	43.63	46.52
FeO	23.19	23.43	25.07	20.44	20.98	21.20	20.78	19.16	17.63	18.57	20.40	20.49	20.64	21.01	20.43	21.28	19.89	19.30
Fe_2O_3	36.40	38.56	50.27	9.98	9.79	11.98	18.38	8.30	8.55	9.84	9.49	12.24	11.89	11.99	7.82	9.76	10.09	9.59
MnO	0.46	0.42	0.24	0.42	0.36	0.39	0.54	0.29	0.21	0.31	0.24	0.31	0.34	0.35	0.26	0.37	0.33	0.35
MgO	3.12	2.93	1.95	6.64	6.55	6.13	5.73	8.17	9.52	8.77	7.00	6.67	6.59	6.45	7.68	7.53	7.84	8.26
CaO	0.00	0.01	0.00	0.01	0.00	0.00	0.01	0.00	0.00	0.01	0.00	0.01	0.00	0.01	0.00	0.00	0.01	0.00
NiO	0.17	0.18	0.27	0.01	0.02	0.00	0.02	0.05	0.13	0.10	0.02	0.02	0.04	0.02	0.12	0.05	0.04	0.08
ZnO	0.33	0.26	0.15	0.62	0.59	0.67	0.60	0.12	0.12	0.10	0.34	0.39	0.32	0.38	0.11	0.46	0.38	0.21
Total	100.17	99.94	100.03	99.30	100.05	99.94	99.89	99.53	100.64	100.54	99.58	99.53	99.82	99.38	100.22	100.48	99.83	100.52
Cr	0.78	0.73	0.44	1.28	1.28	1.21	1.04	1.25	1.24	1.18	1.25	1.14	1.19	1.13	1.26	1.05	1.09	1.16
Ti	0.02	0.02	0.02	0.02	0.02	0.02	0.01	0.01	0.01	0.01	0.01	0.01	0.01	0.01	0.02	0.04	0.01	0.01
V	0.00	0.00	0.00	0.00	0.00	0.00	0.00	0.00	0.00	0.00	0.00	0.00	0.00	0.00	0.00	0.00	0.00	0.00
Al	0.09	0.08	0.04	0.43	0.44	0.45	0.43	0.53	0.53	0.55	0.49	0.52	0.49	0.53	0.52	0.66	0.63	0.59
Fe^{3+}	1.09	1.15	1.49	0.26	0.25	0.32	0.51	0.21	0.22	0.25	0.25	0.33	0.32	0.32	0.20	0.24	0.26	0.24
Fe^{2+}	0.86	0.87	0.92	0.66	0.67	0.69	0.72	0.60	0.55	0.59	0.65	0.67	0.68	0.68	0.63	0.65	0.62	0.61
Mn	0.01	0.01	0.01	0.01	0.01	0.01	0.01	0.01	0.01	0.01	0.01	0.01	0.01	0.01	0.01	0.01	0.01	0.01
Mg	0.14	0.13	0.08	0.33	0.32	0.30	0.27	0.39	0.45	0.41	0.34	0.32	0.32	0.31	0.37	0.36	0.37	0.39
Ni	0.00	0.00	0.01	0.00	0.00	0.00	0.00	0.00	0.00	0.00	0.00	0.00	0.00	0.00	0.00	0.00	0.00	0.00
Zn	0.01	0.01	0.00	0.02	0.01	0.02	0.01	0.00	0.00	0.00	0.01	0.01	0.01	0.01	0.00	0.01	0.01	0.00
Mg#	0.14	0.13	0.08	0.33	0.32	0.30	0.27	0.39	0.45	0.41	0.34	0.32	0.32	0.31	0.37	0.36	0.37	0.39
Cr#	0.89	0.90	0.91	0.75	0.74	0.73	0.71	0.70	0.70	0.68	0.72	0.68	0.71	0.68	0.71	0.62	0.63	0.66
Fe^{3+}#	0.55	0.59	0.75	0.13	0.13	0.16	0.26	0.11	0.11	0.13	0.12	0.16	0.16	0.16	0.10	0.12	0.13	0.12
Al#	0.05	0.04	0.02	0.22	0.22	0.23	0.22	0.27	0.27	0.28	0.25	0.26	0.25	0.27	0.26	0.34	0.32	0.30
Ni ppm	1304	1422	2156	109	174	20	194	390	1033	759	167	185	333	172	959	424	350	654

Table 8. The EPMA data from the main body samples.

Body	MAIN	MAIN	MAIN	MAIN	MAIN	MAIN	MAIN	MAIN	MAIN	MAIN	MAIN	MAIN	MAIN	MAIN	MAIN	MAIN
Sample	140641_a chm	140641_b chm	140641_c chm	140641_d chm	140604_a chm	140604_b chm	140604_c chm	140604_d chm	TS53_SHS18_a chm	TS53_SHS18_b chm	TS53_SHS18_c chm	TS53_SHS18_d chm	TS56_SHS18_a chm	TS56_SHS18_b chm	TS56_SHS18_c chm	TS56_SHS18_d chm
Weight % oxides																
SiO_2	0.03	0.05	0.05	0.06	0.06	0.11	0.06	0.09	0.11	0.20	0.07	0.04	0.01	0.01	0.03	0.02
TiO_2	0.51	0.53	0.53	0.37	0.42	0.72	1.90	0.60	0.66	0.20	0.50	0.25	1.36	0.48	0.89	1.53
V_2O_3	0.13	0.13	0.13	0.14	0.15	0.14	0.38	0.33	0.10	0.10	0.04	0.08	0.14	0.09	0.13	0.15
Al_2O_3	10.67	10.45	10.43	9.95	11.34	13.31	15.87	10.79	13.86	11.52	11.75	12.71	11.79	11.24	11.82	12.37
Cr_2O_3	49.70	49.77	50.42	49.89	51.02	49.41	39.38	36.13	47.02	49.83	50.17	48.11	45.67	48.69	46.96	44.65
FeO	21.81	22.76	22.62	22.80	15.98	13.33	19.56	22.70	20.49	20.80	21.06	20.26	20.68	19.83	20.10	20.57
Fe_2O_3	10.86	10.82	9.86	11.49	11.01	10.72	15.28	24.84	9.70	9.31	8.48	9.92	11.61	10.48	11.22	11.79
MnO	0.46	0.46	0.48	0.46	0.15	0.13	0.13	0.25	0.24	0.31	0.31	0.30	0.44	0.39	0.44	0.40
MgO	5.91	5.16	5.17	4.78	10.08	12.26	8.38	4.38	7.11	6.35	6.53	6.78	6.49	6.70	6.71	6.66
CaO	0.00	0.00	0.00	0.00	0.01	0.01	0.00	0.00	0.01	0.01	0.00	0.00	0.00	0.00	0.01	0.00
NiO	0.12	0.11	0.16	0.05	0.13	0.19	0.18	0.15	0.02	0.01	0.01	0.01	0.02	0.03	0.04	0.05
ZnO	0.23	0.49	0.72	0.83	0.09	0.05	0.16	0.25	0.57	0.53	0.56	0.55	0.85	0.85	0.91	0.86
Total	100.41	100.72	100.58	100.83	100.42	100.39	101.27	100.50	99.89	99.18	99.47	99.02	99.06	98.79	99.26	99.03
Cr	1.28	1.29	1.31	1.29	1.27	1.21	0.97	0.88	1.20	1.30	1.31	1.24	1.19	1.27	1.22	1.16
Ti	0.01	0.01	0.01	0.01	0.01	0.02	0.04	0.01	0.02	0.01	0.01	0.01	0.03	0.01	0.02	0.04
V	0.00	0.00	0.00	0.00	0.00	0.00	0.01	0.01	0.00	0.00	0.00	0.00	0.00	0.00	0.00	0.00
Al	0.41	0.40	0.41	0.38	0.42	0.49	0.58	0.39	0.53	0.45	0.46	0.49	0.46	0.44	0.46	0.48
Fe^{3+}	0.29	0.28	0.26	0.30	0.29	0.28	0.40	0.70	0.25	0.24	0.22	0.26	0.31	0.28	0.30	0.31
Fe^{2+}	0.71	0.74	0.73	0.75	0.53	0.44	0.62	0.79	0.65	0.68	0.67	0.66	0.67	0.65	0.66	0.67
Mn	0.01	0.01	0.01	0.01	0.00	0.00	0.00	0.01	0.01	0.01	0.01	0.01	0.01	0.01	0.01	0.01
Mg	0.29	0.25	0.25	0.23	0.47	0.57	0.39	0.20	0.34	0.31	0.32	0.33	0.32	0.33	0.33	0.33
Ni	0.00	0.00	0.00	0.00	0.00	0.00	0.00	0.00	0.00	0.00	0.00	0.00	0.00	0.00	0.00	0.00
Zn	0.01	0.01	0.02	0.02	0.00	0.00	0.00	0.01	0.01	0.01	0.01	0.01	0.02	0.02	0.02	0.02
Mg#	0.29	0.25	0.26	0.24	0.47	0.56	0.38	0.20	0.35	0.32	0.32	0.33	0.32	0.33	0.33	0.33
Cr#	0.76	0.76	0.76	0.77	0.75	0.71	0.62	0.69	0.69	0.74	0.74	0.72	0.72	0.74	0.73	0.71
Fe^{3+}#	0.14	0.14	0.13	0.15	0.15	0.14	0.20	0.36	0.13	0.12	0.11	0.13	0.16	0.14	0.15	0.16
Al#	0.21	0.20	0.21	0.19	0.21	0.25	0.30	0.20	0.27	0.22	0.23	0.25	0.23	0.22	0.23	0.25
Ni ppm	915	892	1282	402	1018	1517	1407	1193	121	111	53	61	159	255	334	416

Table 9. The EPMA data from the upper body samples.

Body	UPPER	UPPER	UPPER	UPPER	UPPER	UPPER	UPPER	UPPER	UPPER	UPPER	UPPER	UPPER	UPPER	UPPER
Sample	140657_a mgt	140657_b mgt	140657_c_core chm	140657_c_rim1 mgt	140657_c_rim2 mgt	140657_d chm	140657_e_core chm	140657_e_rim1 chm	140657_e_rim2 mgt	TS16_MHP18_a mgt	TS16_MHP18_b chm	TS16_MHP18_c chm	TS16_MHP18_d chm	TS16_MHP18_e chm
Weight % oxides														
SiO_2	0.01	0.04	0.07	0.02	0.01	0.03	0.06	0.01	0.02	0.03	0.03	0.01	0.03	0.04
TiO_2	0.20	0.99	0.42	0.83	0.27	0.79	1.49	0.69	0.53	0.62	2.15	1.66	1.83	2.30
V_2O_3	0.09	0.08	0.20	0.10	0.09	0.10	0.22	0.09	0.11	0.24	0.24	0.21	0.16	0.29
Al_2O_3	0.02	0.83	14.47	1.08	0.15	1.33	12.95	1.77	0.25	0.68	11.13	11.98	14.11	10.33
Cr_2O_3	3.57	33.53	46.14	37.22	8.49	38.01	44.14	39.40	14.17	20.59	42.86	43.88	44.68	43.15
FeO	27.83	23.59	21.07	23.44	27.19	23.26	22.06	23.09	26.48	25.60	22.77	22.34	22.19	22.83
Fe_2O_3	67.45	36.52	8.63	32.75	62.86	32.23	10.90	30.12	56.99	50.42	12.80	12.56	8.47	14.42
MnO	0.22	0.51	0.32	0.42	0.03	0.55	0.52	0.50	0.18	0.19	0.40	0.37	0.27	0.37
MgO	0.35	2.28	6.25	2.30	0.59	2.59	5.64	2.59	0.85	1.36	5.02	5.48	6.35	5.10
CaO	0.00	0.01	0.01	0.01	0.01	0.01	0.00	0.00	0.01	0.00	0.00	0.00	0.00	0.01
NiO	0.42	0.30	0.04	0.22	0.56	0.21	0.04	0.21	0.48	0.36	0.07	0.04	0.05	0.05
ZnO	0.05	0.30	1.05	0.39	0.04	0.36	1.11	0.45	0.11	0.17	0.87	0.82	0.89	0.82
Total	100.20	98.97	98.66	98.78	100.29	99.47	99.15	98.93	100.19	100.26	98.33	99.36	99.03	99.70
Cr	0.07	0.82	1.20	0.93	0.18	0.95	1.16	0.99	0.31	0.46	1.15	1.15	1.18	1.14
Ti	0.00	0.02	0.01	0.02	0.01	0.02	0.04	0.02	0.01	0.01	0.05	0.04	0.05	0.06
V	0.00	0.00	0.00	0.00	0.00	0.00	0.00	0.00	0.00	0.00	0.01	0.00	0.00	0.01
Al	0.00	0.03	0.56	0.04	0.00	0.05	0.51	0.07	0.01	0.02	0.44	0.47	0.56	0.41
Fe^{3+}	1.92	1.11	0.22	1.00	1.81	0.98	0.28	0.91	1.67	1.49	0.34	0.33	0.21	0.38
Fe^{2+}	0.98	0.89	0.67	0.88	0.97	0.87	0.71	0.87	0.96	0.94	0.75	0.73	0.68	0.75
Mn	0.00	0.01	0.01	0.01	0.00	0.01	0.01	0.01	0.00	0.00	0.01	0.01	0.01	0.01
Mg	0.01	0.11	0.31	0.11	0.02	0.12	0.28	0.12	0.04	0.06	0.25	0.27	0.32	0.25
Ni	0.01	0.01	0.00	0.01	0.01	0.01	0.00	0.01	0.01	0.01	0.00	0.00	0.00	0.00
Zn	0.00	0.01	0.03	0.01	0.00	0.01	0.03	0.01	0.00	0.00	0.02	0.02	0.02	0.02
Mg#	0.01	0.11	0.31	0.11	0.02	0.12	0.28	0.12	0.04	0.06	0.25	0.27	0.32	0.25
Cr#	0.99	0.96	0.68	0.96	0.97	0.95	0.70	0.94	0.97	0.95	0.72	0.71	0.68	0.74
Fe^{3+}#	0.96	0.57	0.11	0.51	0.91	0.50	0.15	0.46	0.84	0.75	0.18	0.17	0.11	0.20
Al#	0.00	0.02	0.28	0.02	0.00	0.03	0.03	0.26	0.00	0.01	0.23	0.24	0.29	0.21
Ni ppm	3299	2346	277	1720	4387	1684	321	1657	3787	2836	532	345	360	395

Table 10. The EPMA data from the NE body samples.

Body	NE	NE	NE	NE	NE	NE	NE	NE	NE	NE	NE	NE	NE	NE
Sample	140778_a	140778_b	140778_c	140778_d	140778_e	140779_a	140779_b	140779_c	140779_d	140779_e	TS45_SH S18_a	TS45_SH S18_b	TS45_SH S18_c	TS45_SH S18_d
	chm	chm	chm	chm	chm	chm	chm	chm	chm	spinel	chm	chm	mgt	chm
Weight % oxides														
SiO_2	0.04	0.09	0.05	0.09	0.03	0.04	0.05	0.02	0.04	0.09	0.04	0.02	0.03	0.04
TiO_2	0.44	0.38	3.23	0.43	0.67	0.48	0.33	0.41	0.43	0.01	1.81	1.36	0.72	0.64
V_2O_3	0.17	0.13	0.43	0.25	0.21	0.24	0.16	0.18	0.15	0.05	0.15	0.14	0.11	0.13
Al_2O_3	11.48	11.43	14.21	14.03	13.08	17.22	14.82	10.02	8.63	27.30	10.45	10.79	1.64	2.33
Cr_2O_3	49.50	47.48	34.63	40.70	41.65	33.21	40.60	40.56	47.05	30.56	45.29	47.42	35.90	38.04
FeO	16.93	22.66	24.67	22.01	22.62	23.18	17.36	22.82	23.02	20.17	21.98	21.69	23.10	22.68
Fe_2O_3	11.32	11.04	16.83	15.71	15.33	20.09	17.33	20.35	14.99	12.34	12.16	10.48	33.99	31.20
MnO	0.14	0.41	0.53	0.27	0.50	0.42	0.14	0.61	0.53	0.43	0.53	0.55	0.63	0.63
MgO	9.22	5.08	4.62	5.36	5.01	4.71	8.91	4.02	4.21	8.04	5.50	5.76	2.80	3.08
CaO	0.00	0.00	0.00	0.01	0.00	0.01	0.01	0.00	0.00	0.00	0.01	0.01	0.00	0.01
NiO	0.10	0.05	0.08	0.11	0.05	0.20	0.16	0.14	0.06	0.04	0.01	0.02	0.09	0.08
ZnO	0.11	0.18	0.23	0.25	0.25	0.17	0.11	0.27	0.18	0.56	0.90	1.02	0.32	0.45
Total	99.45	98.92	99.49	99.24	99.40	99.96	99.97	99.40	99.28	99.58	98.83	99.26	99.32	99.30
Cr	1.25	1.24	0.91	1.03	1.06	0.81	0.98	1.02	1.23	0.72	1.21	1.25	0.88	0.94
Ti	0.01	0.01	0.08	0.01	0.02	0.01	0.01	0.01	0.01	0.00	0.05	0.03	0.02	0.02
V	0.00	0.00	0.01	0.01	0.00	0.00	0.00	0.00	0.00	0.00	0.00	0.00	0.00	0.00
Al	0.43	0.45	0.55	0.53	0.50	0.62	0.53	0.38	0.34	0.96	0.41	0.43	0.06	0.09
Fe^{3+}	0.30	0.29	0.44	0.43	0.42	0.55	0.48	0.58	0.42	0.31	0.32	0.27	1.03	0.94
Fe^{2+}	0.56	0.75	0.80	0.74	0.76	0.78	0.59	0.80	0.79	0.63	0.72	0.70	0.86	0.85
Mn	0.00	0.01	0.01	0.01	0.01	0.01	0.00	0.02	0.01	0.01	0.02	0.02	0.02	0.02
Mg	0.44	0.25	0.23	0.25	0.24	0.22	0.40	0.19	0.21	0.36	0.28	0.29	0.13	0.14
Ni	0.00	0.00	0.00	0.00	0.00	0.01	0.00	0.00	0.00	0.00	0.00	0.00	0.00	0.00
Zn	0.00	0.00	0.01	0.01	0.01	0.00	0.00	0.01	0.00	0.01	0.02	0.03	0.01	0.01
Mg#	0.44	0.25	0.22	0.26	0.24	0.22	0.41	0.19	0.21	0.36	0.28	0.29	0.13	0.15
Cr#	0.74	0.74	0.62	0.66	0.68	0.56	0.65	0.73	0.79	0.43	0.74	0.75	0.94	0.92
Fe^{3+}#	0.15	0.15	0.23	0.22	0.21	0.28	0.24	0.29	0.21	0.16	0.17	0.14	0.52	0.48
Al#	0.22	0.23	0.29	0.27	0.25	0.32	0.27	0.19	0.17	0.48	0.21	0.22	0.03	0.04
Ni ppm	755	363	621	889	377	1601	1255	1073	491	313	70	160	742	659

Table 11. The EPMA data from the SW body samples.

Body	SW	SW	SW	SW	SW	SW	SW	SW	SW	SW	SW	SW	SW	SW	SW
Sample	TS02_SHS18_a	TS02_SHS18_b	TS02_SHS18_c	TS02_SHS18_d	TS05_SHS18_a_core	TS05_SHS18_a_rim1	TS05_SHS18_a_rim2	TS05_SHS18_a_rim3	TS05_SHS18_b	TS05_SHS18_c	TS05_SHS18_d	TS01_MHP18_a	TS01_MHP18_b	TS01_MHP18_c	TS01_MHP18_d
	mgt	chm	chm	mgt	chm	chm	mgt	mgt	chm	chm	chm	chm	chm	chm	chm
Weight % oxides															
SiO_2	0.01	0.15	0.02	0.03	0.06	0.06	0.04	0.94	0.04	0.09	0.03	0.02	0.04	0.02	0.01
TiO_2	0.72	0.55	0.58	0.70	0.40	0.64	0.86	0.01	0.73	0.60	0.78	0.45	0.41	1.83	0.37
V_2O_3	0.12	0.14	0.12	0.13	0.18	0.13	0.18	0.01	0.15	0.14	0.14	0.18	0.14	0.24	0.13
Al_2O_3	2.87	2.89	2.85	2.80	11.11	3.48	1.12	0.01	3.06	3.95	3.18	12.48	12.26	10.30	10.95
Cr_2O_3	36.36	39.27	39.31	35.97	46.78	40.28	18.16	0.42	39.88	40.94	38.53	48.67	50.37	46.54	48.28
FeO	22.72	22.77	23.11	22.80	21.11	22.39	25.12	28.71	22.70	22.94	23.18	21.43	17.03	22.73	21.29
Fe_2O_3	33.26	30.56	30.40	33.86	13.92	28.97	52.70	71.39	29.63	27.26	30.74	8.58	9.17	11.41	11.34
MnO	0.44	0.47	0.47	0.41	0.25	0.34	0.17	0.00	0.36	0.35	0.40	0.29	0.23	0.30	0.38
MgO	3.58	3.44	3.20	3.50	6.06	3.82	2.27	0.28	3.57	3.37	3.26	6.36	9.35	5.55	5.95
CaO	0.01	0.02	0.01	0.00	0.00	0.00	0.01	0.03	0.00	0.00	0.00	0.00	0.01	0.00	0.01
NiO	0.09	0.08	0.05	0.08	0.04	0.12	0.28	0.02	0.12	0.11	0.14	0.04	0.14	0.05	0.03
ZnO	0.15	0.25	0.17	0.25	0.33	0.25	0.07	0.02	0.26	0.19	0.17	0.21	0.09	0.34	0.21
Total	100.33	100.59	100.29	100.54	100.24	100.49	100.96	101.85	100.50	99.93	100.57	98.71	99.25	99.31	98.95
Cr	0.88	0.96	0.97	0.87	1.19	0.99	0.40	0.01	0.98	1.02	0.95	1.27	1.28	1.24	1.25
Ti	0.02	0.01	0.01	0.02	0.01	0.02	0.02	0.00	0.02	0.01	0.02	0.01	0.01	0.05	0.01
V	0.00	0.00	0.00	0.00	0.00	0.00	0.00	0.00	0.00	0.00	0.00	0.00	0.00	0.01	0.00
Al	0.10	0.11	0.10	0.10	0.42	0.13	0.04	0.00	0.11	0.15	0.12	0.49	0.46	0.41	0.42
Fe^{3+}	0.99	0.91	0.90	1.01	0.38	0.86	1.54	1.99	0.88	0.81	0.91	0.22	0.24	0.30	0.30
Fe^{2+}	0.84	0.84	0.85	0.84	0.70	0.82	0.91	0.99	0.83	0.84	0.85	0.68	0.55	0.73	0.70
Mn	0.01	0.01	0.01	0.01	0.01	0.01	0.00	0.00	0.01	0.01	0.01	0.01	0.01	0.01	0.01
Mg	0.16	0.16	0.15	0.16	0.29	0.18	0.09	0.01	0.17	0.16	0.15	0.31	0.45	0.28	0.29
Ni	0.00	0.00	0.00	0.00	0.00	0.00	0.01	0.00	0.00	0.00	0.00	0.00	0.00	0.00	0.00
Zn	0.00	0.01	0.00	0.01	0.01	0.01	0.00	0.00	0.01	0.00	0.00	0.01	0.00	0.01	0.00
Mg#	0.16	0.16	0.15	0.16	0.29	0.18	0.09	0.01	0.17	0.16	0.15	0.31	0.45	0.28	0.29
Cr#	0.89	0.90	0.90	0.90	0.74	0.89	0.92	0.97	0.90	0.87	0.89	0.72	0.73	0.75	0.75
Fe^{3+}#	0.50	0.46	0.46	0.51	0.19	0.43	0.78	1.00	0.44	0.41	0.46	0.11	0.12	0.15	0.15
Al#	0.05	0.05	0.05	0.05	0.21	0.06	0.02	0.00	0.06	0.07	0.06	0.25	0.23	0.21	0.21
Ni ppm	685	595	396	629	282	934	2164	118	941	875	1077	295	1087	377	225

APPENDIX 2.

Table 12. Ru content from LA-ICP-MS data in analysed chromite grains. See how the data was reprocessed from the chapter 4.2.3. Abbrevation, NaN = not analysed.

Thick section	Ru99 µg/g	Ru101 µg/g
TS05_SHS18_1	NaN	0.05
TS05_SHS18_2	NaN	0.14
TS05_SHS18_3	NaN	0.09
TS05_SHS18_6	0.10	0.06
TS05_SHS18_7	0.14	0.06
TS16_SHS18_8	0.15	0.14
TS16_SHS18_9	0.58	0.62
TS16_SHS18_10	0.11	0.09
TS16_SHS18_11	0.16	0.12
TS16_SHS18_12	0.17	0.17
TS16_SHS18_13	0.19	0.16
TS16_SHS18_14	0.30	0.36
TS27_SHS18b_16	0.33	0.29
TS27_SHS18b_17	0.60	0.52
TS27_SHS18b_18	0.31	0.27
TS39_SHS18b_22	0.38	0.39
TS39_SHS18b_23	0.27	0.25
TS39_SHS18b_24	0.17	0.10
TS39_SHS18b_25	0.19	0.13
TS39_SHS18b_26	0.18	0.18
TS39_SHS18b_27	0.26	0.18
TS39_SHS18b_28	0.16	0.09
TS39_SHS18b_29	0.25	0.28
TS46_SHS18b_30	1.52	1.23
TS46_SHS18b_31	0.23	0.26
TS46_SHS18b_32	0.68	0.60
TS46_SHS18b_33	0.28	0.34
TS46_SHS18b_35	0.36	0.50
TS46_SHS18b_37	0.23	0.32
TS46_SHS18b_38	0.66	0.77
TS46_SHS18b_39	0.49	0.54
TS46_SHS18b_40	0.14	0.15

APPENDIX 3.

Table 13. Sample list.

Sample ID	Drillhole	Start depth (m)	End depth (m)	Lithology	Body	Thin section	EPMA analysis	Grains	20 nA	40 nA	Thick sections
TS01_SHS18	13MOS8137	63.33	63.38	1B	SW	x					
TS02_SHS18	13MOS8137	89.55	89.6	1B	SW	x	x	4	x		
TS03_SHS18	13MOS8137	114.85	114.9	1B	SW	x					
TS05_SHS18	13MOS8137	209.48	209.53	1B	SW	x	x	7	x		x
TS01_MHP18	13MOS8137	182.34	182.39	1B	SW	x	x	4		x	
TS06_SHS18	17MOS8168	488.2	488.25	1B	MAIN	x					
TS07_SHS18	17MOS8168	505.23	505.27	1B	MAIN	x	x	4	x		
TS07_SHS18b	17MOS8168	505.27	505.33	1B	MAIN						
TS08_SHS18	17MOS8168	522.19	522.24	1B	MAIN	x					
TS08_SHS18b	17MOS8168	522.24	522.29	1B	MAIN						
TS09_SHS18	17MOS8168	541.22	541.27	1B	MAIN	x					
TS09_SHS18b	17MOS8168	541.27	541.32	1B	MAIN						
TS10_SHS18	17MOS8168	557.41	557.46	1B	MAIN	x	x	4	x		
TS10_SHS18b	17MOS8168	557.36	557.41	1B	MAIN						
TS11_SHS18	17MOS8168	572.63	572.68	1B	MAIN	x					
TS11_SHS18b	17MOS8168	572.68	572.73	1B	MAIN						
TS12_SHS18	17MOS8168	594	594.05	1B	MAIN	x					
TS12_SHS18b	17MOS8168	594.05	594.1	1B	MAIN						
TS13_SHS18	17MOS8168	607.65	607.7	1B	MAIN	x					
TS13_SHS18b	17MOS8168	607.6	607.65	1B	MAIN						
TS14_SHS18	17MOS8168	623.24	623.29	1B	MAIN	x					
TS14_SHS18b	17MOS8168	623.29	623.34	1B	MAIN						
TS15_SHS18	17MOS8168	640.96	641.01	1B	MAIN	x					
TS15_SHS18b	17MOS8168	641.01	641.06	1B	MAIN						
TS16_SHS18	17MOS8168	656.95	657	1B	MAIN	x	x	5	x		x

Sample ID	Drillhole	Start depth (m)	End depth (m)	Lithology	Body	Thin section	EPMA analysis	Grains	20 nA	40 nA	Thick sections
TS17_SHS18	17MOS8168	673.18	673.23	1B	MAIN	x					
TS17_SHS18b	17MOS8168	673.13	673.18	1B	MAIN						
TS18_SHS18	17MOS8168	693.29	693.34	1B	MAIN	x					
TS18_SHS18b	17MOS8168	693.34	693.39	1B	MAIN						
TS19_SHS18	17MOS8168	697.94	697.99	1B	MAIN	x					
TS19_SHS18b	17MOS8168	697.89	697.94	1B	MAIN						
TS20_SHS18	17MOS8168	719.72	719.77	1B	MAIN	x	x	5	x		
TS21_SHS18	17MOS8168	732.22	732.27	1B	MAIN	x					
TS21_SHS18b	17MOS8168	732.17	732.22	1B	MAIN						
TS22_SHS18	17MOS8168	746.35	746.4	1B	MAIN	x	x	4	x		
TS22_SHS18b	17MOS8168	746.3	746.35	1B	MAIN						
TS23_SHS18	17MOS8168	760.1	760.15	1B	MAIN	x					
TS23_SHS18b	17MOS8168	760.05	760.1	1B	MAIN						
TS24_SHS18	17MOS8168	773.32	773.37	1B	MAIN	x	x	4	x		
TS24_SHS18b	17MOS8168	773.37	773.42	1B	MAIN						
TS25_SHS18	17MOS8168	781.1	781.15	1B	MAIN	x					
TS25_SHS18b	17MOS8168	781.05	781.1	1B	MAIN						
TS26_SHS18	17MOS8168	793.53	793.53	1B	MAIN	x					
TS26_SHS18b	17MOS8168	793.48	793.53	1B	MAIN						
TS27_SHS18	17MOS8168	808.08	808.13	1B	MAIN	x	x	3	x		
TS27_SHS18b	17MOS8168	808.13	808.18	1B	MAIN						x
TS28_SHS18	17MOS8168	819.21	819.26	1B	MAIN	x					
TS28_SHS18b	17MOS8168	819.26	819.31	1B	MAIN						
TS29_SHS18	17MOS8168	835	835.05	1B	MAIN	x					
TS29_SHS18b	17MOS8168	835.05	835.1	1B	MAIN						
TS30_SHS18	17MOS8168	849.17	849.22	1B	MAIN	x	x	4	x		
TS30_SHS18b	17MOS8168	849.22	849.27	1B	MAIN						
TS31_SHS18	17MOS8168	868.9	868.95	1A	MAIN	x					

Table 12. Continued.

Sample ID	Drillhole	Start depth (m)	End depth (m)	Lithology	Body	Thin section	EPMA analysis	Grains	20 nA	40 nA	Thick sections
TS31_SHS18b	17MOS8168	868.95	869	1A	MAIN						
TS32_SHS18	17MOS8168	883	883.05	1A	MAIN	x					
TS32_SHS18b	17MOS8168	883.05	883.1	1A	MAIN						
TS33_SHS18	17MOS8168	894.05	894.1	1A	MAIN	x	x	4	x		
TS33_SHS18b	17MOS8168	894	894.05	1A	MAIN						
140656	13MOS8123	18	18.05	1B	UPPER	x					
TS34_SHS18b	13MOS8123	18.05	18.1	1B	UPPER						
140657	13MOS8123	37.6	37.65	1B	UPPER	x	x	9		x	
TS35_SHS18b	13MOS8123	37.55	37.6	1B	UPPER						
140658	13MOS8123	75.4	75.45	1B	UPPER	x					
TS36_SHS18b	13MOS8123	75.45	75.5	1B	UPPER						
140659	13MOS8123	100.35	100.4	1B	UPPER	x					
TS37_SHS18b	13MOS8123	100.4	100.45	1B	UPPER						
140660	13MOS8123	122.5	122.55	1B	UPPER	x					
TS38_SHS18b	13MOS8123	122.55	122.6	1B	UPPER						
TS16_MHP18	13MOS8123	90.13	90.18	1B	UPPER	x	x	5		x	
140604	13MOS8123	718.8	718.85	1B	MAIN	x	x	4	x		
TS39_SHS18b	13MOS8123	718.85	718.9	1B	MAIN						x
140610	13MOS8123	872.4	872.45	1A	MAIN	x					
TS40_SHS18b	13MOS8123	874.45	874.5	1A	MAIN						
140641	11MOS8060	881.4	881.45	1B	MAIN	x	x	4	x		
TS41_SHS18b	11MOS8060	881.45	881.5	1B	MAIN						
140652	11MOS8060	1043.65	1043.7	1B	MAIN	x					
TS42_SHS18b	11MOS8060	1043.7	1043.75	1B	MAIN						
140654	11MOS8060	1089.2	1089.25	1B	MAIN	x					
TS43_SHS18b	11MOS8060	1089.15	1089.2	1B	MAIN						
140777	12MOS8076	39.05	39.1	1B	NE	x					
TS44_SHS18b	12MOS8076	39.1	39.15	1B	NE						
TS45_SHS18	12MOS8076	59.45	59.5	1B	NE	x	x	4		x	
140778	12MOS8076	81.85	81.9	1B	NE	x	x	5		x	
TS46_SHS18b	12MOS8076	81.9	81.95	1B	NE						x
140779	12MOS8076	102.65	102.7	1B	NE	x	x	5		x	

Table 12. Continued.

Sample ID	Drillhole	Start depth (m)	End depth (m)	Lithology	Body	Thin section	EPMA analysis	Grains	20 nA	40 nA	Thick sections	
TS47_SHS18b	12MOS8076	102.6	102.65	1B	NE							
TS48_SHS18	12MOS8076	122.97	123.02	1B	NE	x						
TS49_SHS18	18MOS8209B	694.05	694.1	1B	MAIN	x						
TS49_SHS18b	18MOS8209B	694	694.05	1B	MAIN							
TS52_SHS18	17MOS8169B	677.55	677.6	1B	MAIN	x						
TS52_SHS18b	17MOS8169B	677.6	677.65	1B	MAIN							
TS53_SHS18	17MOS8169B	742.51	742.56	1B	MAIN	x	x	4	x			
TS53_SHS18b	17MOS8169B	742.56	742.61	1B	MAIN							
TS54_SHS18	17MOS8169B	833	833.05	1A	MAIN	x						
TS54_SHS18b	17MOS8169B	833.05	833.1	1A	MAIN							
TS55_SHS18	12MOS8102	724.2	724.25	1B	MAIN	x						
TS56_SHS18	12MOS8102	837.83	837.88	1B	MAIN	x	x	4		x		
TS57_SHS18	11MOS8043	573.47	573.52	1B	MAIN	x						
TS58_SHS18	11MOS8043	704.16	704.21	1B	MAIN	x						
TS59_SHS18	12MOS8078	318.82	318.87	1B	MAIN	x						
TS60_SHS18	12MOS8078	504.84	504.89	1B	MAIN	x						
102	10			2	4	59	21	96	14	7	5	Total